RICE UNIVERSITY

A Demonstration and Evaluation of Trajectory Mapping

by

Gary Allen Morris

A THESIS SUBMITTED
IN PARTIAL FULFILLMENT OF THE
REQUIREMENTS FOR THE DEGREE

Doctor of Philosophy

APPROVED, THESIS COMMITTEE:

Arthur A. Few, Chairman
Professor of Space Physics & Astronomy

Mark R. Schoeberl
Branch Head
Atmospheric Chemistry and
Dynamics Branch
NASA/Goddard Space Flight Center

Tamara A. S. Ledley
Senior Faculty Fellow
Dept. of Space Physics & Astronomy

Ronald L. Sass
Professor of Ecology &
Evolutionary Biology

Houston, Texas
September, 1994

DISCLAIMER

Abstract

A Demonstration and Evaluation of Trajectory Mapping

by

Gary Allen Morris

The problem of creating synoptic maps from asynoptically gathered data has prompted the development of a number of schemes. Most notable among these schemes are the Kalman filter, the Salby-Fourier technique, and constituent reconstruction. This thesis presents a new technique, called trajectory mapping. Trajectory mapping employs a simple model of air parcel motion to create synoptic maps from asynoptically gathered data.

To assess the applicability of the technique, four sources of trajectory mapping errors were analyzed. The analysis revealed that 1) the computational error is negligible; 2) measurement uncertainties can result in errors which grow with time scales on the order of a week; 3) isentropic approximations lead to errors characterized by time scales of a week; and 4) wind field inaccuracies can cause significant errors in individual parcel trajectories in a matter of hours. All the studies, however, indicated that while individual trajectory errors can grow rapidly, constituent distributions, such as those depicted in trajectory maps, are much more robust, maintaining a high level of accuracy for periods on the order of several weeks.

The trajectory mapping technique has been successfully applied to a variety of problems. First, trajectory mapping was employed in the study of dynamical wave-breaking events. Second, trajectory mapping was applied in satellite data validation studies, both for the determination of instrument accuracy and precision. Third, trajectory mapping was used to assess the accuracy of the meteorological wind fields. Such demonstrations imply that trajectory mapping will become an important tool in answering questions of global change, particularly the issue of ozone depletion.

Acknowledgments

First, this research was performed under appointment to the U.S. Department of Energy, Graduate Fellowships for Global Change Program, administered by Oak Ridge Institute for Science and Education (grant number DE–AC05–760R00033). Thanks to Mary Kinney, Milton Constantin, and all the people at Oak Ridge and the Department of Energy for accommodating my often peculiar requests and providing the monetary support for my research over the last two years.

Thanks to all the people involved in the creation, processing, and reduction of the data sets used in the studies presented in this thesis. In particular, thanks to Joe Waters (MLS), Aiden Roche (CLAES), Jim Russell (HALOE), Richard Swinbank (UKMO), Paul Newman and Leslie Lait (NMC), Ricky Rood (GSFC), Jim Gleason (SBUV2), and Mike Proffitt (ER-2 Ozone) not only for their data but also for helpful comments and suggestions along the way.

Thanks to Lee Elson for creating and allowing my use of Figure 2.4, to Leslie Lait for creating and allowing my use of Figure 2.5, and to Lynn Sparling and Mark Schoeberl for allowing my use of Figure 3.2.

Thanks to Mark Schoeberl, my advisor at NASA/Goddard for allowing me to conduct my dissertation research at Goddard and under him. His enthusiasm, knowledge, and encouragement were invaluable. Also, thanks to all the people at NASA/Goddard in Code 916 without who's assistance my journey to completing this thesis would have been much more arduous.

Thanks also to Arthur Few and Rice University for allowing me to pursue my research at an institution not only outside of the University, but even outside the city of Houston. Dr. Few's patience and efforts to stay familiar with my research despite the great distance were appreciated.

Finally, thanks to my family and friends, who have endured, entertained, and encouraged me throughout my graduate career. In particular, I owe my sanity (or what's left of it) to those individuals who have interrupted my work via e-mail and telephone calls with a joke, philosophical discussion, sports debate, or any other matter that had NOTHING TO DO WITH MY RESEARCH!

Contents

Illustrations

Tables

Chapter 1

Introduction

Theories and observational evidence of global warming and ozone depletion have captured the interests of scientists, politicians, and the general public. Reports last year of new record low ozone values over Antarctica [14] and at northern mid-latitudes [10] further amplify our need to understand Earth system behavior. Our current understanding is based upon the existing suite of atmospheric chemical and dynamical models. Such models, however, can only be as good as the data sets used in their creation.

Until recently, collecting data on the Earth's atmospheric system has been primarily dependent upon a network of radiosonde stations. These stations, scattered across the planet but mostly concentrated on the inhabited continents, synchronously release weather balloons. The combined data sets from the various stations yield the synoptic maps of the thermodynamical and dynamical structure of the Earth's atmosphere. These synoptic maps are required to initialize and test the predictive models.

In the last 30 years, the advent of orbiting satellites has opened a new era of collecting Earth system data. Satellite instruments can make measurements in remote locations where no radiosondes exist. Satellite data, however, present an immediate problem to the forecasters and modelers who wish to use it. The nature of satellite data collection is very different from the synchronous radiosonde observations, which provide information from widely different regions of the globe at the same time. Satellites can only provide data from one location at one instant in time (except geosynchronous satellites, which provide data continuously for fixed locations within their field of view). The central problem with using satellite data sets, therefore, is the creation of the type of useful, synoptic maps which the radiosonde data provide.

Several methods have been developed over the course of the last decade to produce synoptic maps from asynoptically gathered data: Kalman filtering, Salby's Fourier technique, constituent reconstruction, and trajectory mapping. The last and most recent addition to this list will be the main subject of the present work.

In order to build motivation for the development of this new technique, a brief review of the previously developed techniques, including their strengths and weaknesses, is provided. The trajectory mapping technique is then outlined and assessed. As part of the assessment, potential errors associated with the trajectory mapping technique are examined and estimated. Next, applications of the technique to problems of dynamical analysis and data validation are provided. These applications demonstrate the success, accuracy, and utility of the trajectory mapping technique. Finally, the Appendices provide information on the satellite, aircraft, and meteorological data sets required to produce the maps and figures in this thesis.

Chapter 2

Previous Mapping Techniques

Various techniques have been developed over the last decade to accommodate the creation of global constituent maps from asynoptically gathered data (usually satellite data). Strengths and weaknesses of four of these techniques (daily asynoptic mapping [13], Kalman filtering [12, 36], Salby's Fourier technique [41, 42, 20], and constituent reconstruction [46]) are presented and discussed in this Chapter.

2.1 Daily Asynoptic Maps

Daily global maps can be produced directly from raw data sets which contain a sufficiently large number of measurements and wide geographic scope. Clearly, a major advantage of this technique lies in its simplicity: just map the data points where they are measured. Figure 2.1 depicts a map created from one day of N_2O measurements made by the Cryogenic Limb Array Etalon Spectrometer (CLAES, see Appendix A.2), an instrument on the Upper Atmosphere Research Satellite (UARS). Such a map provides fairly uniform coverage of the region over which the satellite makes measurements. Regions of data drop-out, however, can leave large sections of the globe unsampled. In addition, the regions observed at any given time are limited by the satellite orbit. For example, observations made by UARS are, due to the satellite's orbital geometry, restricted primarily to one hemisphere at a time (see Appendix A).

Another potential problem with asynoptic maps is their tendency to alias atmospheric features, particularly those with time scales on the order of a day or less. To properly capture the dynamics, more sophisticated techniques are required. *Hartmann* [13] employed one such technique in his study of Nimbus–5 satellite data. First, he constructed time series of asynoptically gathered satellite data on latitude circles. An atmospheric wave with wavenumber m and phase speed c should produce a longitudinal constituent distribution given by

$$\rho = \rho_0 e^{im(\lambda - ct)} \tag{2.1}$$

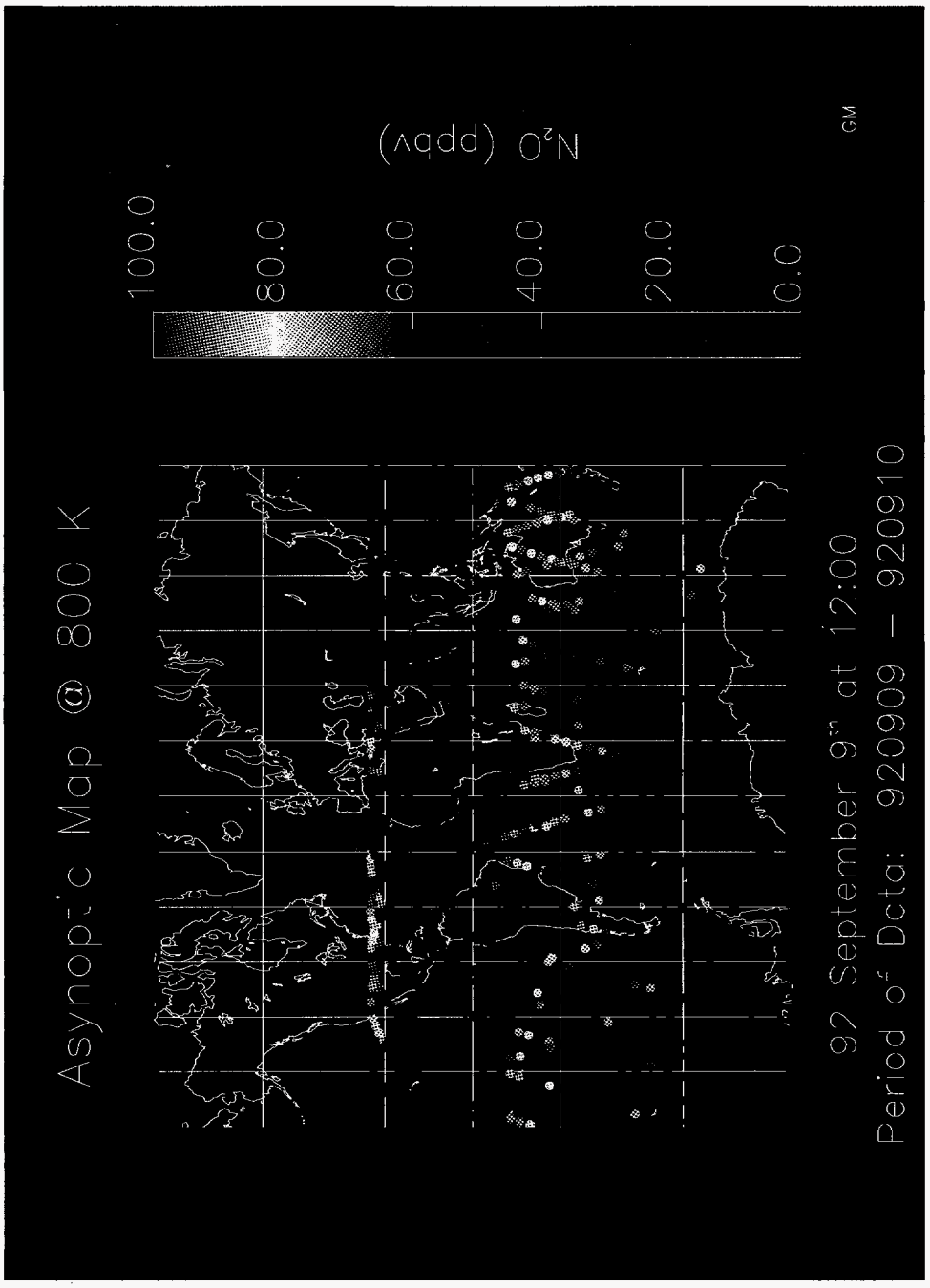

Figure 2.1 Asynoptic Map of CLAES N_2O Data

on a given pressure surface, where λ is the longitudinal position. Given the nature of satellite data retrieval, t and λ are not independent variables. In fact, they are related by

$$\lambda = \lambda_0 + (t - t_0)V_s \tag{2.2}$$

where V_s is the angular velocity of the satellite. As a result, the constituent distribution the satellite observes is given by

$$\rho = \rho_0 e^{im[\lambda_0 - V_s t_0 + (V_s - c)t]} \tag{2.3}$$

Furthermore, the satellite retrieval pattern results in a phase discontinuity at the longitude λ_0 where the measurements for a given day begin and end. While this inaccuracy is a less serious problem in the stratosphere than in the troposphere, it can still confuse the dynamical picture. For examining low zonal wavenumber phenomena ($m = 1$ or 2), corrections based upon the information contained in Equation 2.3 may be adequate. For higher frequency phenomena, however, a more sophisticated approach should be employed.

2.2 Kalman Filtering

The Kalman Filtering technique for mapping satellite data of any type (including meteorological variables and chemical constituents) has been derived from a technique (originally proposed by *Kalman* [15] and expanded upon by *Kalman and Bucy* [16]) to optimally estimate the true state of a system given a set of noisy measurements and their corresponding error estimates. The technique has been adapted to satellite retrieval work by a number of authors. Here, the description developed by *Haggard et al.* [12] for use with data from the Nimbus 7 satellite is presented.

The basic Kalman filter, as applied to map satellite data, proceeds as follows: optimally fit a spatially defined Fourier series on each latitude circle to the satellite retrieved data at a given altitude. Assimilate new measurements into the model with a statistical weight inversely proportional to the magnitude of the associated error estimates. In this way, measurements with small associated errors will contribute the most to the filter's estimate of the constituent field. When the model has been run to the desired output time, the field can be reconstructed along each latitude circle from the Fourier coefficients.

To gain an understanding of the basic principles behind the Kalman filter, examine the simple case of data gathered synoptically on a single latitude circle at a single

altitude. In this case, an estimate for the field can be determined by solving the system of linear equations for the Fourier series representations of each measurement (T_m):

$$T_m(t_n, \lambda_n) = \vec{\mathrm{K}}^T(\lambda_n) \cdot \vec{\mathrm{X}}(t_n, \lambda_n) \tag{2.4}$$

where $T_m(t_n, \lambda_n)$ is the scalar quantity measured at time t_n and longitude λ_n, $\vec{\mathrm{X}}(t_n, \lambda_n)$ represents the Fourier coefficients, and $\vec{\mathrm{K}}^T$ represents the terms of the Fourier series given by

$$\vec{\mathrm{K}}^T(\lambda_n) = [1, \cos(\lambda_n), \sin(\lambda_n), \cos(2\lambda_n), \sin(2\lambda_n), \ldots \sin(M\lambda_n)] \tag{2.5}$$

with M being the order of the Fourier series. (Note: $\vec{\mathrm{A}}$ denotes a column vector, $\vec{\mathrm{A}}^T$ denotes a row vector, and $\mathbf{A}$ denotes a matrix.) In this case, a solution to the problem can be found by simply solving Equation 2.4 for the unique set of Fourier coefficients $\vec{\mathrm{X}}$ which yields the minimum least squares fit T to the data T_m. The problem can be solved as long as the number of terms in the Fourier series of Equation 2.5 is no greater than the number of measurements. In other words,

$$M \leq (\#\quad \text{of} \quad \text{measurements} - 1)/2 \tag{2.6}$$

Using this procedure, a constituent value ($T(t, \lambda)$) can be estimated at all longitudes at a specified time, altitude, and latitude.

The satellite data retrieval problem, however, is somewhat more complicated. The data on a given latitude circle are not all taken at the same time. Therefore, the Kalman filter is employed in an attempt to optimally construct the Fourier series estimates of the data field. Beginning from an estimate of the initial field and an estimate of its associated error, a model projects future distributions. When new measurements become available, they influence the model so as to bring the model output closer to the measurements. The amount of influence each measurement has is related to its associated error estimate. Essential to the technique, therefore, is an estimate of the measurement errors. Data sets from the instruments aboard the Upper Atmosphere Research Satellite (UARS) provide such error estimates.

As with the measurements, a Fourier series can be fit to the error estimates:

$$\sigma(t_n, \lambda_n) = \vec{\mathrm{K}}^T(\lambda_n) \cdot \vec{\mathrm{Y}}(t_n, \lambda_n) \tag{2.7}$$

where $\vec{\mathrm{Y}}(t_n, \lambda_n)$ represents the Fourier coefficients for the errors. To provide correct weighting between new measurements and model estimates, the variance, rather than

the error, is the relevant quantity to examine. The variance is given simply by

$$\sigma^2(t_n,\lambda_n) = (\vec{\mathrm{K}}^T(\lambda_n)\cdot\vec{\mathrm{Y}}(t_n,\lambda_n)(\vec{\mathrm{K}}^T(t_n,\lambda_n)\cdot\vec{\mathrm{Y}}(t_n,\lambda_n) \quad (2.8)$$

$$= \vec{\mathrm{K}}^T(\lambda_n)\mathbf{S}\vec{\mathrm{K}}(\lambda_n) \quad (2.9)$$

where $\mathbf{S}$ is the covariance matrix with elements

$$\mathbf{S}_{ij} = \vec{\mathrm{Y}}_i\vec{\mathrm{Y}}_j \quad (2.10)$$

Two further quantities are required by the Kalman filter: $d\vec{\mathrm{X}}/dt$ and $d\mathbf{S}/dt$. Knowing the rate of change of the Fourier coefficients associated with the measurements and the variances allows predictions to be made at future times. These future estimates are given by

$$\vec{\mathrm{X}}(t_{n+1},\lambda) = \vec{\mathrm{X}}(t_n,\lambda) + (t_{n+1}-t_n)d\vec{\mathrm{X}}/dt \quad (2.11)$$

$$\mathbf{S}(t_{n+1},\lambda) = \mathbf{S}(t_n,\lambda) + |t_{n+1}-t_n|d\mathbf{S}/dt \quad (2.12)$$

Substituting these equations into Equations 2.4 and 2.9 respectively yields the model estimates of the constituent value ($T_e(t_{n+1},\lambda)$) and its error ($\sigma_e^2(t_{n+1},\lambda)$) at time t_{n+1}.

The model estimate is improved through the assimilation of new measurements in the following manner:

$$\vec{\mathrm{X}}^*{}_n = \vec{\mathrm{X}}(t_n,\lambda) + \frac{\mathbf{S}(t_n,\lambda)\vec{\mathrm{K}}(\lambda_n)(T_m(t_n,\lambda_n)-T_e(t_n,\lambda_n))}{\sigma_e^2(t_n,\lambda_n)+\sigma_m^2(t_n,\lambda_n)} \quad (2.13)$$

$$\mathbf{S}^*{}_n = \mathbf{S}(t_n,\lambda) - \frac{\mathbf{S}(t_n,\lambda)\vec{\mathrm{K}}(\lambda_n)\vec{\mathrm{K}}^T(\lambda_n)\mathbf{S}(t_n,\lambda)}{\sigma_e^2(t_n,\lambda_n)+\sigma_m^2(t_n,\lambda_n)} \quad (2.14)$$

In the first case, premultiplying by $\vec{\mathrm{K}}^T(\lambda_n)$ gives a new model estimate for the constituent value of

$$T(t_n,\lambda_n) = T_e(t_n,\lambda_n) + \frac{T_m(t_n,\lambda_n)-T_e(t_n,\lambda_n)\sigma_e^2(t_n,\lambda_n)}{\sigma_e^2(t_n,\lambda_n)+\sigma_m^2(t_n,\lambda_n)} \quad (2.15)$$

In the second case, premultiplying by $\vec{\mathrm{K}}^T(\lambda_n)$ and postmultiplying by $\vec{\mathrm{K}}(\lambda_n)$ yields the new model variance given by

$$(\sigma^2(t_n,\lambda_n))^{-1} = (\sigma_e^2(t_n,\lambda_n))^{-1} + (\sigma_m^2(t_n,\lambda_n))^{-1} \quad (2.16)$$

As can be seen, the new measurements are incorporated in proportion to the relative weight merited by their associated variances.

All of the above equations are invariant under time reversal. Data, therefore, can be assimilated both forward and backward in time. By using forward and backward calculations in combination, twice the number of measurements can be included in the field estimates. The Fourier coefficients for the combined forward and backward technique can be determined through a weighted combination of the coefficients from the separate forward and backward calculations. The combined coefficients are given by

$$\vec{\mathrm{X}} = \mathbf{S}_{FR}(\mathbf{S}_F^{-1}\vec{\mathrm{X}}_F + \mathbf{S}_R^{-1}\vec{\mathrm{X}}_R) \tag{2.17}$$

where $\vec{\mathrm{X}}_F$ and $\vec{\mathrm{X}}_R$ are the Fourier coefficients corresponding to the forward and reverse calculations; $\mathbf{S}_F$ and $\mathbf{S}_R$ are the forward and reverse run covariance matrices; and $\mathbf{S}_{FR}$, the covariance matrix associated with the forward/backward combination, is given by

$$\mathbf{S}_{FR} = (\mathbf{S}_F^{-1} + \mathbf{S}_R^{-1})^{-1} \tag{2.18}$$

The estimate takes into account data gathered both before and after the time of the estimate.

Figure 2.2 provides an example of the Kalman filter technique as applied to the CLAES N_2O data from September 1992. The map has been produced for the same day shown in Figure 2.1). To construct Figure 2.2, the following specific procedure for the Kalman filter was employed. First, the zonal means of the constituent fields at each latitude for the first 24 hours of data (starting at midnight on September 6^{th}) and the last 24 hours before the desired output time (noon September 8^{th} through noon September 9^{th}) were determined. Then the average rate of change of the zonal mean over the 3.5 day period was calculated and used to initialize $d\vec{\mathrm{X}}/dt$. To initialize the covariance matrix ($\mathbf{S}$), the variance of the first day's data (σ_0^2) on each latitude circle from the associated, initial zonal mean was determined. This estimate was assumed to describe the errors associated with each of the terms in the Fourier series. $\mathbf{S}$, therefore, was initially given by

$$\mathbf{S} = \sigma_0^2\mathbf{I} \tag{2.19}$$

where $\mathbf{I}$ is the identity matrix. Finally, the initial estimate of $d\mathbf{S}/dt$ was set to be twice $\mathbf{S}$. The large initial errors allowed the model to be heavily dependent on new measurements in the early stages of its evolution.

The same procedure has been applied in the reverse time direction using data gathered from noon on September 9^{th} through midnight September 13^{th}. The forward

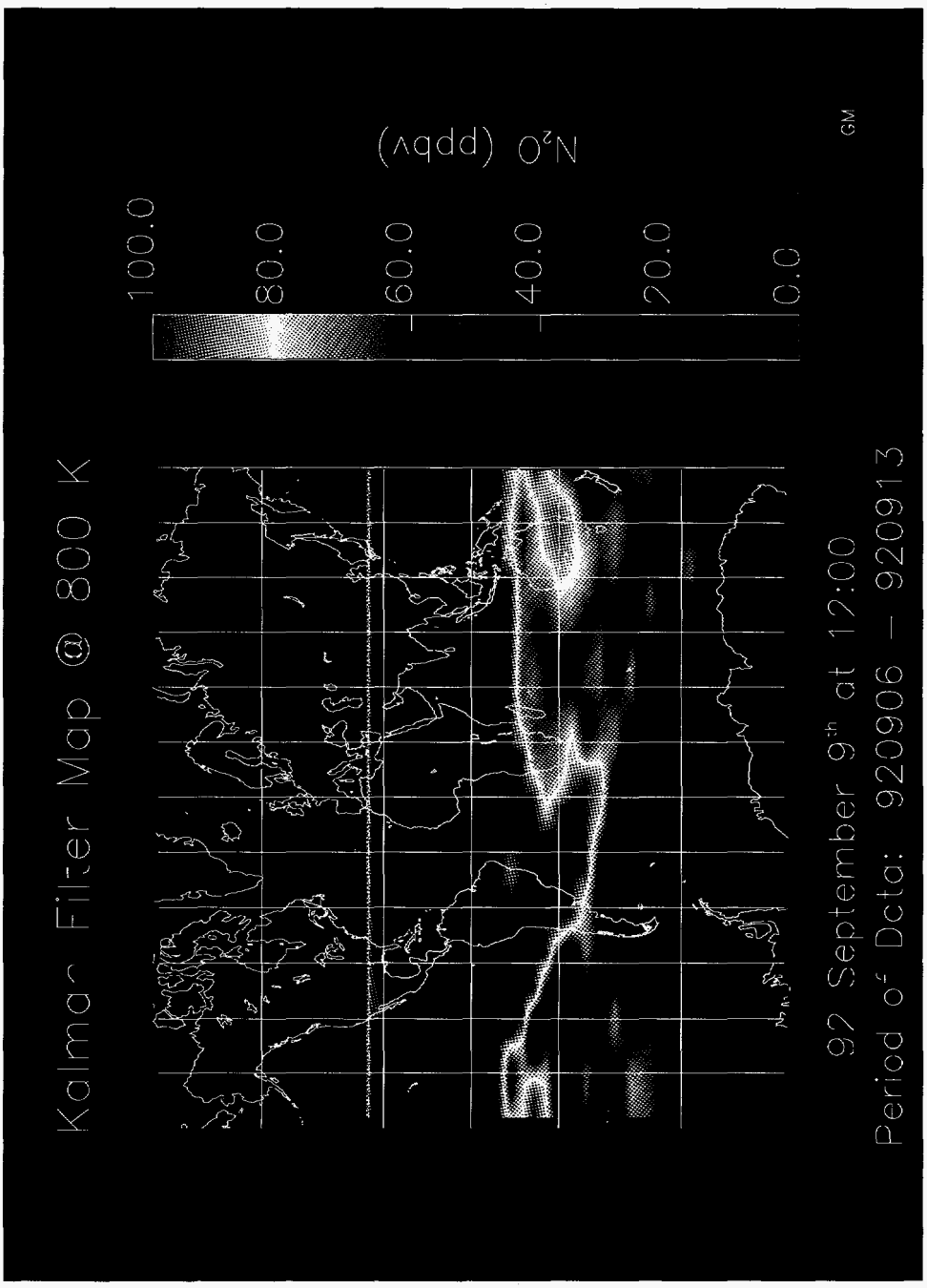

Figure 2.2 Kalman Filter Map of CLAES N_2O Data

and backward results have been combined using Equation 2.17 to produce the map of Figure 2.2.

The original error estimate for each measurement introduced into the model has been doubled. Part of the reason for this doubling lies in the resolution selected for the filter. The output grid is 4^0 latitude by 5^0 longitude. In determining the appropriate latitude circle for each measurement, the nearest grid latitude circle was used. This latitude circle may have been as far off as 2^0 from the actual measurement latitude. In regions of large constituent gradients, such a discrepancy can lead to large errors.

As with the other techniques (see Figures 2.1, 2.4, 2.5, and 3.1), the Kalman filter reproduces the gross dynamical structure. The wave-breaking event (the large tongue of high N_2O air extending from the tropics through the mid-latitudes), the vortex boundary (the large gradient between low N_2O values in the polar regions and mid-range values in the mid-latitudes), and the high N_2O region near Australia are successfully modeled. Noticeable also, however, are the consecutive spots of high and low N_2O values along latitude circles at mid-latitudes. Such features are unlikely to be real. Rather, these spots are likely places where the Fourier fit overshoots (undershoots) the actual constituent values. Fourier techniques are particularly susceptible to such ringing errors.

One important by-product of the Kalman filter technique is an estimate of the errors associated with its maps. Figure 2.3 shows the error estimate associated with the map of Figure 2.2.

In summary, therefore, the Kalman filter successfully characterizes an evolving constituent field through a mathematical technique. The procedure optimally incorporates new measurements using a weighting scheme based upon associated errors. The Kalman filter, however, applies very little of the physics of the real atmosphere in the production of its synoptic maps.

2.3 Salby-Fourier Mapping

Another technique developed for mapping asynoptic satellite data of any variable (temperature, humidity, trace gas mixing ratio, etc.) was suggested by *Salby* (1982 a,b) [41, 42]. The approach employs Fourier transforms of data gathered in space/time coordinates to zonal wavenumber/temporal frequency coordinates. In theory, the technique is quite straightforward: Fourier transform asynoptically gathered data in

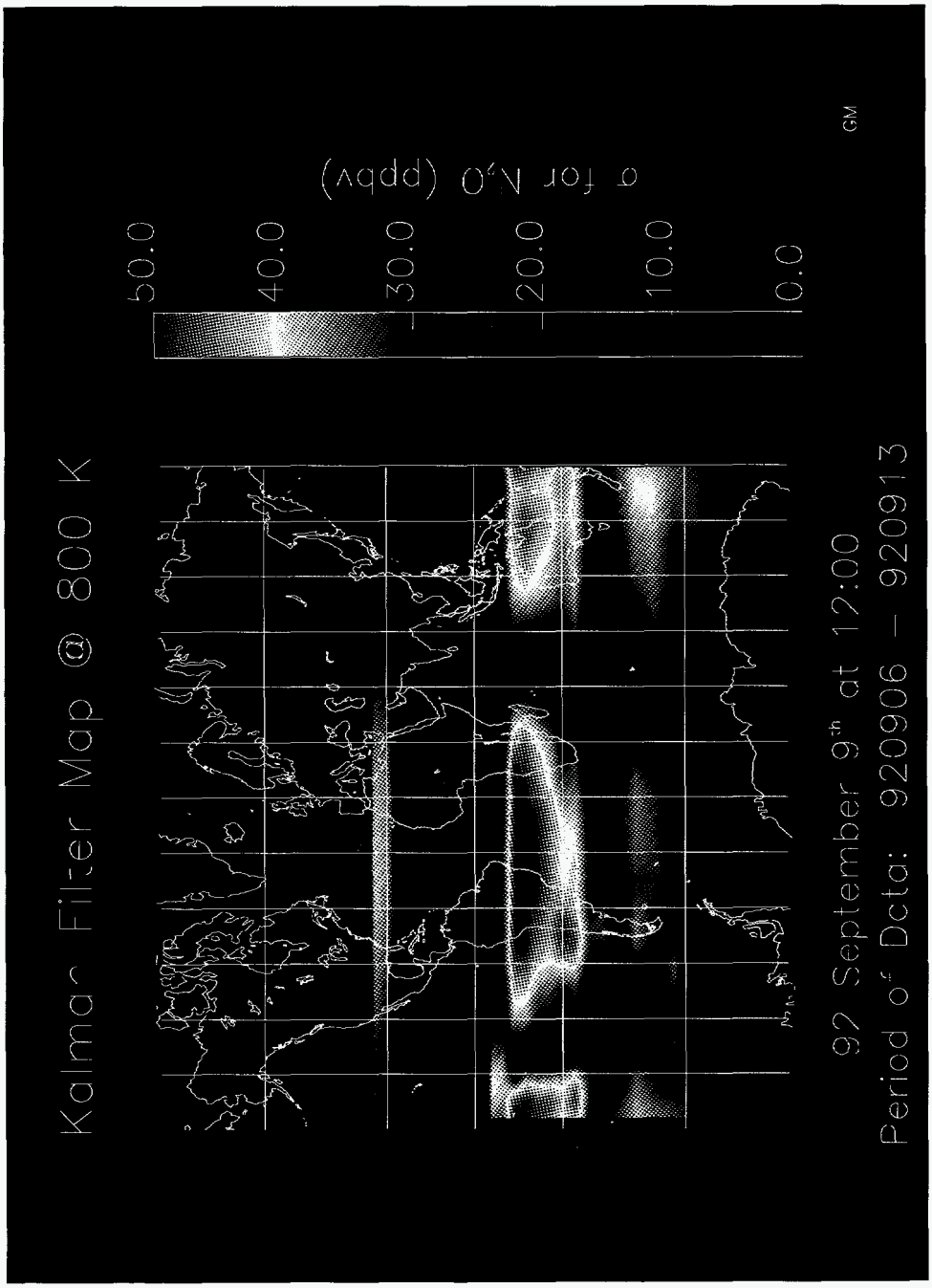

Figure 2.3 Kalman Filter Error Estimates for CLAES N_2O Data

space and time and reconstruct constituent distributions based on the zonal waves thus determined.

Following *Lait and Stanford* [20], for a constituent field $\psi(\lambda_j, t_k)$ specified at regular intervals in longitude (λ_j) and time (t_k) on a given latitude circle at a given altitude, the Fourier transform is given by

$$\Psi(m,\sigma) = \sum_{j=0}^{N-1} \sum_{k=0}^{M-1} \psi(\lambda_j, t_k) \exp[-i(m\lambda_j + \sigma t_k)] W \tag{2.20}$$

where W is a weighting function which takes into account the geometry of the grid selected. The transforms can be easily performed if the time and space components of Equation 2.20 are independent of one another. For asynoptically gathered satellite data, however, the longitudes of successive ascending (descending) nodes are time dependent and given by the simple relation

$$\lambda_{x,j} = \lambda_{x,0} - ct_{x,j} \tag{2.21}$$

where c represents the zonal speed of the satellite, x the ascending (descending) set of nodes, and j the node number.

Fortunately, by a carefully chosen rotation of the coordinate system, independent time and zonal transforms can be calculated. The grid created in the rotated space is parallel and orthogonal to the axes of the new coordinate space. The appropriate coordinates are given by

$$\begin{pmatrix} s \\ r \end{pmatrix} = \mathbf{R} \begin{pmatrix} \lambda \\ t \end{pmatrix} \tag{2.22}$$

where $\mathbf{R}$ is the rotation matrix given by

$$\mathbf{R} = \begin{pmatrix} \cos c^{-1} & -\sin c^{-1} \\ \sin c^{-1} & \cos c^{-1} \end{pmatrix} \tag{2.23}$$

In the rotated coordinate system, the Fourier transforms in Equation 2.20 are independent and, therefore, separable.

After finding the appropriate transforms in the rotated coordinate space, the Fourier coefficients are rotated back to the original time/latitude coordinate system. The constituent distribution at longitude λ_* on a given latitude circle at time t_* can then be derived by simply computing the inverse transform from $\Psi(m_*, \sigma_*)$ to $\psi(\lambda_*, t_*)$.

Figure 2.4 shows an example of a map generated using the Salby-Fourier technique.

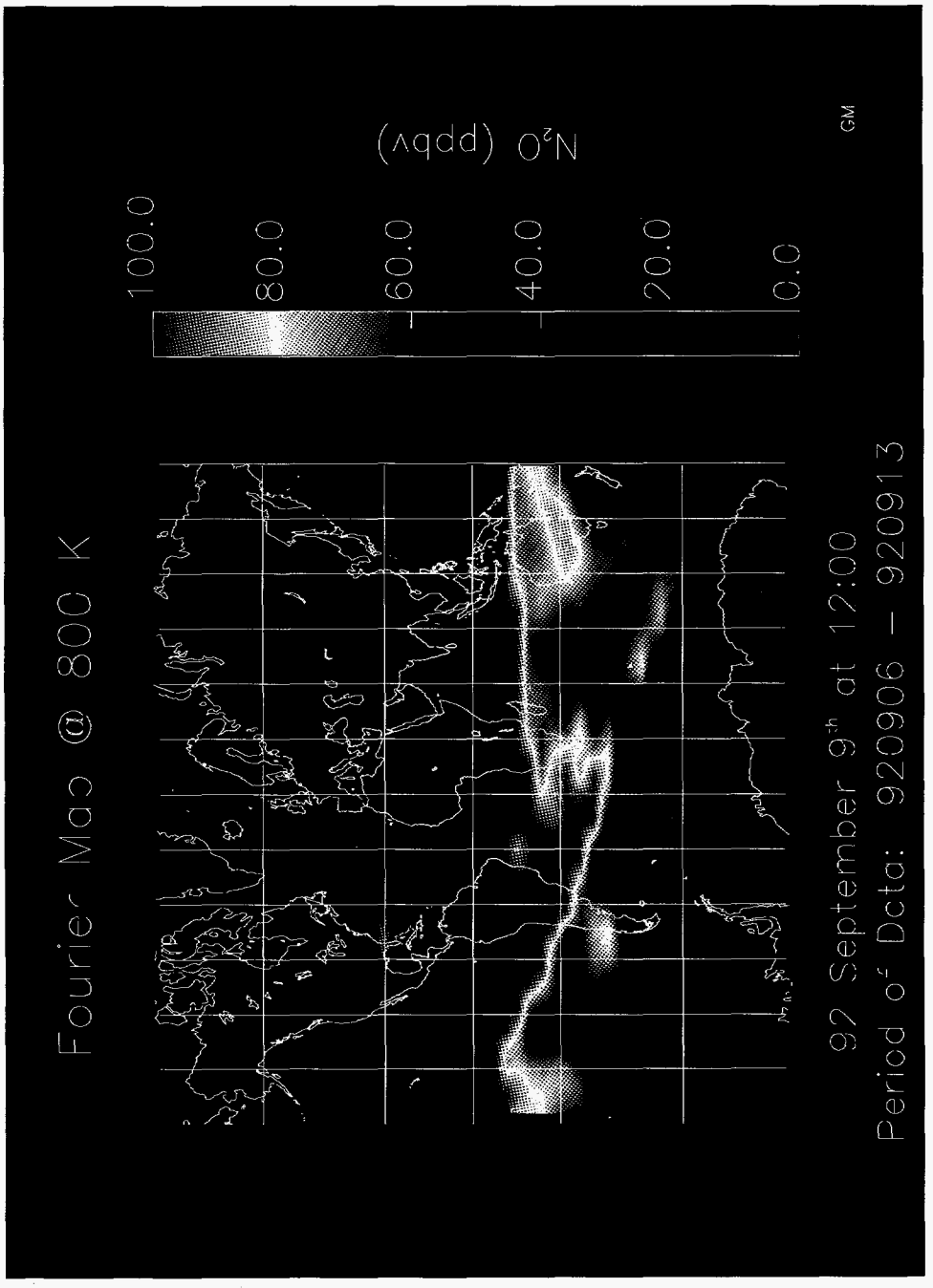

Figure 2.4 Salby-Fourier Map of CLAES N_2O Data

Again, the CLAES N_2O data gathered during the period September 6–12, 1992 have been interpolated to the 800 K potential temperature surface and mapped at noon on September 9. Many of the same features seen in the Kalman filter map of Figure 2.2 are reproduced here. Among these are the wave-breaking event, the vortex boundary, and, unfortunately, indications of Fourier series ringing. Further discussion of the dynamics of this time period and a comparison of the Salby map with maps produced with other techniques can be found in Section 4.1.

Among its strengths, the technique is particularly well suited for the processing of a large ensemble of data over a wide range of latitudes and altitudes. Errors introduced by discrepancies in retrieved data values along nearby scanning tracks or along lines of ascending or descending nodes are easily identified and removed. In addition, the technique preserves fast-moving waves and reduces aliasing due to high-frequency components and non-wave features [20].

The technique, however, is unable to detect waves of higher wavenumber than half the number of orbits per day. And poleward of 70^0–75^0, results become less reliable due to over- and undersampling of the data field by satellite instruments in these polar regions. The ascending and subsequent descending nodes grow closer and closer together at these polar latitudes, so the measurements are not necessarily independent of one another.

The technique also requires a continuous sequence of measurements over the period transformed. In regions of missing data, therefore, values must be supplied via interpolation. *Lait and Stanford* [20] have determined that cubic spline interpolation performs the task best in regions with limited numbers of missing data points along the orbital track or across orbital tracks, while linear interpolation is more appropriate for larger zonal gaps.

2.4 Constituent Reconstruction

Unlike the previously outlined techniques, the constituent reconstruction technique [46, 44] combines knowledge of the meteorological fields with trace gas measurements. In this way, the technique incorporates known atmospheric dynamics into its map products. Also unlike other techniques, reconstruction does not require large amounts of data to produce synoptic maps.

Based upon the idea of modified Lagrangian mean transport (see *McIntyre* [25]), reconstruction provides a powerful way to examine constituent data sets by trans-

forming to a coordinate system which greatly simplifies the dynamical components of the continuity equation:

$$\rho_t + \vec{v} \cdot \vec{\nabla}\rho = S \tag{2.24}$$

where ρ represents the constituent concentration (a function of position and time), ρ_t the time change in that concentration, $\vec{v}$ the wind velocity vector, and S the sources minus the sinks of the constituent.

The reconstruction technique exploits the quasi-conservative nature of air parcel motion with respect to potential vorticity (PV) and potential temperature (θ). (These quantities are discussed further in Appendix E.) To produce its map products, reconstruction averages measurements in [PV, θ] space (where PV and θ are derived from meteorological analyses). These averages are then assumed to define the trace gas value along entire [PV, θ] contours in real space. This very assumption, however, also implies that the technique cannot properly account for chemically active species or species injected locally in the flow field.

Constituent distributions determined in [PV, θ] space are inversely transformed back to latitude/longitude/altitude coordinates using the [PV, θ] fields from the meteorological analyses. In so doing, constituent concentrations in regions remote from direct observation can be estimated. The level of small scale structures reproduced, however, is entirely dependent upon that present in the meteorological [PV, θ] fields. The course resolution of these fields often severely limits the minimum size of the observable structure in the data.

Constituent reconstruction is most successful for dynamical periods over which PV and θ act as conserved quantities. In the lower stratosphere, a time scale of about 2 weeks is fairly typical for the conservation of these quantities. The technique has been successfully demonstrated with both aircraft [44] and balloon [19] data. Figure 2.5 shows the technique as again applied to N_2O data from CLAES during the September 1992 wave-breaking event.

Constituent reconstruction allows for comparison of measurements not collocated in space or time rather straightforwardly [44]. First, produce reconstructed maps with data from one instrument. Then resample it in the fashion of the second instrument. Of course, a similar procedure can also be used with Kalman filter and Salby-Fourier maps.

This comparison procedure can also be employed to assess the rate of diabatic and chemical processes. If a single instrument samples the region of interest for an extended period of time, maps can be made exclusively with data from the early

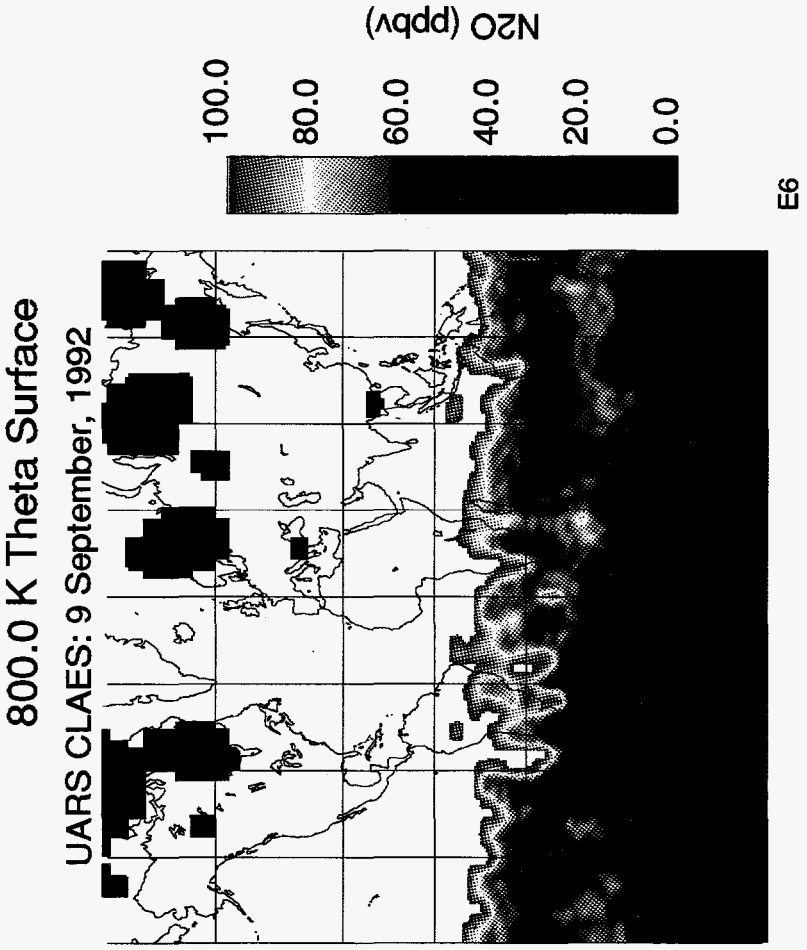

Figure 2.5 Reconstructed Map of CLAES N_2O Data

part of the period, then resampled and compared to data from the later parts of the period. Observed changes can then be attributed to non-conservative effects [46].

Chapter 3

Trajectory Mapping

Trajectory mapping is a new technique for producing synoptic maps from asynoptically gathered trace gas data. The technique combines several of the strengths of the techniques outlined in Chapter 2 with a minimum of assumptions.

Trajectory mapping employs a simple, two-dimensional model of atmospheric motions (known as the trajectory model, see Section 3.1) to advect measurements forward or backward in time from the point at which they were made. Meteorological analyses provide the winds which determine the magnitude and direction of parcel motion at each time step. In this way, like constituent reconstruction, the technique incorporates knowledge about the behavior of the real atmosphere.

By advecting a large number of measurements (all made at different times) to the same instant in time, a synoptic map of a constituent field can be constructed. Such a map is known as a "trajectory map." An example of a trajectory map showing the September 1992 wave-breaking event in CLAES N_2O is provided by Figure 3.1. In the figure, the larger dots represent measurements which have been added to the map within the 24 hour period around the synoptic map time, while the smaller dots represent measurements which have been advected more than 12 hours to the time of the synoptic map.

Unlike Kalman filtering, trajectory mapping does not require knowledge of the error associated with each measurement. Knowing these errors, however, is helpful in assessing the validity of trajectory maps. Since both measurement and meteorological errors are present in trajectory mapping, determining the actual errors associated with trajectory maps can be quite complicated (as outlined in Section 3.2 below).

The trajectory mapping technique is relatively unaffected by missing data points (such as periods of satellite data drop-out) which present difficulties for the Salby-Fourier technique. And trajectory maps can be produced outside of periods during which measurements are made, so long as the wind field analyses exist.

The ability of the technique to produce maps outside data gathering periods proves particularly helpful when examining the evolution of atmospheric events. Events

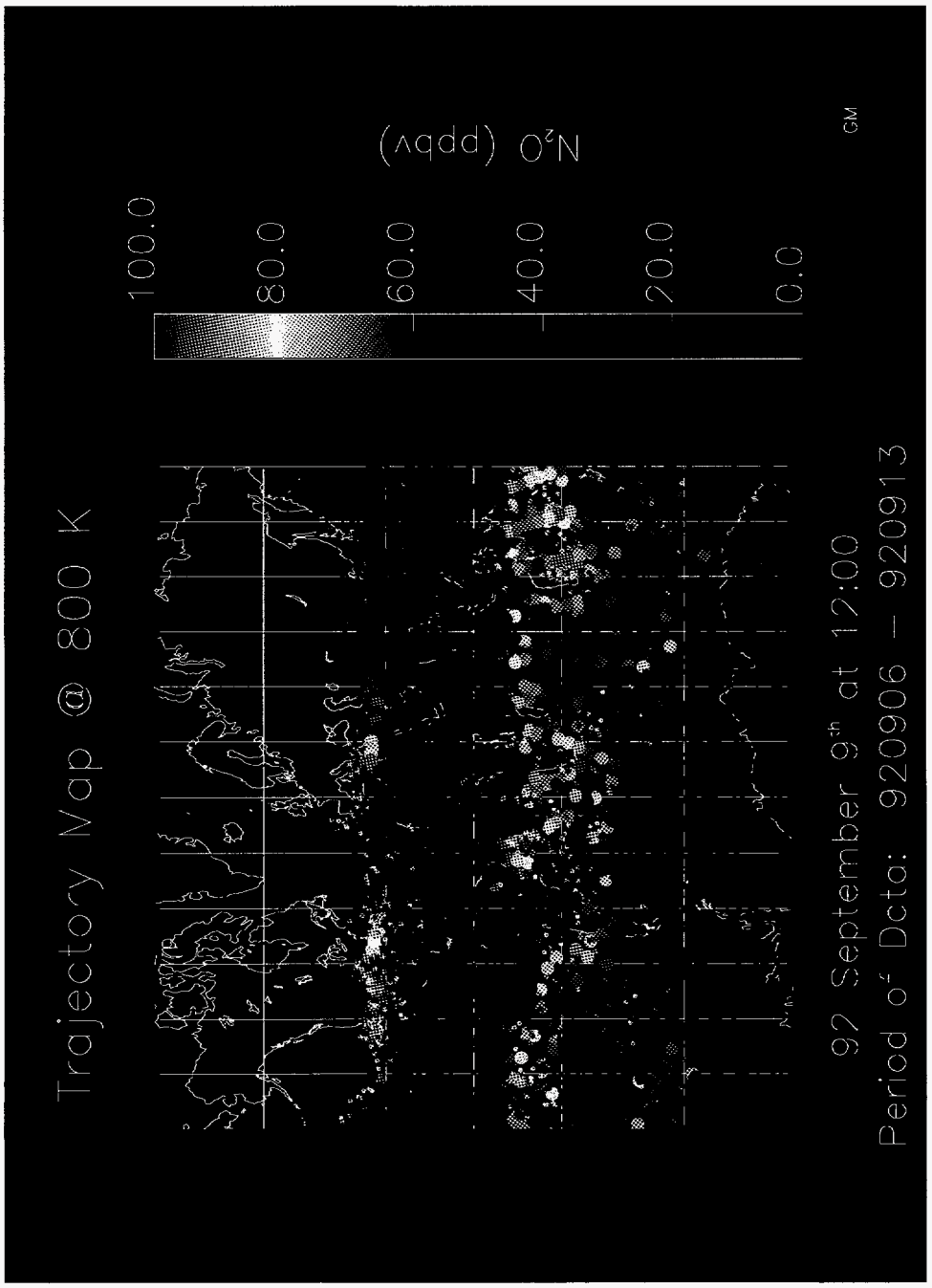

Figure 3.1 Trajectory Map of CLAES N_2O Data

which occur, at least in part, outside data gathering periods can be more clearly explained using the trajectory mapping technique (see Section 4.1).

The trajectory technique demonstrates several additional strengths. First, its synoptic maps are generated easily and straightforwardly from asynoptic data. Second, the technique is not sensitive to irregular observational strategies (unlike the Salby Fourier technique). Third, the technique allows for comparison of non-coincident or non-collocated measurements. Fourth, the technique makes no assumptions about the amount of mixing occurring in the real atmosphere (unlike constituent reconstruction, which assumes uniformly mixed [PV, θ] tubes). Fifth, the technique applies no artificial, mathematical constraints to the data nor does it require the binning of data in any way (unlike the Kalman filtering, Salby-Fourier, and reconstruction techniques).

The ability of trajectory mapping to compare non-coincident and non-collocated measurements facilitates data validation studies. For example, the comparison between aircraft and satellite measurements, which previously relied on overpasses, can be performed with higher statistical robustness using the trajectory mapping technique (see Section 4.2.1). As another example, we have employed trajectory mapping to intercompare Microwave Limb Sounder (MLS) and the Halogen Occultation Experiment (HALOE) H_2O measurements (see Section 4.2.1). For more information on the UARS instruments, see Appendix A.

The trajectory mapping technique has a few disadvantages compared to the other methods. First, unlike the Kalman filtered, Salby-Fourier, or reconstructed maps, trajectory maps are not uniformly gridded. Second, the quality of trajectory maps is substantially dependent upon the quality of the meteorological fields. Missing or inaccurate meteorological data degrade the accuracy of the advected measurements. Constituent reconstruction shares this dependence on the meteorological fields while Kalman filtering and the Salby-Fourier technique (which rely strictly on a mathematical fit to the measurements) avoid such reliance entirely.

Clearly, an understanding of the accuracy of the trajectory computation is critical to assessing the value of the resultant maps. A considerable portion of this Chapter, therefore, will be devoted to evaluating errors associated with the technique.

3.1 The Trajectory Model

The backbone of the trajectory mapping technique is the trajectory model. Using prescribed wind fields, this model mathematically simulates the motion of air parcels

in the atmosphere. The model can advect parcels either forward or backward in time and can be run either isentropically or diabatically.

Isentropic trajectories are computed through successive spatial and temporal interpolation of the wind fields to parcel locations. Meteorological fields are specified on a regular latitude/longitude/pressure grid at regular time intervals. Several different analyses of meteorological fields are available for use in the trajectory model (see Table 3.1), each with its own spatial and temporal resolution. These data sets are discussed in greater detail in Appendix D.

To derive values of the meteorological fields at parcel locations, a series of interpolations is performed. The fields are interpolated vertically from pressure surfaces to the potential temperature surface of interest (for a further discussion of potential temperature, see Appendix E). This procedure produces a 2–D latitude/longitude grid of meteorological data on an isentropic surface. The 2–D isentropic data are then interpolated to the parcel positions using either a linear or cubic spline interpolation scheme along latitude circles and meridians. Finally, the meteorological fields are linearly interpolated in time to the current model time.

After determining the winds, the model moves the parcels isentropically forward or backward in time using a fourth order Runga-Kutta scheme such that

$$\lambda_{i+1,j} = \lambda_{i,j} + \frac{\Delta t}{6}\left(d\lambda_1(i,j) + 2d\lambda_2(i,j) + 2d\lambda_3(i,j) + d\lambda_4(i,j)\right) \tag{3.1}$$

$$\phi_{i+1,j} = \phi_{i,j} + \frac{\Delta t}{6}\left(d\phi_1(i,j) + 2d\phi_2(i,j) + 2d\phi_3(i,j) + d\phi_4(i,j)\right) \tag{3.2}$$

where λ represents the latitude and ϕ the longitude and where the functions $d\lambda_k$ are defined by

$$d\lambda_1(i,j) = a^{-1}v\left(i, \phi_{i,j}, \lambda_{i,j}\right) \tag{3.3}$$

$$d\lambda_2(i,j) = a^{-1}v\left(i + \frac{\Delta t}{2}, \phi_{i,j} + d\phi_1(i,j)\frac{\Delta t}{2}, \lambda_{i,j} + d\lambda_1(i,j)\frac{\Delta t}{2}\right) \tag{3.4}$$

$$d\lambda_3(i,j) = a^{-1}v\left(i + \frac{\Delta t}{2}, \phi_{i,j} + d\phi_2(i,j)\frac{\Delta t}{2}, \lambda_{i,j} + d\lambda_2(i,j)\frac{\Delta t}{2}\right) \tag{3.5}$$

$$d\lambda_4(i,j) = a^{-1}v\left(i + \Delta t, \phi_{i,j} + d\phi_3\Delta t, \lambda_{i,j} + d\lambda_3\right) \tag{3.6}$$

and the functions $d\phi_k$ are given by

$$d\phi_1(i,j) = \frac{u\left(i, \phi_{i,j}, \lambda_{i,j}\right)}{\left(a\cos(\lambda_{i,j} + d\lambda_1\frac{\Delta t}{2})\right)} \tag{3.7}$$

Data Set	Grid Spacing (lon X lat)	Vertical Resolution # levels (range)	# of Analyses (per day)
NMC (National Meteorological Center)	5^0 X 2^0	18 (0.4 to 1000 mb) (55 km to the surface)	1
UKMO (United Kingdom Met Office)	3.75^0 X 2.5^0	18 (0.4 to 1000 mb) (55 km to the surface)	1
GSFC (Goddard Space Flight Center)	5^0 X 4^0	18 (0.4 to 1000 mb) (55 km to the surface)	4

Table 3.1 Meteorological Data Sets

$$d\phi_2(i,j) = \frac{u\left(i+\frac{\Delta t}{2}, \phi_{i,j} + d\phi_1(i,j)\frac{\Delta t}{2}, \lambda_{i,j} + d\lambda_1(i,j)\frac{\Delta t}{2}\right)}{\left(a\cos(\lambda_{i,j} + d\lambda_2\frac{\Delta t}{2})\right)} \tag{3.8}$$

$$d\phi_3(i,j) = \frac{u\left(i+\frac{\Delta t}{2}, \phi_{i,j} + d\phi_2(i,j)\frac{\Delta t}{2}, \lambda_{i,j} + d\lambda_2(i,j)\frac{\Delta t}{2}\right)}{\left(a\cos(\lambda_{i,j} + d\lambda_3\frac{\Delta t}{2})\right)} \tag{3.9}$$

$$d\phi_4(i,j) = \frac{u\left(i+\Delta t, \phi_{i,j} + d\phi_3\Delta t, \lambda_{i,j} + d\lambda_3\right)}{\left(a\cos(\lambda_{i,j} + d\lambda_4\frac{\Delta t}{2})\right)} \tag{3.10}$$

for parcel j at time i, with a being the radius of the Earth (6.37×10^6 m), u the East/West wind velocity, and v the North/South wind velocity.

The trajectory model contains a number of adjustable parameters: time step, diabatic heating, meteorological field, and the potential temperature surface. Studies to determine the relative impacts of different choices for these parameters are outlined below and in Section 3.2.

Schoeberl and Sparling [47] have examined the growth of the computational error of the trajectory model as a function of the size of the time step. For computations presented here, a step size of 0.01 day has been chosen, resulting in errors of about 10^{-5} degrees per day in the latitudinal and longitudinal directions (see Figure 3.2).

Parcel motion relative to isentropic surfaces can be estimated using diabatic heating rates. The model employs the output from an off-line computation of the atmospheric heating rates to compute the net heating of each parcel along its isentropic trajectory. The net heating rates used here have been provided by radiative trans-

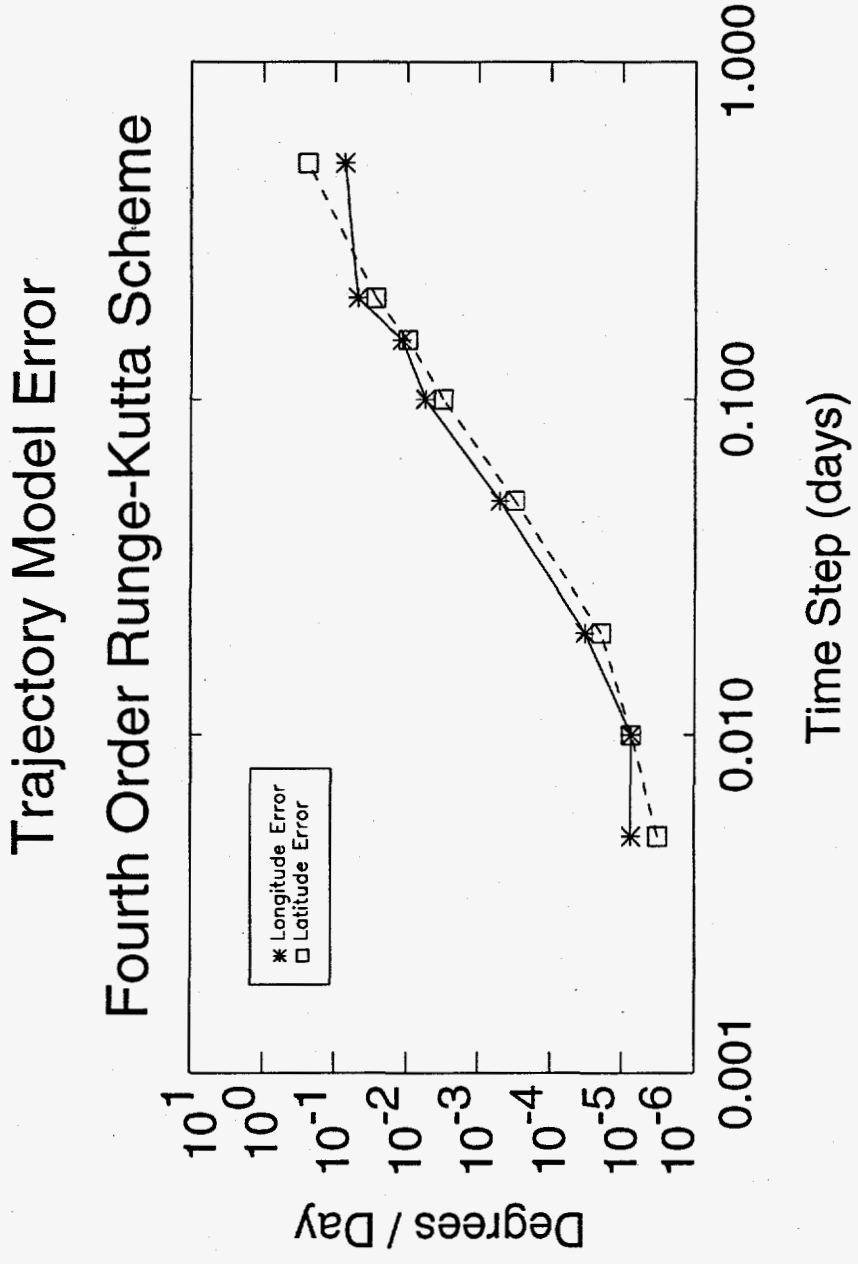

Figure 3.2 Trajectory Errors as a Function of the Model Time Step

fer calculations described by *Rosenfield* [39]. In the diabatic mode, therefore, the trajectory model is capable of producing 3-D trajectories.

For computations involving large numbers of parcels (such as those required for most trajectory maps), such 3-D computations are time consuming and impractical. Because small changes in potential temperature seldom change meteorological fields dramatically, the diabatic technique as applied in the studies presented here discretizes the isentropic surfaces on which meteorological fields are calculated. This discretization reduces the number of vertical interpolations of meteorological data the model must perform. The diabatic model run time, therefore, is greatly reduced. For example, given a parcel which initially begins on an isentropic surface θ_i, the trajectory model will advect this parcel using meteorological data from this isentropic surface so long as its potential temperature remains within a specified $\pm\delta\theta$. Once the associated potential temperature of the parcel reaches $\theta_i \pm \delta\theta$, the parcel trajectory is calculated with meteorological data from the isentropic surface $\theta_{i\pm1}$, where $\theta_{i\pm1} = \theta_i \pm 2\delta\theta$. Thus, the model approximates 3-D motion.

The trajectory model employed in this study has been demonstrated reliable through a number of tests. In particular, the model successfully preserves zonal flow for the imposed solid body rotation wind field about the pole

$$\mathrm{u} = \mathrm{u}_0 \cos(\phi) \tag{3.11}$$

$$\mathrm{v} = 0 \tag{3.12}$$

Tipping such a solid body rotation wind field off the pole also produces expected results.

The trajectory model has a wide variety of useful applications. For example, weather balloon flights can be simulated using isobaric trajectory calculations [6]. *Schoeberl et al.* [46] have employed the trajectory technique to estimate the 2-D eddy diffusion coefficient for the 1987 Southern hemisphere and 1989 Northern hemisphere winter vortices. In another study, *Schoeberl et al.* [45] demonstrated the dependence of the measured ClO content of a parcel upon the minimum previously encountered air parcel temperature (determined by back trajectory calculations). And *Sparling et al.* [49] outlined a strategy to examine the potential effects on the stratosphere of the proposed high speed civil transports (HSCT's) using a trajectory technique.

Related to the trajectory technique is the study of atmospheric dynamics through the advection of material contours. The first such scheme was developed by *Dritschel* [7]. He assumed an unbounded, inviscid, incompressible fluid whose motion was

strictly constrained to conserve vorticity. To ensure the motion conserved vorticity, the velocity field was derived from the vorticity field. In regions of high curvature or large velocity gradients, parcels were added to the contour to better observe its evolution. Parcels were removed from the calculations where and when nearby contours converged.

More closely related to the trajectory technique discussed in this work is the contour advection scheme developed by *Waugh and Plumb* and *Plumb and Waugh* [57, 56, 31]. They adapted *Dritschel's* contour advection scheme to use meteorological wind field analyses rather than the winds derived from the conservation of vorticity. The contour advection technique allows closer examination of the evolution of fine scale atmospheric structures, such as those seen in aircraft in situ trace gas measurements [56, 31].

Clearly, the trajectory technique has demonstrated a number of useful applications. The remainder of this thesis explores the use of a trajectory model in the construction of synoptic maps from satellite data, an application first suggested and employed by *Pierce et al.* [30]. The combination of trajectory calculations and satellite retrieved constituent data provides a powerful tool for a variety of work. Satellite data accuracy can be determined through comparison with other measurements, including those not necessarily made at the same place or time as the original measurement. Satellite data precision can also be studied through an examination of the internal consistency of an individual data set. Furthermore, the quality of the meteorological fields can be estimated by determining the dependence of results from the above tests upon the wind field data set employed. Each of these applications are explored in Chapter 4. First, however, an assessment of errors associated with the technique is provided.

3.2 Errors in Trajectory Mapping

As mentioned earlier in this Chapter, the validity of trajectory mapping is fundamentally dependent on the accuracy of the trajectory calculations. The information about an individual parcel location degrades with time owing to the cumulative effects of errors along each parcel's trajectory. The spatial distribution of a large ensemble of parcels, however, is less sensitive to these errors, as we show below. A fundamental problem, therefore, is to determine a reasonable upper bound for the length of time

over which parcel trajectories are accurate. A related problem concerns the maximum age for which measurements included in trajectory maps can be considered valid.

In exploring these problems, we shall examine and evaluate four potential sources of trajectory mapping errors: computational error, trace gas measurement uncertainties, diabatic/adiabatic calculational differences, and meteorological errors. The meteorological errors include differences in meteorological analyses.

3.2.1 Computational Error

The first of these four error sources, the computational error, has been examined and found to be quite small for the fourth order Runge–Kutta time integration scheme used here [47]. *Schoeberl and Sparling* demonstrated the magnitude of this error to be 10^{-5} degrees/day for the time step of 0.01 day used in all the studies shown in this thesis (see Figure 3.2).

To derive this quantity, they advected a group of parcels forward in time for n days. Their locations on day n then initialized back trajectories through the same set of n days. Their final and initial locations were compared. Since all other conditions for the forward and backward runs were identical, the resulting discrepancies must be due entirely to computational errors. Furthermore, the nature of the calculation insures that the computational errors consist only of numerical round-off errors. Given the results of *Schoeberl and Sparling*, these numerical round-off errors can be ignored, especially as compared to the magnitudes of the errors from other sources.

3.2.2 Trace Gas Measurement Uncertainties

The second of the error sources, measurement uncertainties, consists of two basic components: the error in the measured constituent mixing ratio and the subsequent accumulation of errors during model advection. The former of these two errors is a result of the measurement technique and remains a constant with time, while the latter is a result of the the trajectory technique and grows with time.

Before exploring the errors resulting from the technique, however, consider the limitations of the satellite measurements themselves. Inaccurate measurement of the constituent and improper pressure registration both contribute to erroneous values. (For further discussion of these errors as related to the UARS instruments, see Appendix A.)

In addition, the horizontal scale of the satellite measurement can affect the correlation of recent satellite measurements with older, advected measurements. When the scale of atmospheric features becomes small compared to the scale of the satellite measurements, the features will tend to be averaged out. For example, filaments of vortex material which peel off the vortex edge and stretch into mid-latitudes eventually become quite thin, as in the case of Figure 3.3. In this Figure, vortex material (as defined by material inside the -2.6×10^{-4} K m^2 / kg / sec potential vorticity (PV) contour) is represented by the white cross-hatched region. Note the very fine scale structure of the vortex material, particularly that of the filament (thin white line) wrapping around the bottom edge of the vortex and into the lower right quadrant of the Figure.

So long as the horizontal dimension of the atmospheric features is on the order of the satellite footprint dimension, the satellite can detect them. As filaments evolve, however, they grow very long and very thin, as discussed by *Pierce and Fairlie* [29] and as can be seen in Figure 3.3. Satellite instruments gradually lose their ability to detect these filaments because the volume of air over which the measurements are made consists less and less of filamentary air. In other words, satellite measurements tend to blur regions of sharp constituent gradients. As a result, in Figure 3.3, not all the measurements (represented by the colored dots) around the thin filament are indicative of vortex air.

As another example, examine the time sequence of trajectory maps shown in Figure 3.4. This Figure depicts the wave-breaking event first reported by *Randel* [34] as seen in the CLAES N_2O data at the 800 K potential temperature surface (30 km) As the wave (represented by the tongue of high N_2O (red) material extending into mid-latitudes from the tropics) breaks, the feature is stretched out into a narrow filament. Nearby, newer satellite measurements (represented by the larger dots) begin to decrease in value as compared to the older advected measurements (represented by the smaller dots). Further discussion of both of these Figures can be found in Section 4.1.

For the trajectory mapping technique, instrumental limitations imply that the older parcels which have been pulled out in filaments may disagree with nearby, newer parcels. The disagreement may be due more to the instrument's inability to detect very fine scale atmospheric features than to an error in the technique.

Certainly, however, the filaments do eventually mix with their surroundings, making the older parcels and, hence, the technique inaccurate. Since the trajectory model

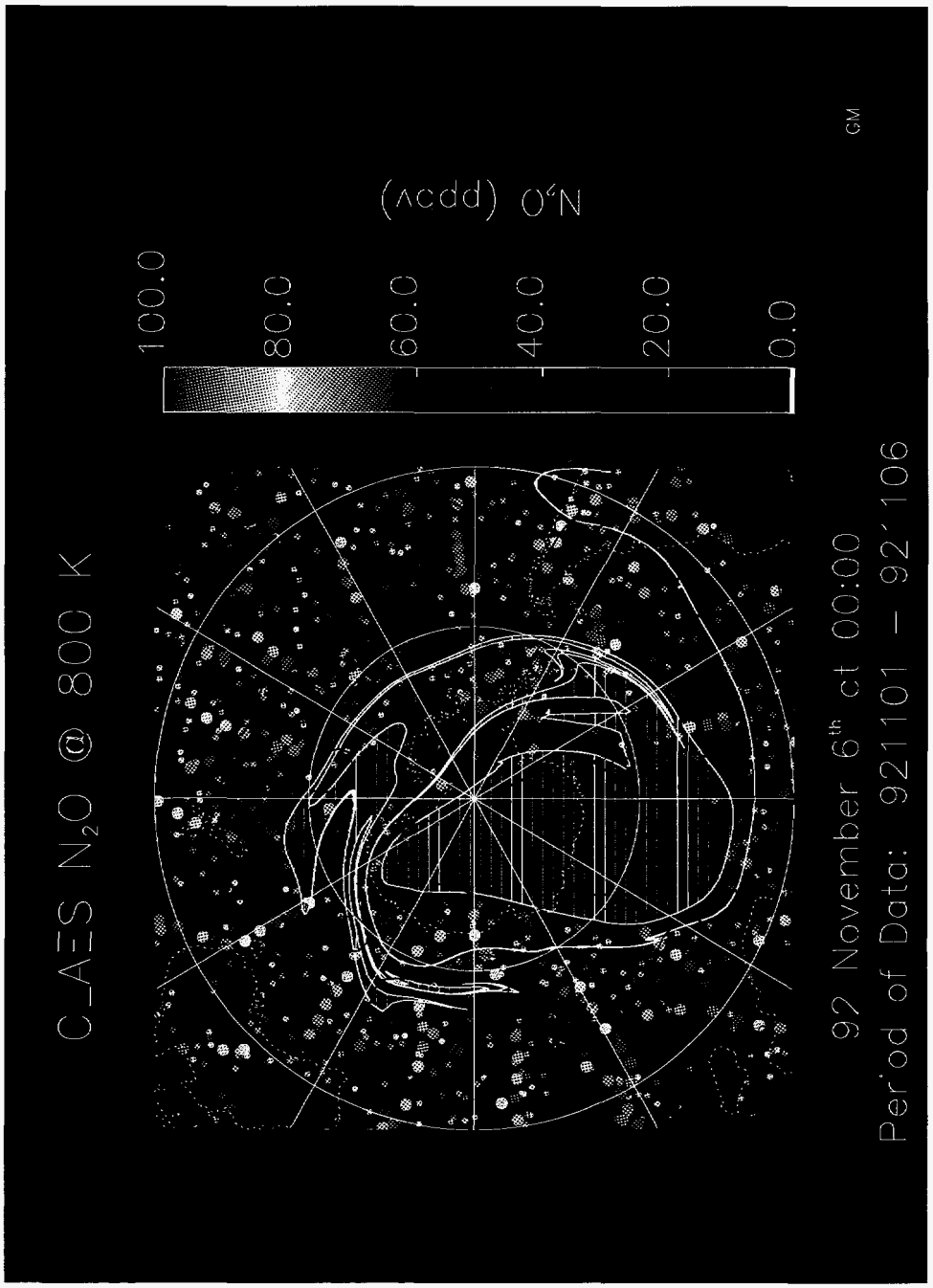

Figure 3.3 Trajectory Map of CLAES N_2O Showing Vortex Filamentation

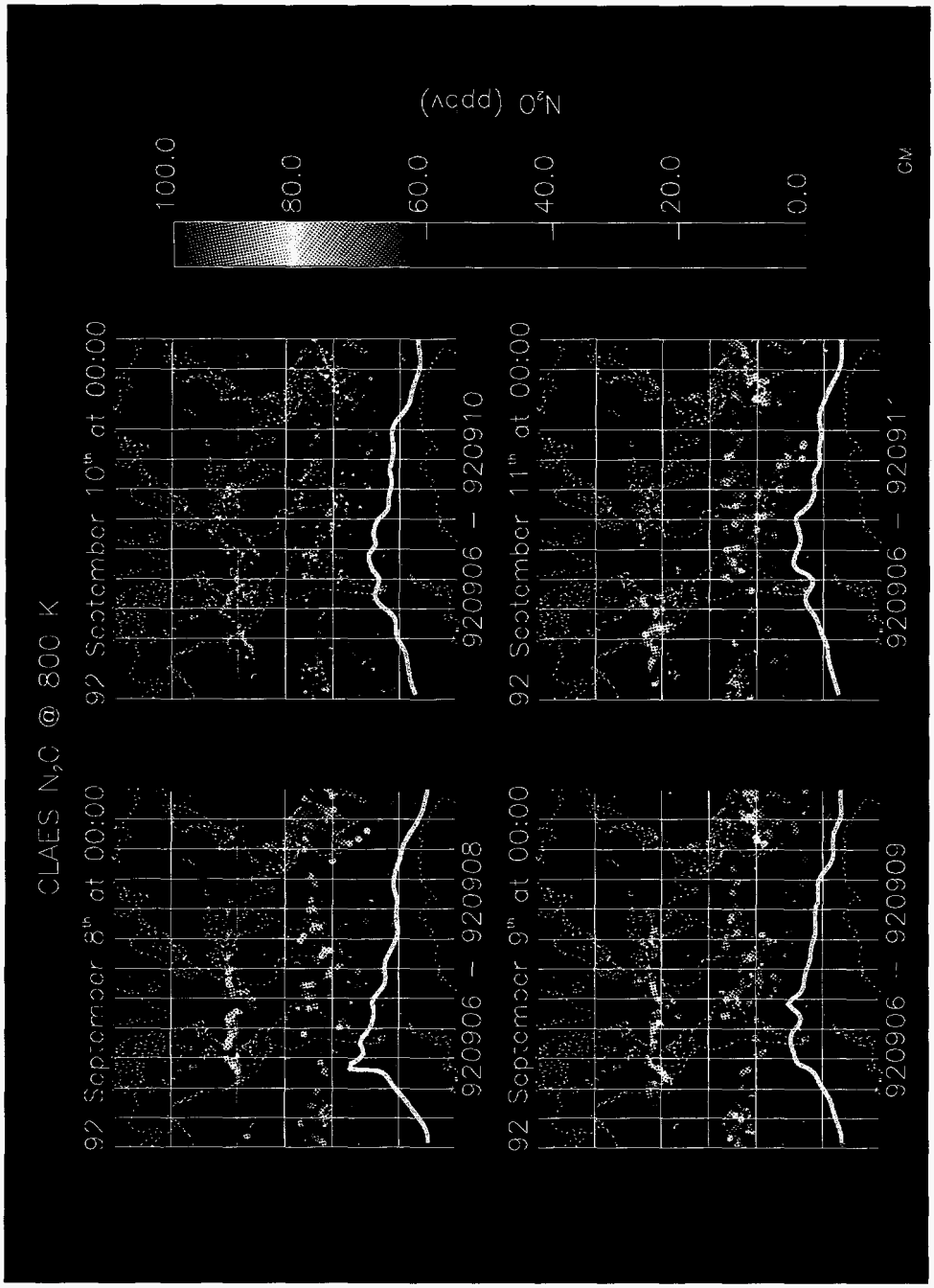

Figure 3.4 September 1992 Wave Breaking Event Seen in CLAES N_2O Data

uses only the wind field to make its predictions (ignoring chemical reactions and mixing), parcels necessarily lose accuracy with age.

In addition to these quantitative measurement uncertainties, uncertainties in the location of each measurement and in the location of gradients in the meteorological fields also adversely affect trajectory maps (also see Section 3.2.4). If a single parcel is initialized in the trajectory model for each measurement, the uncertainty in the location of the measurement can increase rapidly with time, especially when the parcel is advected through chaotic regions or regions of high wind shear in the flow field.

The vertical and horizontal uncertainties in the location of measurements are accounted for differently. The initial uncertainty in the horizontal location of a measurement can be taken into account by initializing a group of parcels over a region with dimensions on the order of the spatial uncertainty (see Section 3.3) for each measurement. Alternatively, to keep computational costs low, a single parcel can be used to initialize the measurement provided that it is removed from the map when the uncertainty in its location (which increases with time) exceeds the grid spacing.

The initial horizontal uncertainty in the location of a measurement is given by the horizontal scale of the satellite footprint. This compact region will eventually become highly distorted and drawn out under the shearing effects of the winds [29]. The shearing causes the predicted location of a measurement to become more uncertain with time.

To get a sense of just how rapidly a parcel can be sheared apart by gradients in the wind field, "megaparcels" were initialized on a uniform, equal area grid. Megaparcels consisted of a central parcel surrounded by four additional parcels (sub-parcels) located 20 km away on the points of the compass (i.e. one parcel 20 km East, one 20 km North, etc.). The 40 km megaparcel diameter was chosen to coincide approximately with the width of space over which a single CLAES measurement is made.

Pierce et al. [30] first suggested and employed such a megaparcel technique, advecting a large number of tightly packed sub-parcels for each measurement in the HALOE (Halogen Occultation Experiment, see Appendix A.1) data set. Statistically, the technique is equivalent to advecting a spatial probability distribution for the parcel location. Initially compact, this distribution disperses with time. The rate of dispersion can be approximated by the rate of separation of the megaparcels. Figure 3.5 shows the fraction of megaparcels whose members all remain within 500

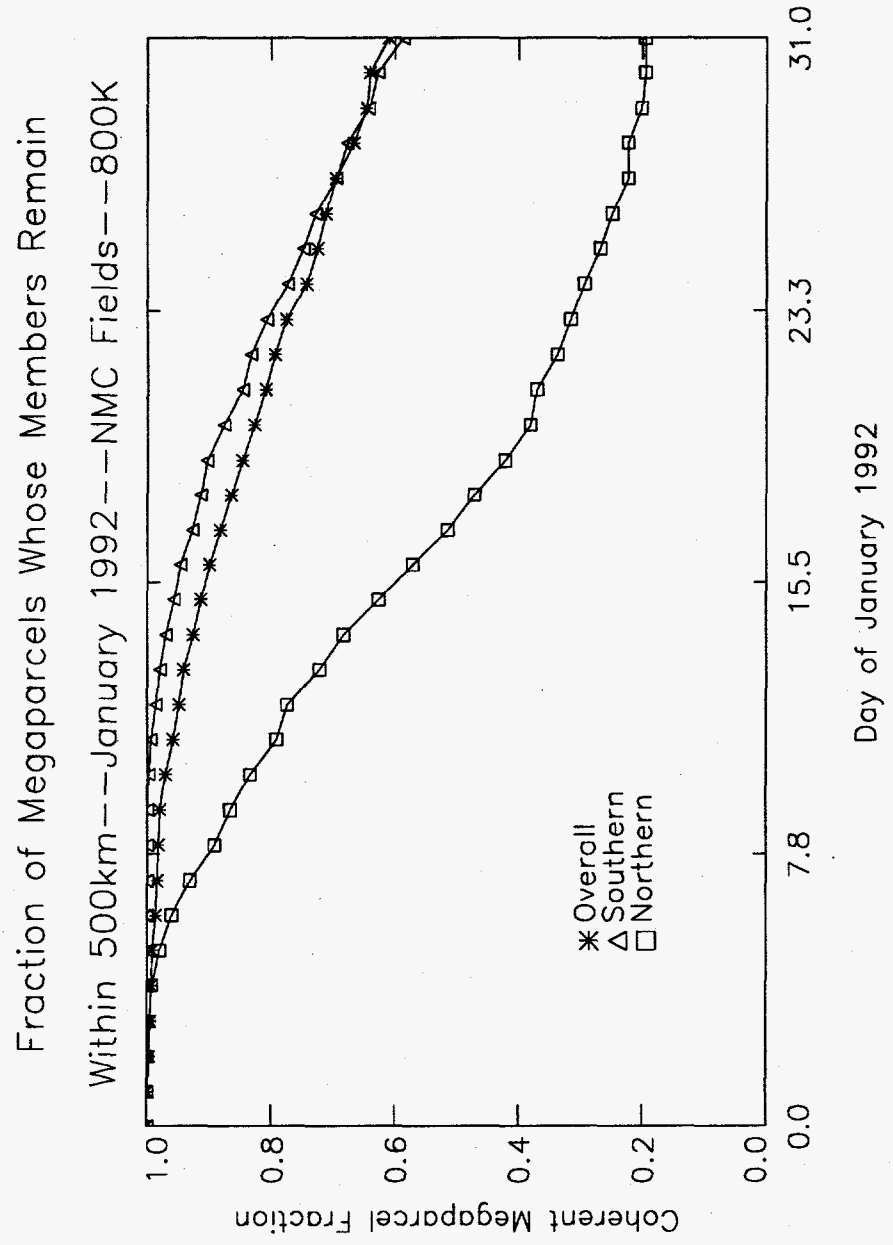

Figure 3.5 Megaparcel Separation Test

km (or approximately the initial grid spacing distance) of their associated central parcels as a function of time.

The megaparcel test was performed in both hemispheres on the 800 K potential temperature surface (30 km) during January and June (not shown) 1992 with meteorological data from the National Meteorological Center (NMC, see Appendix D.1): January (Figure 3.5). The tests revealed that more than half the megaparcels in the winter hemisphere remain compact for 15–20 days. In the summer hemispheres, the tests indicated that more than half the megaparcels remain compact for the entire period. Such results do not exclude the possibility of large shearing. The distributions of the sheared separation distances (see Figure 3.6 and the discussion below) show, however, that the majority of megaparcels do remain compact.

Clearly, the rate of decrease in the fraction of parcels remaining close together is dependent upon the amount of horizontal wind shear present in the meteorological fields. The winter hemisphere, as expected, exhibits more shearing. Because the 800 K potential temperature surface (30 km) lies close to the jet core in the winter hemisphere, conditions of maximum wind shear are present in these tests. This study, therefore, probably represents a "worst case" scenario.

Figure 3.6 shows the distributions on two different days during January in the Northern Hemisphere, the worst case observed in the study. After 8 days, the Figure suggests that nearly all the parcels remain compact to within a few grid boxes. Even after 31 days, the most probable separation distance is on the order of or less than the grid spacing (approximately 500 km longitudinally at the equator). Therefore, even in the "worst case" scenario, 6–10 days appears to be a reasonable estimate for accurate parcel lifetimes. The June distribution (not shown) is similarly weighted toward small separation distances.

On the other hand, one might expect that such estimates are quite generous, especially considering the coarse time interval and grid spacing of the meteorological fields used in the tests of Figures 3.5–3.6. The 24–hour NMC meteorological fields used in this study are defined for grid points every 2^0 of latitude and every 5^0 of longitude. Since these shearing tests examined the separation of parcels initially only 40 km apart (or about one-fifth of a grid box), the information required to drive the observed shearing must be interpolated from the larger scales. *Waugh and Plumb* [57], however, have demonstrated that the grid spacing of the stratospheric meteorological fields can be quite coarse without significantly affecting the trajectory calculations over periods of a week or longer. In fact, they determined that it is the large scale

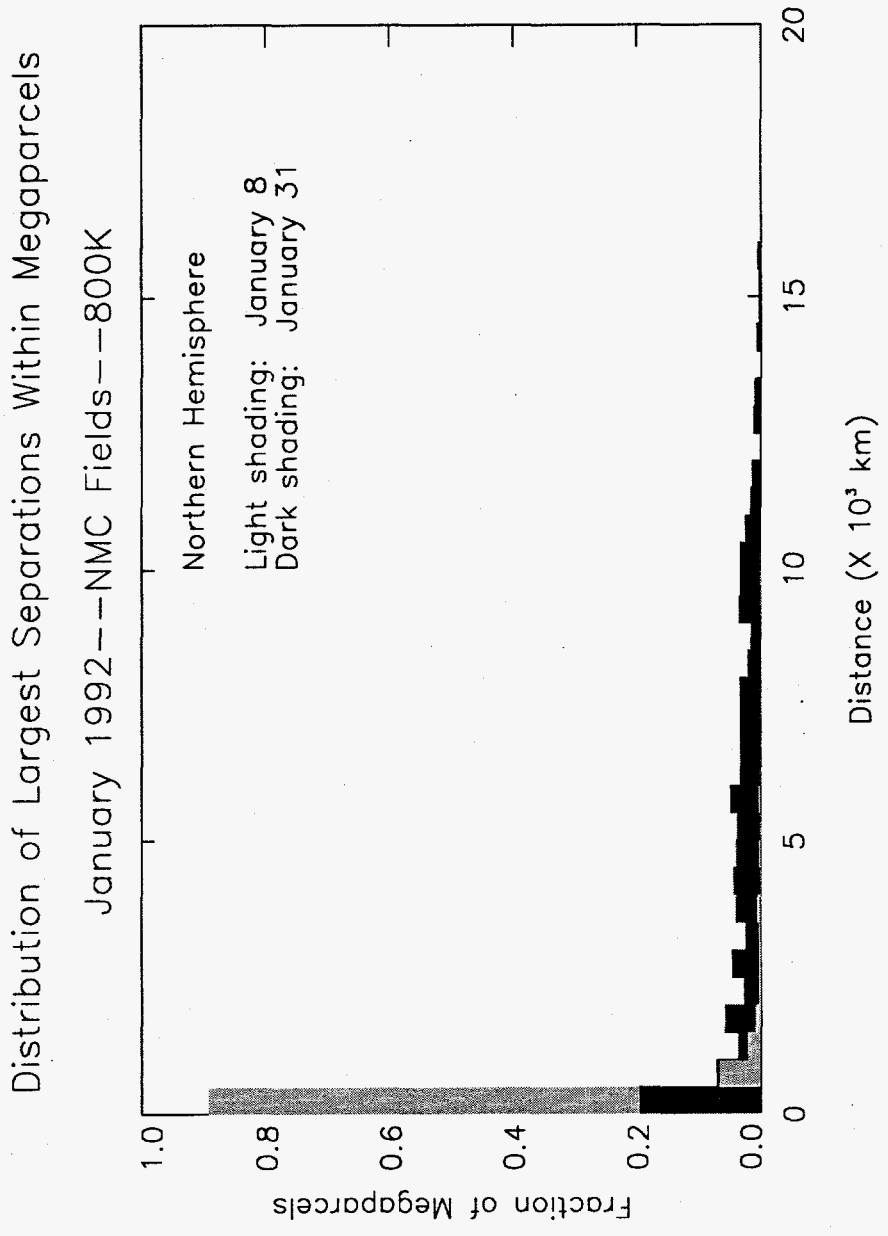

Figure 3.6 Distribution of Maximum Separation Distances

structures in the wind fields which are mainly responsible for driving the small-scale features, such as those observed in contour advection studies. Furthermore, they suggest that the temporal frequency of the meteorological analyses used is far more important than the spatial resolution for the accurate generation of such features [57]. Such conclusions support the estimates of Figures 3.5–3.6.

Figures 3.5–3.6 also suggest that the horizontal shearing problem can be circumvented without resorting to the megaparcel initialization by simply discarding old parcels when the shearing exceeds the grid size. For a few parcels, this time scale is a matter of hours. For others, however, this time scale can be weeks. Section 3.3 pursues the idea of tracking parcel shearing in greater detail.

Because the vertical motion of the parcel is constrained to a single potential temperature surface, the initial uncertainty in the vertical location of a measurement enters into an isentropic trajectory calculation differently. Each parcel is initialized with a constituent value derived from a vertical interpolation of a discrete set of column measurements to a particular potential temperature surface. Reported errors in measurement of the vertical profile result in uncertainty in the interpolation of this profile. This uncertainty can be taken into account by initializing each parcel with a constituent value of $\rho \pm \Delta\rho$, where $\Delta\rho$ depends on the magnitude of the vertical gradients of the constituent field and the shape of the potential temperature surface. Unlike the error in the horizontal location, the error $\Delta\rho$ is constant with time.

In summary, the three dimensional character of satellite measurements can introduce uncertainties in the trajectory mapping technique. Maps produced using the single parcel representation contain inaccurate positional information, especially in the presence of large wind shears. Some disagreements between new and old measurements in trajectory maps, however, can be attributed to the inability of the satellite to detect fine scale structure in the atmosphere.

Trajectory maps only reflect a possible state of the real atmosphere. One improvement in the technique may be to advect a spatial probability distribution for the location of each measurement and then use these probability distributions as weighting functions in the construction of constituent maps. Such a technique is examined further in Section 3.3.

3.2.3 Diabatic vs Adiabatic Calculations

Another inaccuracy in the trajectory mapping technique results from the adiabatic approximation used most often in trajectory calculations. In regions of ascent or descent, diabatic effects cause changes in the potential temperatures of real air parcels. The vertical motion which results from these diabatic effects leads to two types of inaccuracies in the isentropic calculations: those caused by vertical constituent gradients and those caused by vertical wind shears.

After a period of time governed by the rate of heating, vertical constituent gradients result in inaccurate isentropic trajectory maps. Isentropic trajectory maps cannot account for the movement of parcels onto the potential temperature surface of study which occurs in the real atmosphere. Instead, these maps contain only those measurements made on the potential temperature surface of study. In regions of large vertical constituent gradients, the parcels which migrate to the potential temperature surface of study will have constituent values quite different from those measured on that surface at an earlier time. The older measurements in such a trajectory map are, therefore, unrepresentative of the correct synoptic distribution.

Even without large vertical constituent gradients, errors in trajectory maps can accumulate due to the adiabatic approximation. As the parcels move off their initial potential temperature surface, they encounter somewhat different winds, both in magnitude and direction. When this difference becomes substantial, the horizontal trajectories separate. The time scale for this separation is somewhat longer than that for the shearing discussed in the last section (since they must first vertically separate to the point that the encountered wind fields are substantially different). Isentropic calculations in regions with substantial diabatic effects, therefore, will contain a significant number of inaccurate, older parcels if such parcels are not otherwise removed.

To quantify the errors caused by this horizontal separation, two characteristics of diabatic and adiabatic trajectory maps were examined as a function of time: the displacement of individual trajectories from their initial positions and the spatial distribution of a representative trace gas. Both studies utilized a nearly uniform initial distribution of 2057 parcels between 20^0 North latitude and the pole. NMC balanced winds for the month of January 1992 drove the trajectories. Isentropic trajectories were run on the 800 K potential temperature surface (30 km), while diabatic calculations were initialized at 800 K, isentropically advected, then vertically corrected once

each time step according to heating rates calculated by a radiative transfer model [39]. Figure 3.7 displays the results of the two aforementioned comparisons between the diabatic and adiabatic maps.

In the Figure, the starred points represent the correlation between the individual parcel displacements (for the two different computational schemes) as a function of time. This correlation remains above 0.9 for ten days, and is still greater than 0.5 after thirty days. Such results indicate that the adiabatic approximation is quite good for at least 10 days.

The triangular points in the Figure represent the correlation between the resultant, trace gas distributions. To compute the spatial distributions, the Northern hemisphere was divided into 95 equal area bins. Each parcel was assigned its initial NMC PV value as a proxy variable for trace gas concentration. Trajectory maps, from which the average trace gas density in each bin could be computed, were produced every 24 hours. In order that the total material in both the diabatic and adiabatic maps be the same, bins in the diabatic case were integrated vertically. The vertically integrated diabatic bins were then compared with the two-dimensional adiabatic bins. The results demonstrate that even after 30 days, very high correlation exists between the two density fields. In other words, the large scale features found in trajectory maps appear quite robust.

From the statistical analysis of both the displacements and spatial distributions presented above, it appears that the isentropic approximation used in most trajectory calculations is valid for individual trajectories over periods of about 10 days, even during the winter season. Information related to the large scale features of the distribution appears to be preserved for even longer periods of time, though the constituent field may be locally changing due to vertical motions not captured in the isentropic calculations.

3.2.4 Wind Field Errors

Finally, but most importantly, errors in the wind field can have significant impacts on trajectory calculations. As mentioned earlier, slight displacement of chaotic regions in the wind field can lead to dramatic changes in trajectory calculations. To examine the potential effects on resultant trajectory maps caused by wind field errors, a study examining the differences between trajectory maps produced with NMC balanced winds and those produced with assimilated winds from NASA/Goddard Space Flight

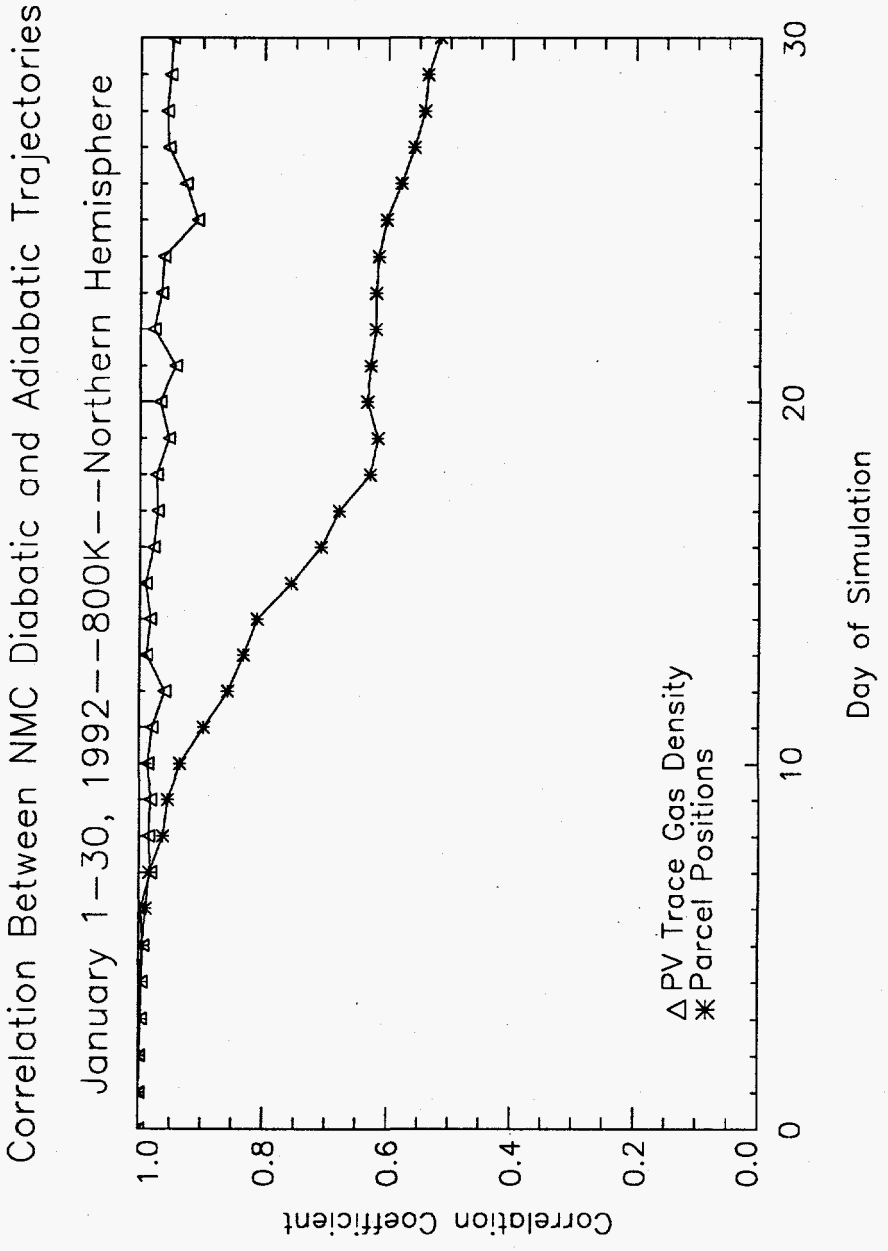

Figure 3.7 Differences Between Isentropic and Diabatic Trajectories

Center's Data Assimilation Office (GSFC, see Appendix D.3) was conducted. The study was performed for the period January 1-28, 1992. Again, a distribution of 2057 parcels nearly uniform in density was initialized in the Northern hemisphere on the 800 K potential temperature surface (30 km) between 20^0 North latitude and the pole. Isentropic trajectory calculations were performed and the resulting maps analyzed with the same two methods described above. Figure 3.8 shows the results of this analysis.

Again, the starred points represent the correlations between individual parcel displacements, while the triangles represent the correlations between the spatial distributions as a function of time. As before, the spatial distributions remain highly correlated for the entire period of study (still near 0.9 after 28 days). The correlation between the displacements, however, drops off much more rapidly. After just 3 days, the correlation between parcel positions has dropped to below 0.9. And after 10 days, it has reached its minimum value of 0.2.

The fact that this correlation gets no lower than 0.2 is a result of geometry, dynamics, and tracer conservation. Parcels within the vortex tend to stay within the vortex, and are hence confined to remain within a certain distance of one another. Parcels outside the vortex remain outside the vortex and are also confined, this time by the Earth's geometry, to remain within a certain distance of each other. Outside the vortex, however, the maximum allowed separation is greater than that inside the vortex. As a result, a minimal degree of correlation between individual trajectories is maintained over long periods of time.

From this wind field study, it appears that trajectory maps of constituent fields remain valid for long periods of time, while the paths of individual trajectories may become highly uncertain after relatively short periods of time. The results of the next section provide a further understanding of the nature of these trajectory errors.

3.3 Modified Trajectory Mapping

In an attempt to account for the uncertainty in parcel position alluded to earlier, a modified trajectory mapping technique has been developed. The modified technique initializes megaparcel clusters consisting of five sub-parcels for each measurement rather than a single parcel. The spacing of the sub-parcels in each cluster is set to approximately reflect the scale of the satellite measurements. Tests shown here were conducted with the spacing set to two different values: 11 and 44 km.

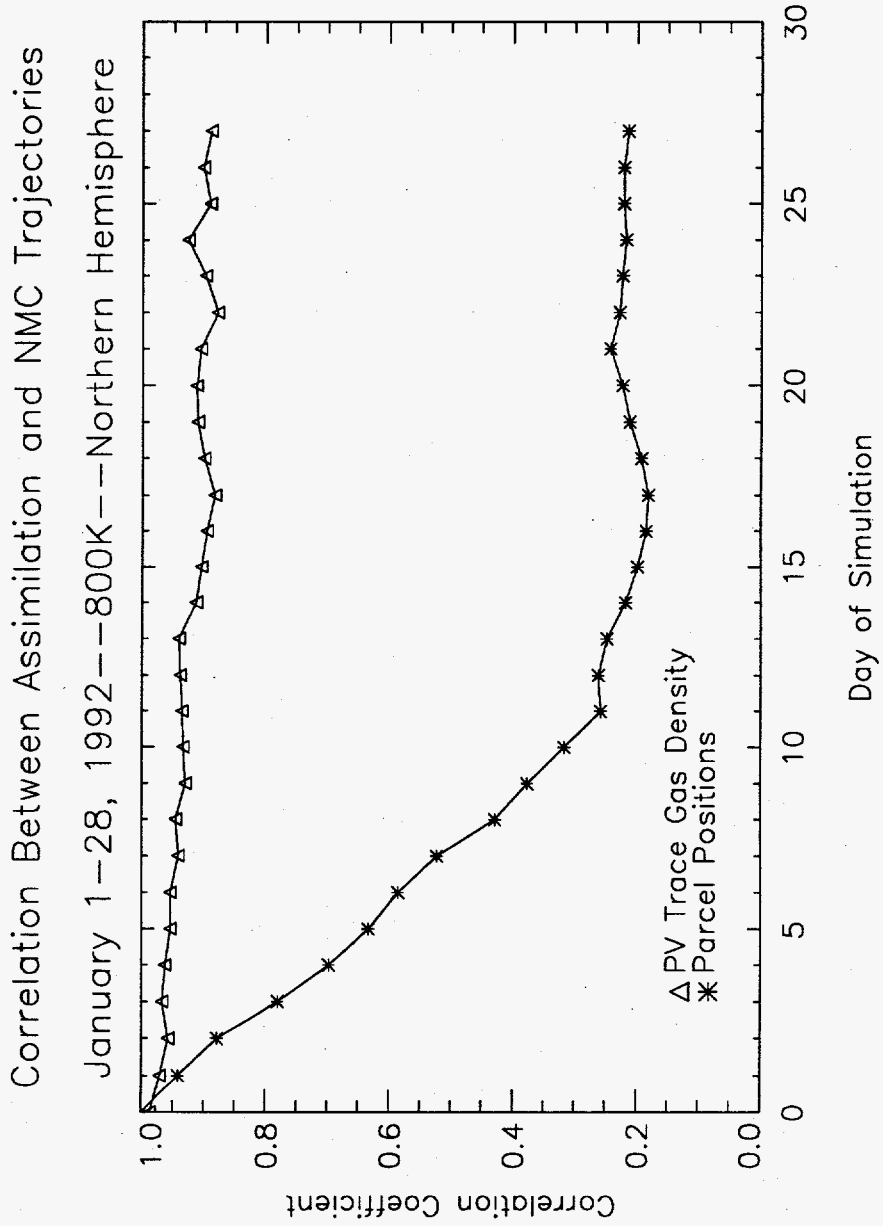

Figure 3.8 Differences Between Trajectories Using GSFC and NMC Wind Fields

In addition to this alternate initialization scheme, the modified trajectory mapping technique attempts to better account for parcel shearing. To simulate atmospheric shearing, the model examines the maximum separation of cluster members after 3 days. If the separation of any of the sub-parcels from its central parcel exceeds 500 km (or the approximate grid spacing), each of the sub-parcels in the cluster is reinitialized as a cluster itself in a process called "spawning." The spawning technique thereby allows measurements to spread in space more like real atmospheric parcels. The spawning time, initial separation, and shearing parameters are all adjustable.

This technique also straightforwardly allows the parcels to mix through the procedure used to create maps. Individual measurements shear apart with time. To produce maps from a collection of sheared measurements, parcels are statistically weighted. The weight of each measurement's sub-parcels is inversely proportional to the total number of sub-parcels representing the measurement. For example, for a measurement which has not spawned and was initialized in a cluster of five sub-parcels, each of the five sub-parcels is given a weight of $1/5^{th}$ of the measurement. Should the measurement have spawned once, 25 sub-parcels would represent the measurement with each carrying a weight of $1/25^{th}$ of the measurement. To determine gridded map values, a statistically weighted average of all the parcels within each grid box is computed.

To determine if the modified technique improved resultant maps and if so, on what scale the improvement might be detected, the following test was conducted. CLAES N_2O data from the period September 3–9, 1992, the period of the noted tropical wave-breaking event in the Southern hemisphere [34], were used in the tests.

N_2O measurements made between the 3^{rd} and 9^{th} of September were isentropically advected to form a synoptic map at 0:00Z on September 9^{th}. Comparisons were made between the most recently added data (gathered between 12:00Z September 8^{th} and 0:00Z September 9^{th}) and the trajectory map composed of the older measurements, as produced by both the standard and modified trajectory mapping techniques. Agreement was determined by examining a normalized root mean square deviation of the new measurements from the trajectory map values. The root mean square deviations were computed from

$$RMS = \frac{\sqrt{\sum_{i=1}^{n}(1 - y_i/x_i)^2}}{n} \tag{3.13}$$

where the x_i represent the n new measurements (made within the 12 hour period prior to the time of the synoptic map) and the y_i represent the corresponding local mean of the older measurements (those advected more than 12 hours).

For the modified trajectory scheme, the mean value was computed using the statistical weighting scheme outlined above. "Nearby" advected measurements were taken to be those measurements whose advected locations at the time of comparison were within a given great circle distance of the new measurements. For this study, the critical distance was allowed to vary from 100 km to 1000 km so that the relative strengths of the two trajectory mapping techniques as a function of scale could be assessed.

Particularly on the smaller scales, some new measurements do not have any old, advected measurements nearby for comparison. Such new measurements have been excluded from the computation of the RMS statistic. Figure 3.9, however, shows the fraction of new measurements which have advected material nearby for three different versions of the trajectory mapping scheme: the standard version, a modified (spawning) technique with an initial separation of 11 km between the central parcel and its associated sub-parcels, and a modified (spawning) technique with an initial separation of 44 km. This Figure indicates the differences in coverage provided by the two techniques. As expected, the modified trajectory mapping technique allows more correlations to be determined, but only noticeably so at the smallest scales. The result is due to the filling of previously unoccupied space with the sheared off pieces of older measurements which the spawning technique incorporates.

Figure 3.10 shows the RMS error as a function of the critical distance for the same three schemes over the entire latitude range in which data was gathered. The Figure demonstrates some improvement for scales smaller than about 400 km when using the modified technique, with the 44 km modified technique producing the minimum RMS error of the three at the smallest critical distances.

Also of interest is the latitudinal dependence of these errors. Data from Figure 3.10 were separated into three latitude bands: equatorial, mid-latitude, and polar. The latter two of these were examined in detail.

The mid-latitude band in the winter hemisphere tends to contain a significant amount of small scale structure. As expected, therefore, Figure 3.11 shows that the modified technique produces the greatest improvement on the smallest scales in the mid-latitudes.

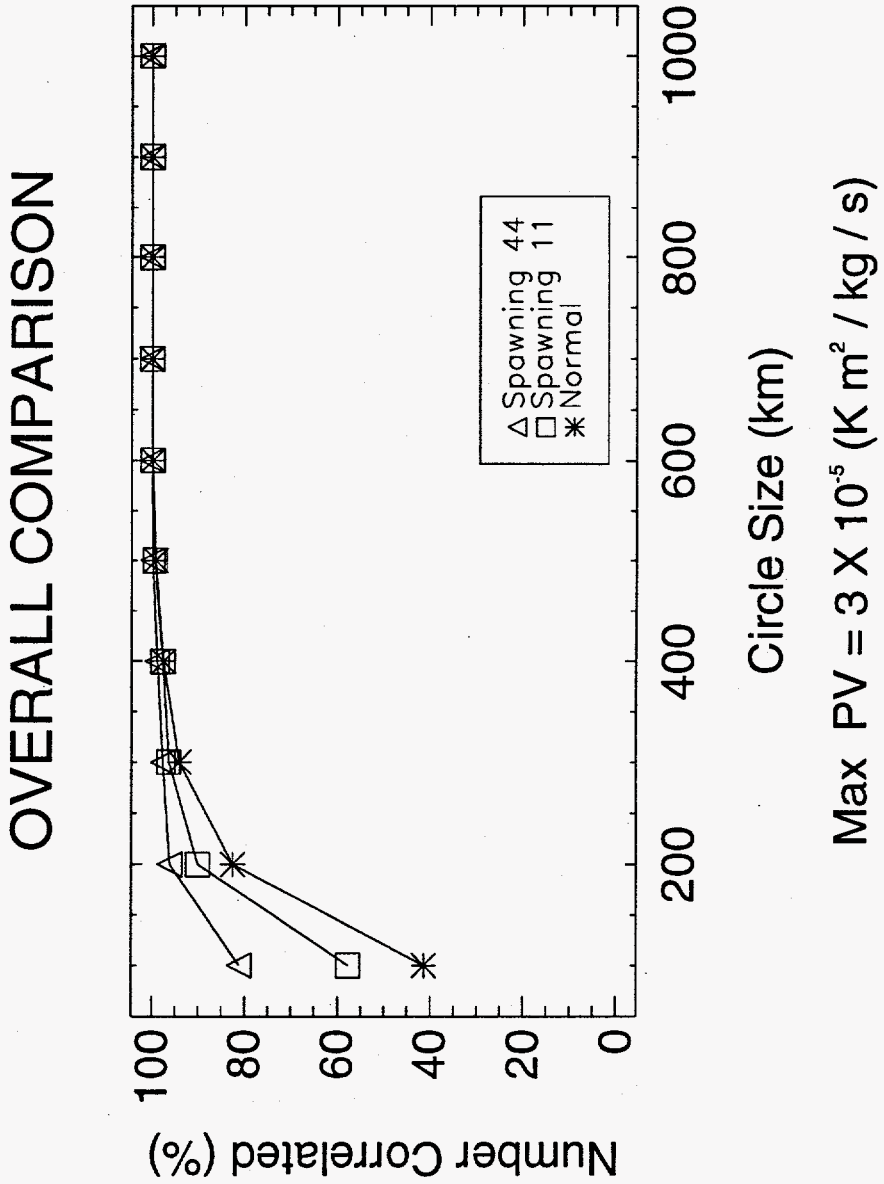

Figure 3.9 Map Coverage for Standard and Modified Trajectory Mapping

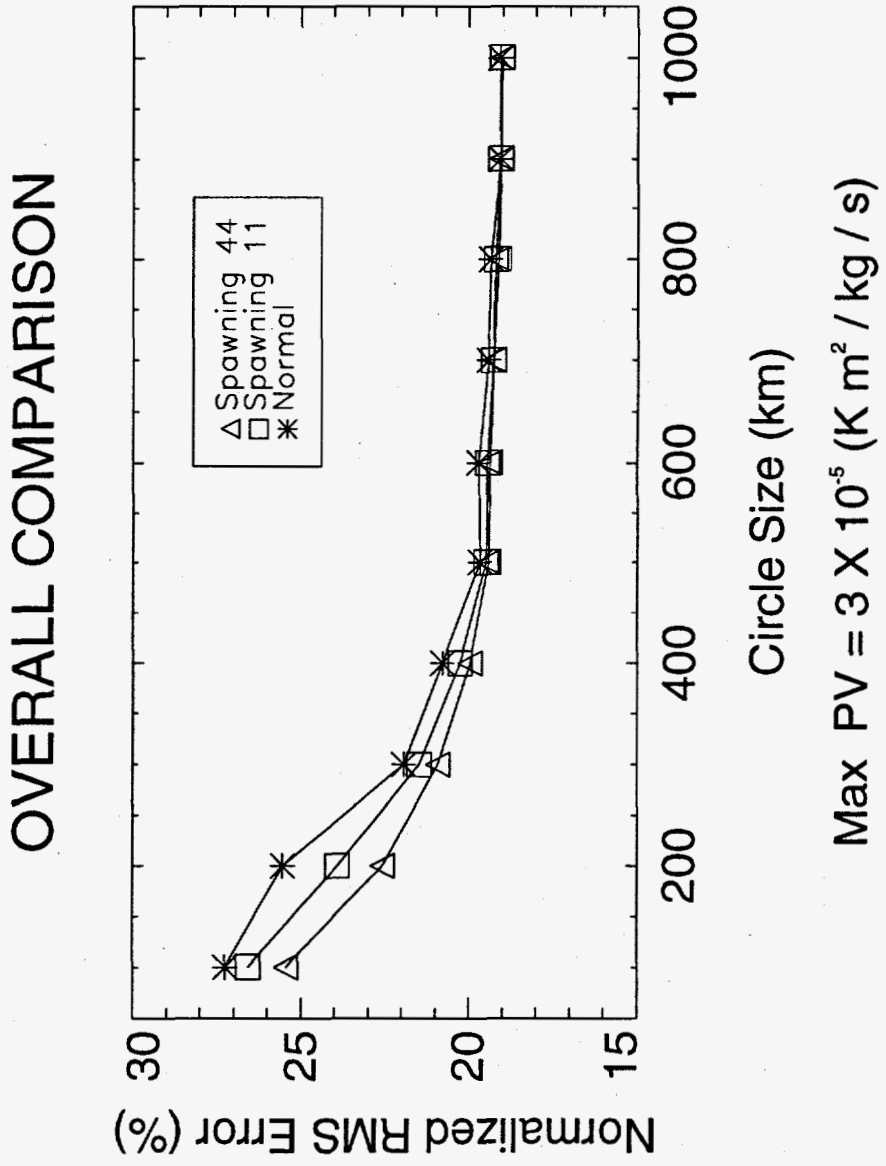

Figure 3.10 RMS Error for Standard and Modified Trajectory Mapping

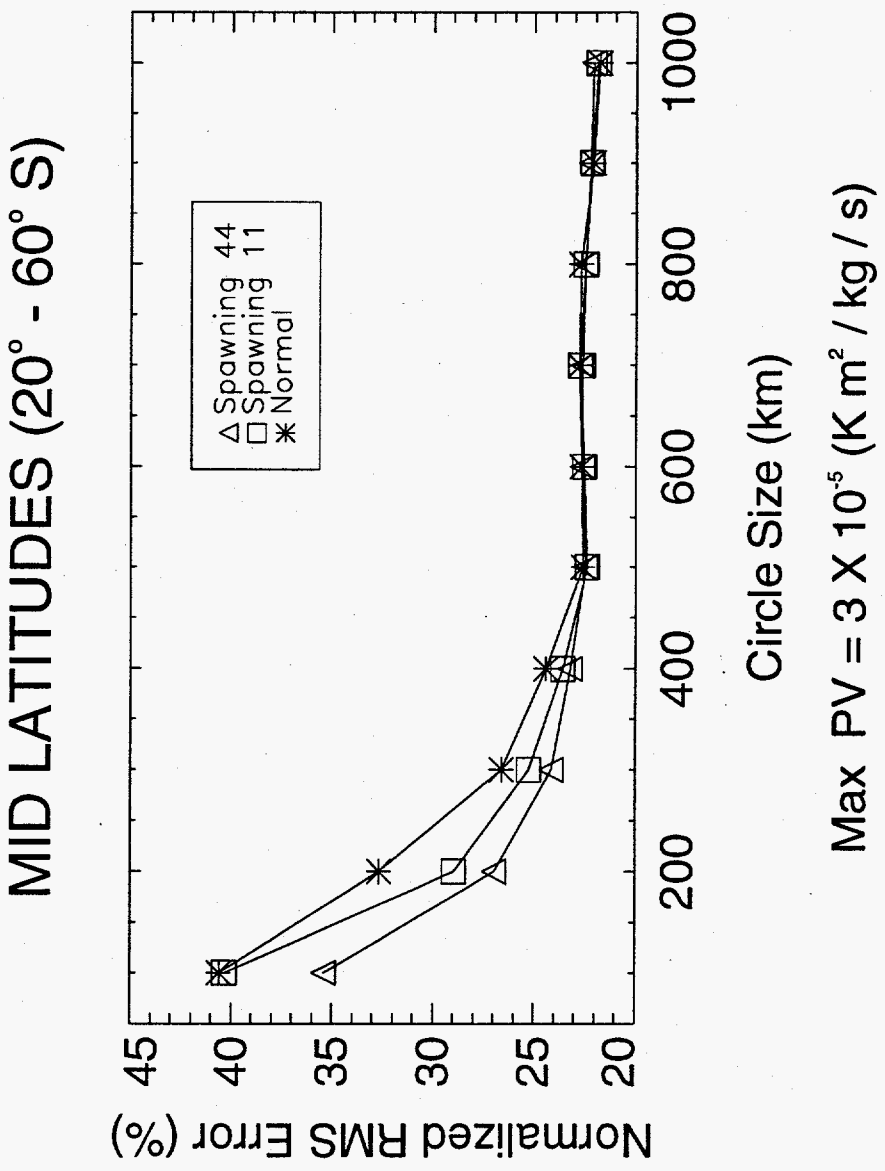

Figure 3.11 RMS Error at Mid-Latitudes

The behavior at higher latitudes is quite different from that at mid-latitudes. Figure 3.12 shows the relationship between RMS error and scale size is quite flat in polar winter regions. The relationship implies that gradients are gentle and constituents fairly well mixed inside the vortex.

These tests indicate an improvement in the agreement between new measurements and predicted map values can be achieved through use of the modified technique. This improvement, however, appears to be limited to scales less than about 400 km and is obtained at an increased computational cost. Therefore, use of the modified technique should probably be limited to cases in which understanding the small scale structure is important.

A second use for the technique can be found in examining sparsely gathered data sets: for example, HALOE data. By using the modified technique, the coverage provided by the trajectory map increases substantially. In fact, *Pierce* [30] first employed multiple parcel initialization for the HALOE data to create trajectory maps. His technique involved initializing a tight cluster of a very large number of parcels for each measurement. He then allowed these clusters to shear apart, spreading to fill in the constituent map quite satisfactorily after several days. Unlike the modified trajectory mapping technique introduced in this Section, however, each measurement in *Pierce's* scheme is represented by the same number of parcels at all times. Thus, the computational cost is comparatively higher than that for the modified trajectory mapping technique, which carries only as many parcels as the shearing dictates.

One final issue can be addressed by examining the results of the modified trajectory mapping study: the nature of the shearing errors. The way in which parcels are sheared apart can be seen quite clearly in Figure 3.13. Here, CLAES N_2O measurements from September 3^{rd} have been advected using the modified trajectory scheme to noon on September 9^{th}. Particularly near the vortex edge, where wind speeds attain their maximum values, most parcels are observed to shear in the direction parallel to the winds and perpendicular to the gradient in the winds. This tendency is indicated by the elongated blobs of uniform color around the vortex edge. Each elongated blob represents the distribution of sub-parcels from a single measurement. Not coincidentally, the direction of shearing also closely parallels the contours of potential vorticity. Furthermore, in tropical regions and inside the vortex, the shearing magnitude is considerably smaller (as indicated by the relatively compact color blobs).

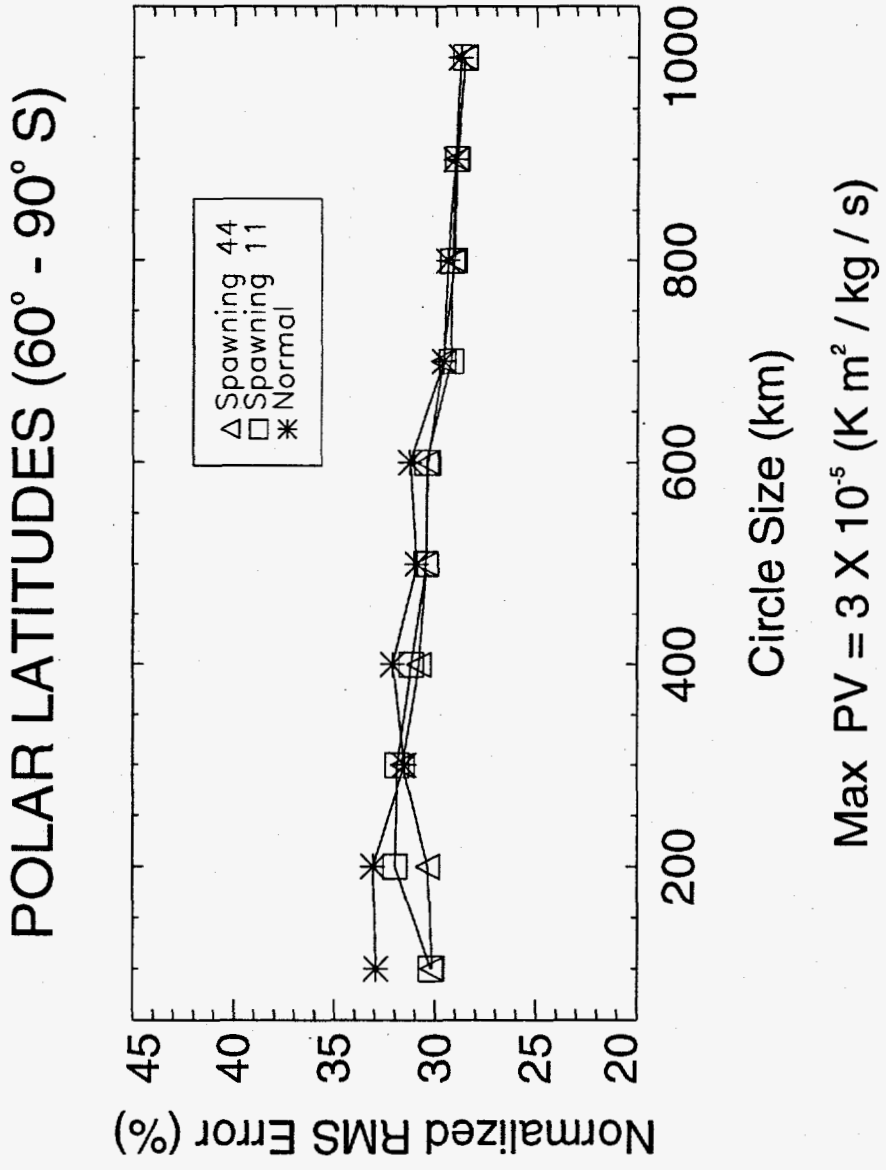

Figure 3.12 RMS Error in Polar Regions

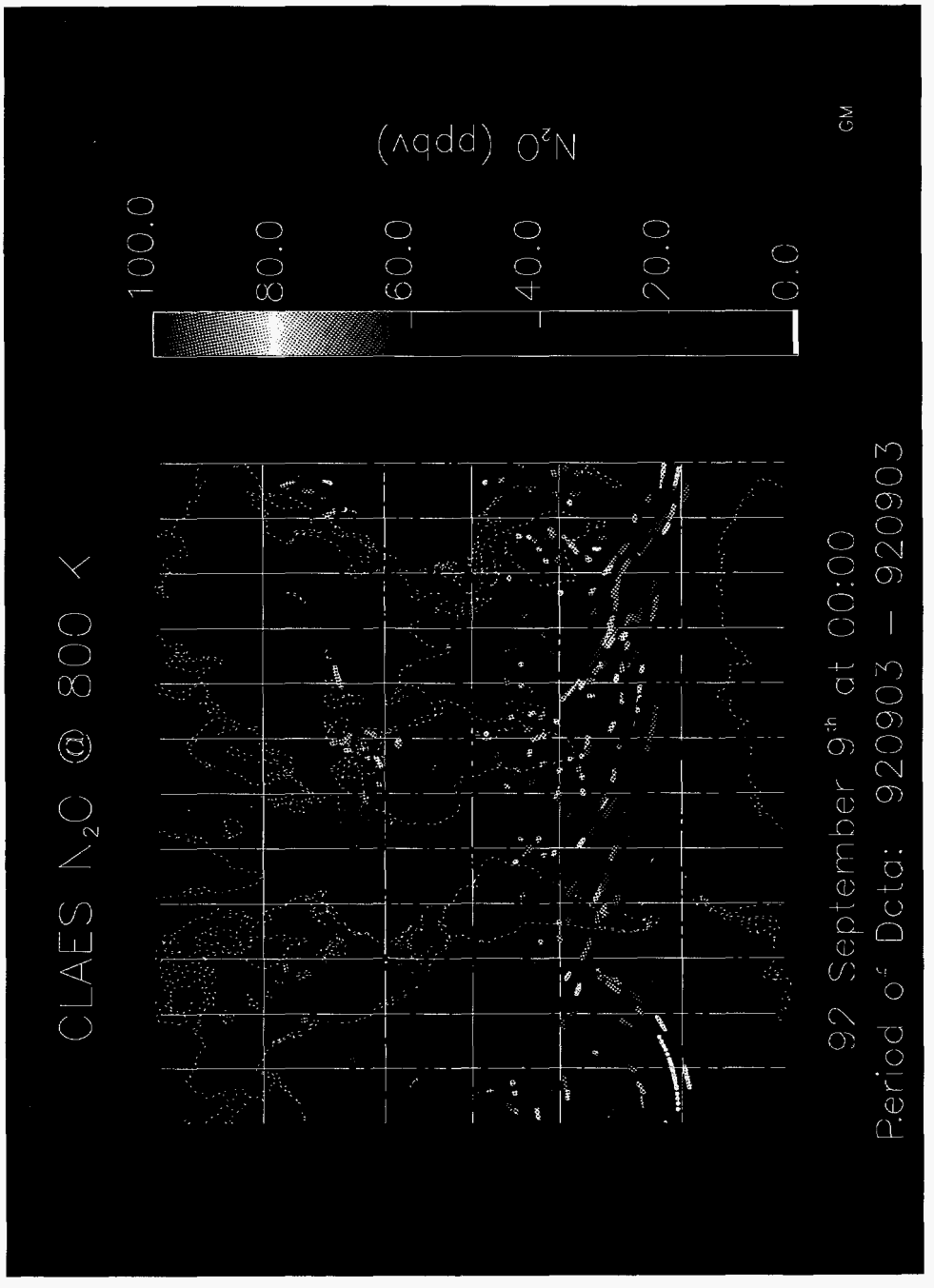

Figure 3.13 Modified Trajectory Map

Such findings explain the success of the point parcel technique in the following manner. Although the point parcel model is an unrealistic representation of atmospheric parcel motion and susceptible to initialization and advection errors, the modified trajectory mapping study indicates that these errors accumulate along the PV contours. Since trace gas values are closely correlated with PV, these errors are not likely to be noticeable in the resultant maps. In other words, the old measurements, though not properly advected, have been advected in such a way that despite errors, they remain in neighborhoods of measurements with similar values. Furthermore, the results validate one of the key assumptions in constituent reconstruction: that [PV, θ] tubes are well mixed. The modified trajectory map shown in Figure 3.13 clearly shows that most of the mixing indeed does occur along these tubes.

In summary, the modified trajectory technique produces marginally better results when examining fine scale atmospheric features and in mapping sparse data sets. The technique, however, does successfully demonstrate atmospheric shearing and explain the success of the point parcel approach.

Chapter 4

Applications

The trajectory mapping technique proves itself quite useful in a number of applications. Below are presented case studies of atmospheric dynamical events, instrument measurement validation, and meteorological field evaluation.

4.1 Atmospheric Dynamical Analysis

To illustrate the capabilities of trajectory mapping, long lived tracer data gathered by two instruments aboard UARS were examined. In the first example, N_2O measurements from the Cryogenic Limb Array Etalon Spectrometer (CLAES) are asynoptically, Salby-Fourier, and trajectory mapped on September 9, 1992. The occurrence of a large scale wave-breaking event [34] provides sharp mid-latitude constituent gradients. The presence of these gradients aids comparisons of the various maps.

Figure 4.1a shows an asynoptic map of CLAES data, interpolated to the 800 K isentropic surface (30 km), on Sept 9, 1992. During the period around September 9, UARS was in "forward flight" mode, so CLAES viewed the atmosphere from 30^0N to 80^0S. Figures 4.1b, c, and d depict synoptic maps at 12:00Z on September 9^{th} of the CLAES data gathered between September 6^{th} and 13^{th} on the 800 K (30 km) surface. The map of Plate 1b was produced with the Salby-Fourier method (shown courtesy of Lee Elson), while the trajectory mapping technique produced the map of Figure 4.1c. Figure 4.1d shows a gridded version of Figure 4.1c to be compared with Figure 4.1b. Also available for comparison is the Kalman filtered map (see Figure 2.2) of the exact same data used to create the Salby-Fourier and trajectory maps.

To produce the trajectory map of Figure 4.1c, data from midnight on September 6 through noon on September 9 were advected forward in time, while data gathered from midnight on September 13 back to noon on September 9 were advected backward in time. Balanced winds derived from NMC temperatures and geopotential heights [33, 26] were used to isentropically advect the measurements. Note that due to in-

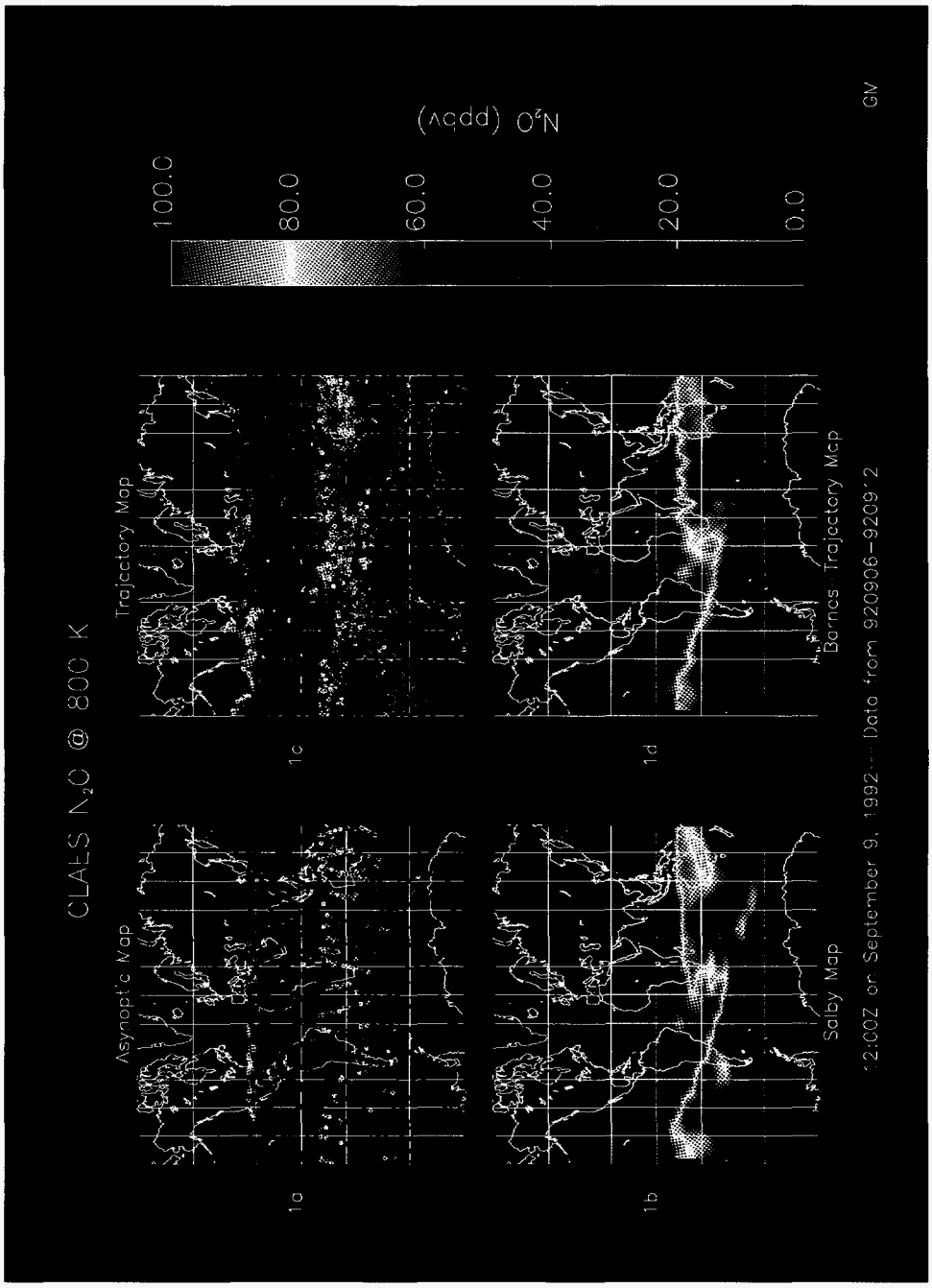

Figure 4.1 Examples of Asynoptic, Salby, and Trajectory Maps

accuracies in the balanced wind approximation near the equator, parcel trajectories equatorward of 20^0 are suspect.

In the trajectory maps, the larger dots represent parcels which have been advected by the trajectory model for periods less than 12 hours (i.e. the larger dots represent the measurements of September 9^{th}). The smaller dots represent parcels added more than 12 hours from the time of the synoptic map (12:00Z on September 9, 1992). The good agreement between older and more recent N_2O measurements demonstrates how well the trajectory model preserves the large scale distribution of nitrous oxide.

Figure 4.1 also demonstrates the advantage of using more than one day of data in map production. While a single day of UARS data provides global coverage, the density of of the coverage improves dramatically when several days data are combined with the trajectory technique (compare Figures 4.1a and c).

The gridded trajectory map (Figure 4.1d), produced with a Barnes averaging scheme, displays a more uniform mid-latitude constituent distribution than does the Salby-Fourier map (Figure 4.1b) or Kalman filtered map (Figure 2.2), both of which contain evidence of Fourier ringing (the high and low N_2O patches). In addition, the trajectory map shows smoother gradients inside the vortex and at the vortex boundary. (In part, this result is an artifact of the scheme used to produce the gridded product from the trajectory data. The Barnes scheme computes a weighted average of parcel values within 1000 km of each grid point. The weighting factor was inversely related to the distance of each parcel from the grid point location. Such a scheme naturally smooths out small scale structures.)

All the gridded products, however, contain somewhat less information than the map of Figure 4.1c. By depicting each measurement, the map of Figure 4.1c allows a visual estimate of the statistical robustness and variance that neither the map of Figure 4.1b nor d allows. Kalman filtering, however, does provide a direct estimate of the errors (see Figure 2.3).

The Salby-Fourier map (Figure 4.1b) and trajectory map (Figure 4.1c) demonstrate a high level of consistency with the satellite data. Studies comparing measurements from September 7–9 to the corresponding synoptic maps for these three days indicate correlation coefficients greater than 0.9.

Unlike the Fourier technique, trajectory mapping can be performed without consideration for data aliasing or periods of missing trace gas data. In addition, the trajectory mapping technique frequently requires far less data than the seven days used in Figure 4.1. Seven days of data were used in the creation of this trajectory

map only so that its product could be directly compared with the Kalman filtered and Salby-Fourier maps. The trajectory mapping technique can produce maps of comparable quality to those Kalman filtered and Salby-Fourier maps using far less data.

The trajectory mapping technique, like Kalman filtering and the Salby-Fourier technique, increases the density of measurements available for use in map production. The higher resolution thus provided allows for the detection of smaller scale features which might otherwise have been overlooked. Figure 3.3 shows a trajectory map generated for November 6, 1992. During this period, the Antarctic vortex is no longer pole centered. It also appears to have shed material to mid-latitudes. Low N_2O filaments can still be seen peeling off of the vortex in this Figure. The low N_2O values (dark blue points) present among the higher values (green points) probably had their origins at or near the vortex edge.

To confirm this hypothesis, a contour advection computation (as described by *Schoeberl and Sparling* [47]) was used to track the vortex edge (here defined by the -2.6×10^{-4} $Km^2/kg/sec$ NMC PV contour) forward in time for eight days from October 28^{th}. When advected to the time of trajectory map and overlaid on the map (as in Figure 3.3), the PV contour seems to explain much of the low N_2O found outside the vortex (again, the white cross-hatched region represents vortex air). In particular, the filament wrapping around the Southern hemisphere at about 35^0S latitude from 0^0 to 90^0W longitude corresponds with two low, recently made, extra-vortex CLAES N_2O measurements. A rough estimate of the likelihood of CLAES detecting a filament is given in the following calculation.

A single day of CLAES measurements provides fairly uniform coverage of one hemisphere, with an average separation between measurements of 400 km in the North/South direction and 12^0 of longitude in the East/West direction. A rough estimate for the expected number of times per day the satellite might make measurements in a filament with width w (km) and length ℓ (degrees longitude) is given by:

$$n = \left(\frac{w}{400}\right)\left(\frac{\ell}{12^o}\right) \tag{4.1}$$

For the case of the filament in Figure 3.3, w is on the order of 40 km while ℓ is around 120^0 longitude, giving $n = 1$. The Figure shows two, newly taken, low valued (blue) measurements very near the filament, so the calculation is of the right order of magnitude.

Also noteworthy in Figure 3.3 is the agreement between the N_2O gradient and the gradient in NMC PV values (red contours). Such agreement is evidenced in nearly all maps produced by the trajectory mapping technique.

As another demonstration of trajectory mapping, Figure 3.4 maps the evolution of the September tropical wave breaking event [33, 23] over the four days from September 8–11, 1992. The larger points in these maps represent data which has been added in the twenty-four hour period prior to the time of the synoptic map. The yellow line represents the edge of the vortex as defined by the -3.0×10^{-4} $Km^2/kg/sec$ NMC PV contour. As in the previous N_2O study, the gradient in N_2O across the vortex boundary and the good agreement between new and old parcel values is well maintained.

Furthermore, to demonstrate the technique's ability to perform despite data gaps, data from the 10^{th} of September were not used in the production of the Figure. As can be seen, the trajectory mapping technique was still able to produce a synoptic map on this day (see Figure 3.4). The use of advected, older data to produce a map on September 10^{th} completed the otherwise incomplete picture of the evolution of the event. An analysis such as that provided in Figure 3.4 demonstrates one of the most powerful applications of the trajectory mapping technique—the reconstruction of the history of atmospheric events, even through periods of missing data. Such long data drop-outs can present severe obstacles for the Salby-Fourier and Kalman filtering techniques.

As a final example, Figure 4.2 shows the large scale intrusion of tropical air to mid and high Northern latitudes in February 1993, also reported by *Randel et al.* [34] and further examined by *Manney et al.* [23]. The H_2O data shown here comes from MLS and was gathered during the period February 18–23, 1993. Forward in time, isentropic trajectory maps were generated on successive days from February 20^{th} to 23^{rd}. Like N_2O, the lifetime of H_2O at these altitudes has been shown to be sufficiently long for H_2O to be considered a valid dynamical tracer in these maps [4].

A couple of features in the Figure are worth noting. First, good agreement between constituent and NMC PV gradients is again evident in the MLS H_2O Figure. Second, the good correspondence of new measurements (larger dots) to older, advected measurements (smaller dots) lends confidence to the technique.

The cases examined above allow the following three conclusions to be made: 1) the advected measurements agree well with new measurements (affirming the technique);

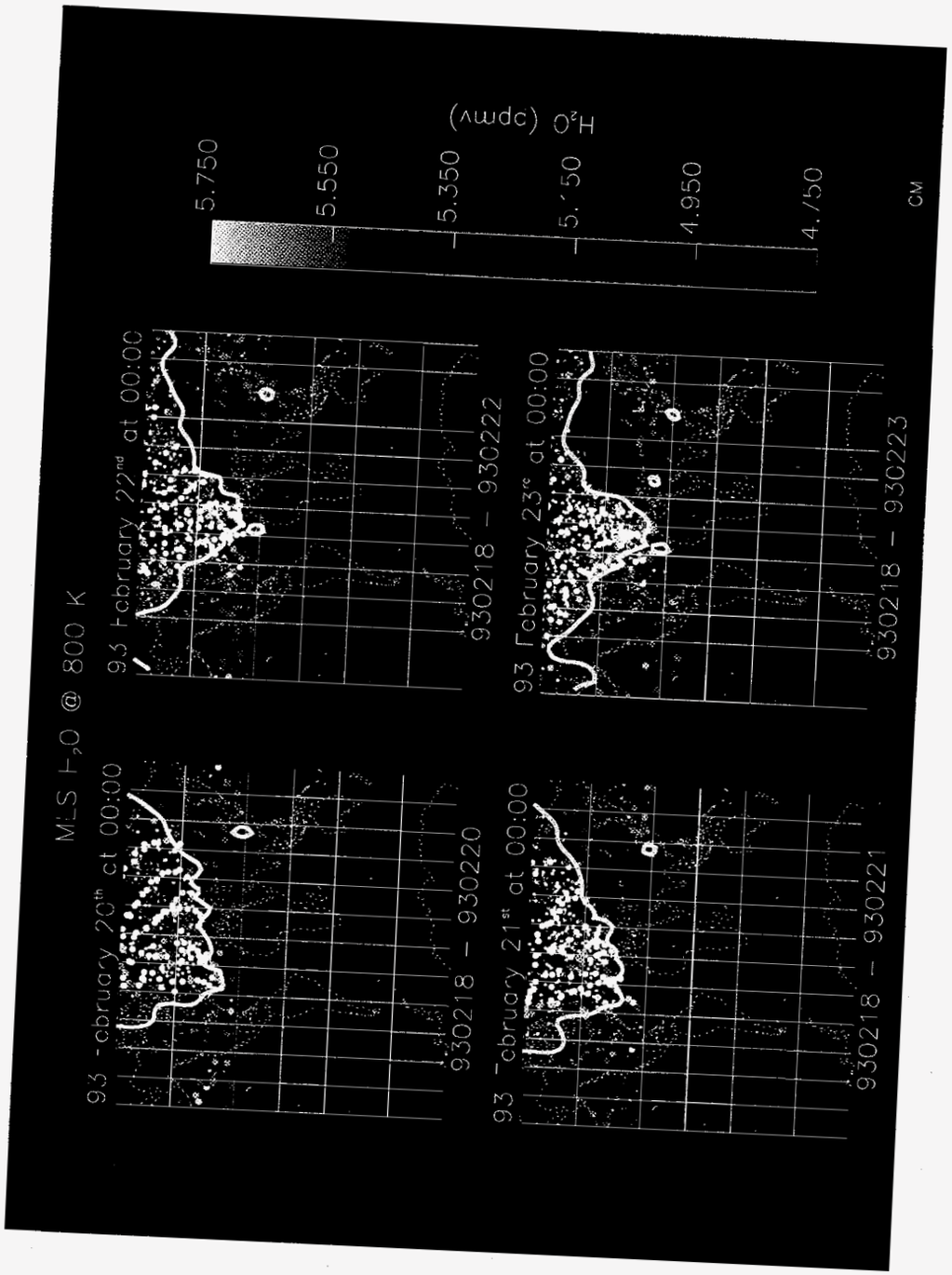

Figure 4.2 February 1993 Wave Breaking Event Seen in MLS H_2O Data

2) the satellite measurements are self-consistent; and 3) the satellite is capable of detecting large scale wave-breaking events and small scale vortex filamentation.

4.2 Data Validation Studies

The trajectory mapping technique proves quite useful in satellite data validation studies. Post-launch validation studies have been, in the past, very difficult to perform. Trajectory mapping provides a simple method with which to carry out such studies. Two types of validation studies can be performed using the technique: analysis of instrument accuracy (by comparing two different instruments' measurements of the same quantity) and precision (by evaluating the self-consistency of data from a single instrument). The methods for estimating each of these quantities are presented below, along with demonstrations using satellite and aircraft data sets.

4.2.1 Accuracy Studies

Due to the inherent difficulty in acquiring measurements from two sources at the same place and time, determining the accuracy of a satellite instrument after launch can be problematic. Trajectory mapping provides a simple method to facilitate this type of data validation.

After outlining a procedure for data validation studies using trajectory mapping techniques, three example studies are presented. The first study examines the agreement between two different UARS instruments measuring the same quantity. The second study assesses the agreement between satellite and in situ measurements. Finally, the third study compares measurements from instruments aboard two different satellites.

Procedure

To perform comparisons between two different data sets, the method creates a series of synoptic trajectory maps using data from one of the two instruments. Ideally, a synoptic trajectory map would be created with data from instrument 1 at each time instrument 2 makes a measurement. The value recorded by instrument 2 can then be compared with the nearby, advected measurements from instrument 1. Due to the high frequency at which the satellites and aircrafts make measurements, however, the creation of synoptic maps at each measurement time is somewhat impractical.

Instead of creating synoptic maps at every measurement time, therefore, synoptic maps are created from both data sets once every 12 hours (at midnight and noon). The first appearance of each measurement from instrument 2 in the series of instrument 2 trajectory maps is then compared with neighboring measurements in the corresponding instrument 1 trajectory map. As shown in Section 3.2, the advection of parcels over periods of less than 12 hours should not lead to substantial errors. The accuracy of the comparisons, therefore, should not be significantly reduced.

If the instrument 1 trajectory maps are constructed solely from forward trajectories, they will be biased toward data added early in the period of interest. The bias owes to two factors: data added in the early part of the study period will be present in more maps, hence included in more averages; and maps early in the series will have fewer data points, resulting in higher weight being given each data point that does exist. To eliminate such biases, trajectory maps of instrument 1 data are created from a combination of forward (in time) and backward (in time) trajectories. Furthermore, with no less accuracy, potentially twice as many points can now be included in the trajectory maps for comparison purposes.

MLS vs HALOE Water Vapor

As a demonstration of the applicability of the trajectory mapping technique to satellite data validation studies, water vapor measurements from MLS (version 3) and HALOE (version 16) were compared. Because MLS and HALOE measurements are not collocated in space or time, the comparison problem is ideally suited for the trajectory mapping technique.

MLS H_2O is available for the Southern hemisphere from August 14 through September 21, 1992 and from October 30 through November 28, 1992. Version 3 MLS H_2O is only reliable down to about 46 mb (22 km) in the stratosphere. Southern hemisphere HALOE measurements are made throughout both of these periods.

Three separate one week long periods were selected for this study: August 14–20, September 14–21, and November 1–7, 1992. Comparisons were made for each period on three different potential temperature surfaces: 650 (26 km), 800 (30 km), and 1200 K (38 km).

The data sets were compared using the technique outlined above (see Procedure) with MLS acting as instrument 1 and HALOE as instrument 2, and with the following additional restrictions. First, MLS trajectory maps were constructed only from data

taken within +/- 1.5 days of the synoptic map time. In this way, errors arising from the trajectory calculations (see Section 3.2) are minimized. Second, to make the comparison with HALOE measurements, MLS data within a 400 km radius circle were averaged. To prevent the influence of large dynamically induced gradients on these averages, Ertel's potential vorticities (calculated from NMC meteorological fields and interpolated to each parcel location) were examined. Those MLS parcels with PV values too dissimilar from the PV value associated with the corresponding HALOE measurement were excluded from the averaging calculations. Table 4.1 shows the tolerances used in this study. Third, only those circles containing more than 3 advected MLS measurements were included in the study.

HALOE's data retrieval pattern restricted the latitude range over which the comparisons were made. For the August period, HALOE measured trace gasses between 40^0 and 60^0 S latitude. During the September period, HALOE retrieved data between 34^0 and 54^0 S, And during the November period, it gathered data between 25^0 and 47^0 S. The August and November HALOE measurements were taken at sunset while the September HALOE measurements were taken at sunrise.

The results of the comparisons are shown in Figures 4.3– 4.5. The Figures indicate reasonable agreement between the measurements. MLS appears routinely higher than HALOE by between 0.5 and 1.5 ppmv, with the higher discrepancies and lower correlation coefficients appearing at higher altitudes. Such results are in good agreement with other validation studies [11].

UARS versus ASHOE Aircraft Ozone Data

A wide variety of atmospheric constituents are measured by both UARS (see Appendix A) and the instruments aboard the ER-2 (see Appendix C). Previous comparisons of these data sets, however, have relied on one of two techniques: satellite overpasses

Potential Temperature (K)	Δ PV $\times 10^{-5} \frac{K \cdot m^2}{kg \cdot s}$		
	Aug	Sept	Nov
650	2	2	2
800	4	5	4
1200	20	20	20

Table 4.1 Restrictions on the Comparison of MLS and HALOE H_2O

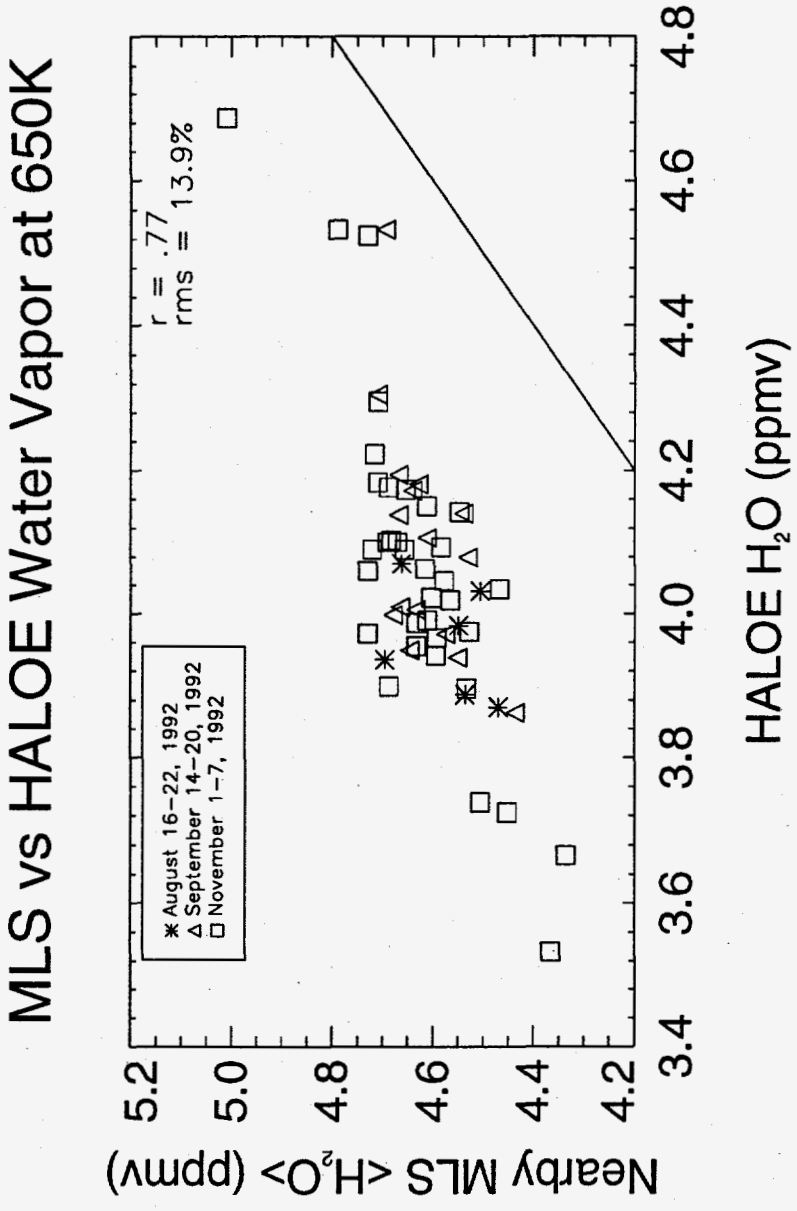

Figure 4.3 MLS vs HALOE Water Vapor at 650 K

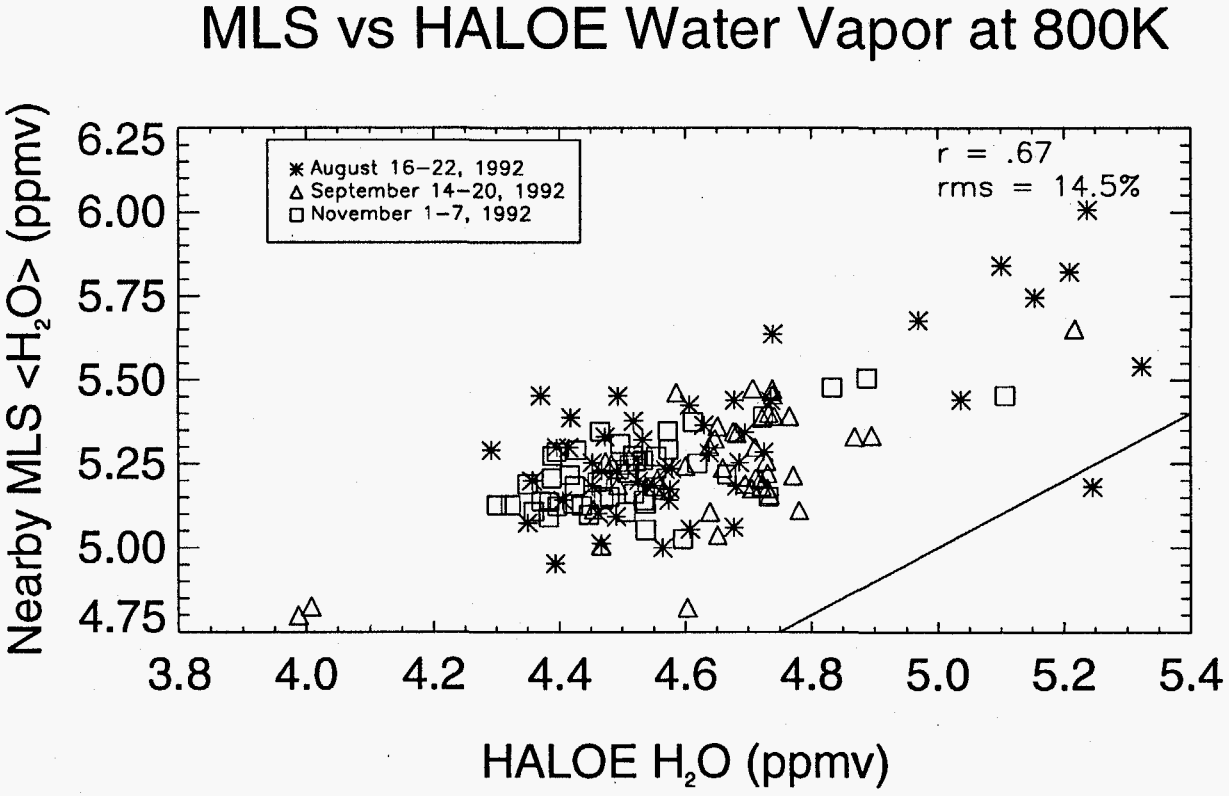

Figure 4.4 MLS vs HALOE Water Vapor at 800 K

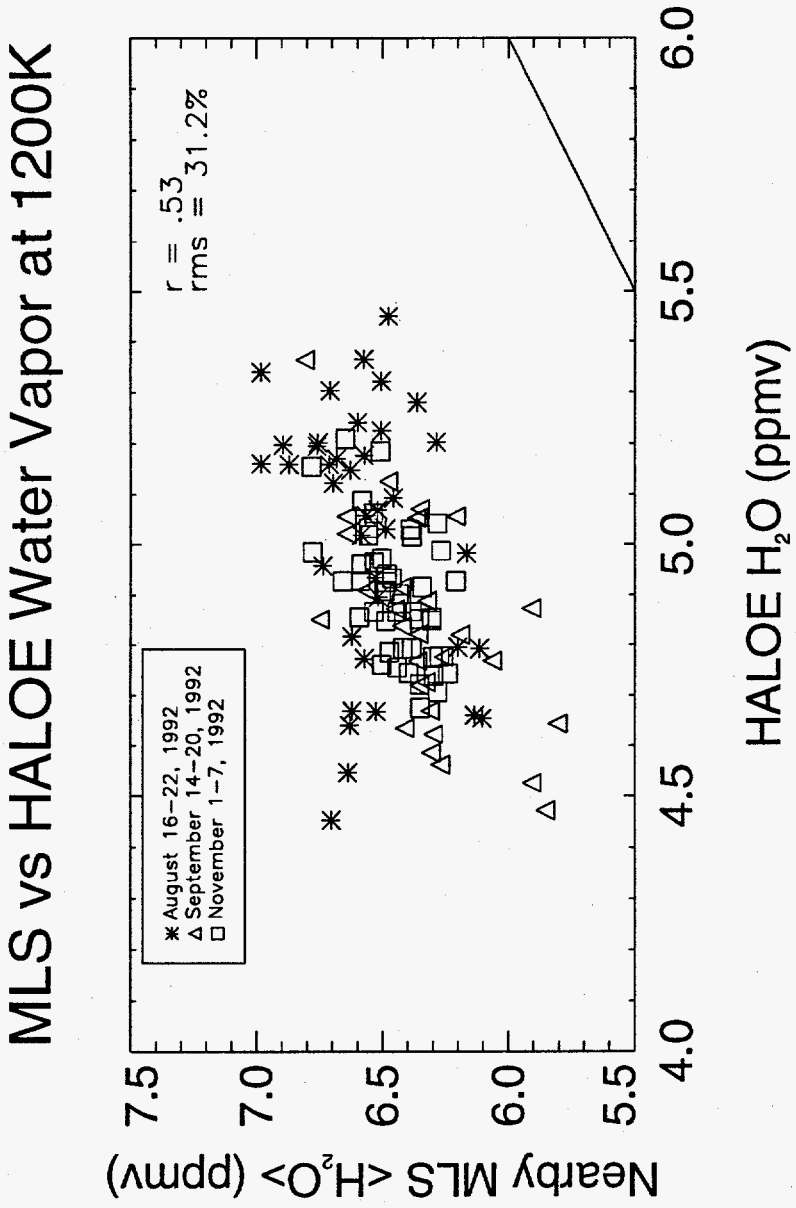

Figure 4.5 MLS vs HALOE Water Vapor at 1200 K

near the flight path [54] or the comparison of zonal means of the satellite data with the aircraft. In this section, trajectory mapping is applied to the problem, allowing a more direct comparison of the two sets of measurements.

The study presented here compares ozone measurements from MLS (205 GHz channel) with those from the ER-2's Dual-Beam UV-Absorption Ozone Photometer [32] made during the Airborne Southern Hemisphere Ozone Experiment (ASHOE). It should be noted that as the ASHOE mission is still underway, the ER-2 ozone data are still preliminary.

To perform the comparisons, trajectory maps were created from MLS ozone data gathered in a 10 day period centered on the flight date. (While the lifetime of an ozone molecule is on the order of hours at these altitudes [4], the lifetime of the odd oxygen which regulates the local mixing ratio of ozone is on the order of months [4]. Therefore, the amount of ozone in a parcel advected for 5 days is unlikely to change significantly.) Flight data were also trajectory mapped, with output being saved 5 times in a 24 hour period. All trajectories were calculated using NMC wind fields.

As in the HALOE/MLS water vapor study, MLS trajectory mapped data were averaged in a 400 km radius circle about the location of the ER–2 measurements. In addition, the modified potential vorticity (MPV, see Appendix E) associated with the ER–2 parcel and the surrounding MLS parcels were compared. Those MLS parcels whose MPV differed by more than 2×10^{-6} K m^2 / kg / sec were excluded from the computed MLS averages. Furthermore, only those ER–2 measurements which had more than three advected MLS measurements nearby were included in the study.

The aircraft data has a much higher spatial and temporal resolution than the satellite data. The ER-2 data sets used in this study report measurements every 10 seconds. With the aircraft traveling about 200 m/s, this temporal resolution results in a spatial resolution of 2 km. In contrast, the satellite data points are separated by about 400 km. Comparing the raw data sets, therefore, would poorly characterize the degree to which they agree or disagree.

A more appropriate comparison can be made by smoothing the aircraft data so that its spatial resolution more closely matches that of the MLS instrument. To do so, the ER–2 data have been averaged over 200 km intervals along isentropic portions of the flight track.

Typical flight plans restrict the aircraft to one potential temperature surface outbound and a different potential temperature surface inbound. Some variability does exist along the flight track. To exclude data too different in potential temperature,

therefore, a tolerance of +/– 5 K from the targeted potential temperature surface has been instituted. The averaging scheme and flight plans outlined above result in 3–15 smoothed data points per flight. A specific list of the flights and potential temperature surfaces included in this study can be found in Table 4.2.

Figure 4.6 shows a comparison of the MLS trajectory mapped averages to the ER-2 measured ozone values for eight ER–2 data sets from 5 flights between the end of March and the middle of April 1994. For the flights on 4/3, 4/5, and 4/13, sufficient data were gathered on two different potential temperature surfaces to include both such surfaces in this study. These days, therefore, are found multiply listed in both Table 4.2 and the legend of Figure 4.6. As can be seen in the Figure, the agreement between the satellite and in situ data is remarkably good, with a correlation coefficient above 0.9 and an RMS error of about 12%.

Figure 4.7 separates the data into individual flights. The Figure shows ozone as a function of latitude for 4 ER-2 flights. Overplotted are the corresponding, trajectory mapped ozone values. Again, the agreement is fairly good. Obviously, however, MLS has a harder time detecting the sharp gradients near the primitive vortex boundary than does the ER–2. This result is due partly to the lower spatial resolution of the MLS measurements and partly to comparison technique itself (the 400 km circles over which the MLS data are averaged restricts the minimum scale of detectable features).

The generally good agreement between the MLS and ER–2 data revealed by this technique, however, demonstrates the relevance of trajectory mapping to future data validation studies of satellite instruments with in situ aircraft measurements.

Label	MLS Data Used (1994)	ER-2 Flight	θ (K)	Δ PV X $10^{-6}\frac{K \cdot m^2}{kg \cdot s}$
940330	3/30, 4/1, 4/3, 4/5	3/30/94	490	2.0
940403a	3/30, 4/1, 4/3	4/3/94	460	1.5
940403b	4/5, 4/7, 4/9		480	1.8
940405a	4/1, 4/3, 4/5	4/5/94	485	1.9
940405b	4/7, 4/9, 4/11		495	2.1
940413a	4/9, 4/11, 4/13	4/13/94	470	1.7
940413b	4/14 – 4/19		500	2.2
940415	4/11, 4/13 – 4/21	4/15/94	490	2.0

Table 4.2 Information for the MLS vs ER-2 Ozone Comparison

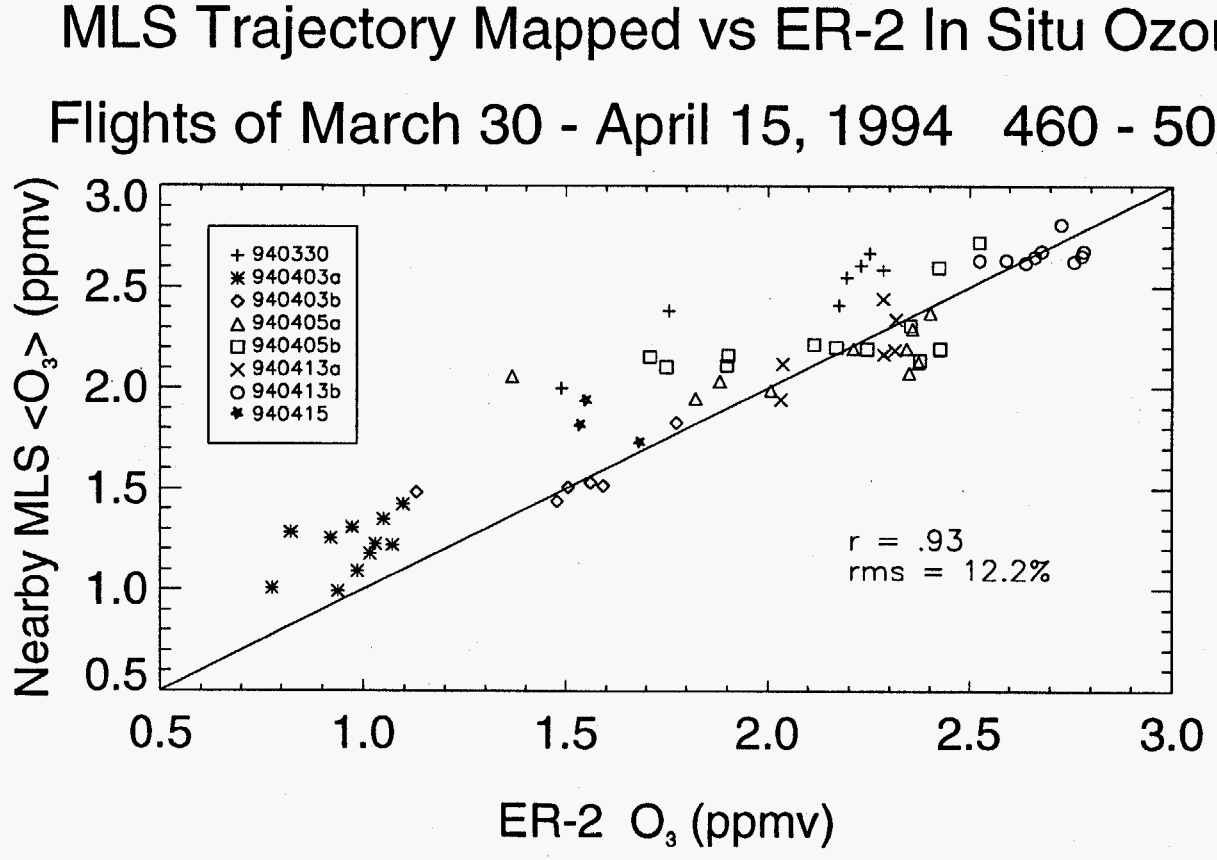

Figure 4.6 MLS vs ER-2 Ozone

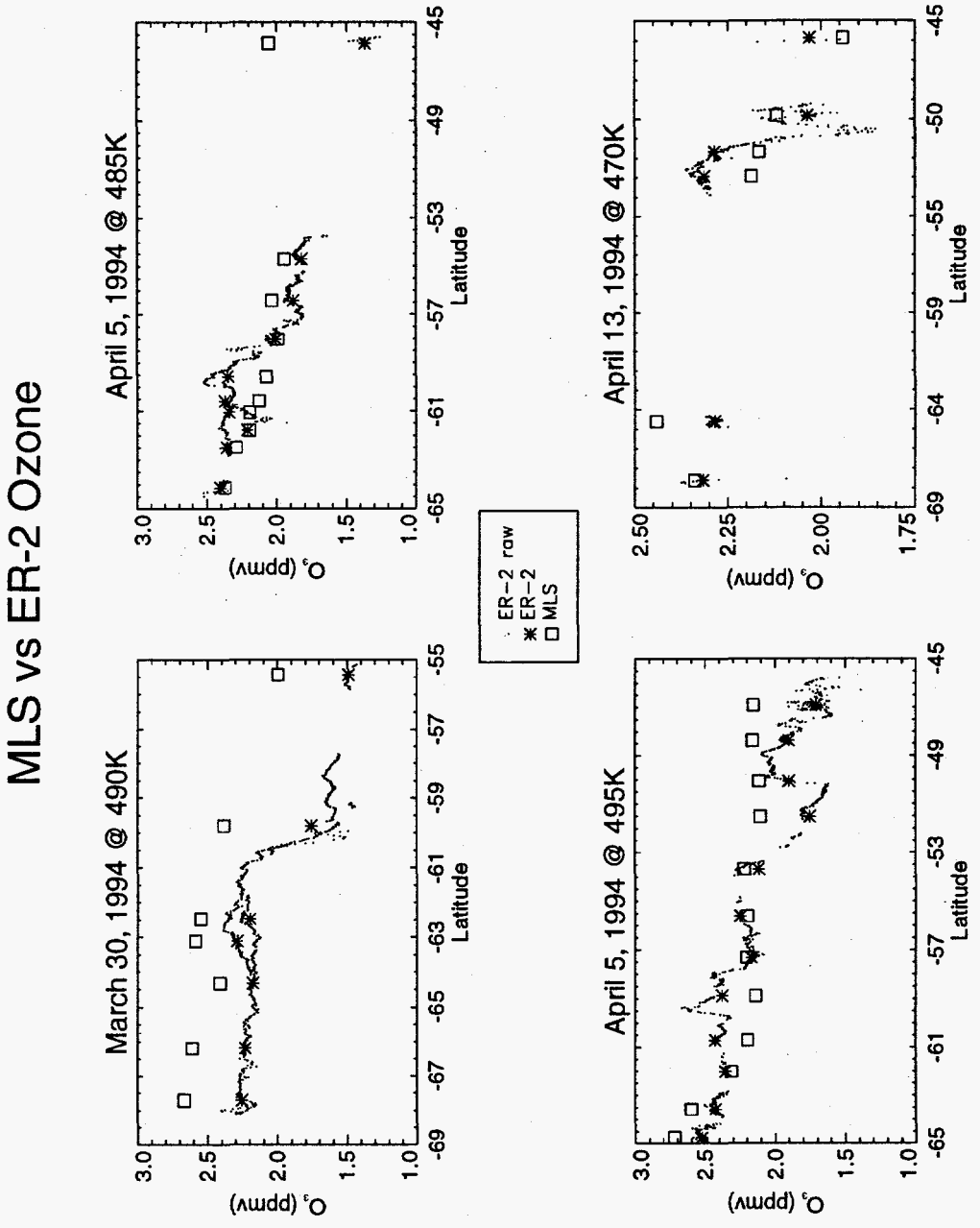

Figure 4.7 MLS vs ER-2 Ozone Along Flight Paths

MLS vs SBUV2 Ozone

As a third and final example of accuracy studies, MLS and the Solar Backscatter Ultra-Violet instrument #2 (SBUV2, see Appendix B) ozone measurements are compared. The basic technique is similar to that outlined above for the other accuracy studies. MLS ozone data on the 800 K potential temperature surface were isentropically trajectory mapped for the period from January 1–14, 1992. Winds from the United Kingdom Meteorological Office (UKMO, see Appendix D.2) were used to advect the measurements. SBUV2 ozone data were isentropically trajectory mapped every 12 hours on the 800 K potential temperature surface from noon January 2^{nd} through noon January 12^{th}.

Figures 4.8 and 4.9 show trajectory maps of the SBUV2 and MLS data at midnight on January 14^{th}. Both maps depict a large filament peeling off the polar vortex and extending through mid-latitudes. In addition, both indicate the presence of tropical air wrapped around the vortex edge. While the MLS ozone measurements appear to be higher than the SBUV2 measurements, the general structure of the fields is quite similar.

For a more rigorous analysis, statistical comparisons were made between the SBUV2 measurements and the average of MLS measurements in nearby neighborhoods. The neighborhood of an SBUV2 measurement was defined by a circle of radius 400 km around the location of the first appearance of an SBUV2 parcel in the SBUV2 trajectory maps. The neighborhood was further restricted by a dynamical constraint on the variation of PV within the circle. No MLS parcels whose PV values differed by more than 5×10^{-5} K m^2 / kg / sec from that of the associated SBUV2 parcel were included in the average. In addition, only MLS measurements made within +/- 1.5 days of the relevant synoptic map time were included.

Figure 4.10 shows a scatter plot of MLS averages versus the SBUV2 measurements. In general, the correlation between the data sets appears quite good, with a calculated correlation coefficient of 0.95 and an RMS error of 13.2%. It appears that at the highest values, MLS consistently records more ozone than SBUV2. When broken down by dynamical regimes, the data reveal interesting behavior.

In the Figure, the triangles represent comparisons made in vortex air (defined as those parcels whose PV value exceeds 3×10^{-4} K m^2 / kg / sec); the plusses represent mid-latitude measurements ($1.25 \times 10^{-4} <$ PV $\leq 3 \times 10^{-4}$ K m^2 / kg / sec); and the circles represent those comparisons made in tropical regions ($|$PV$| \leq 1.25 \times 10^{-4}$

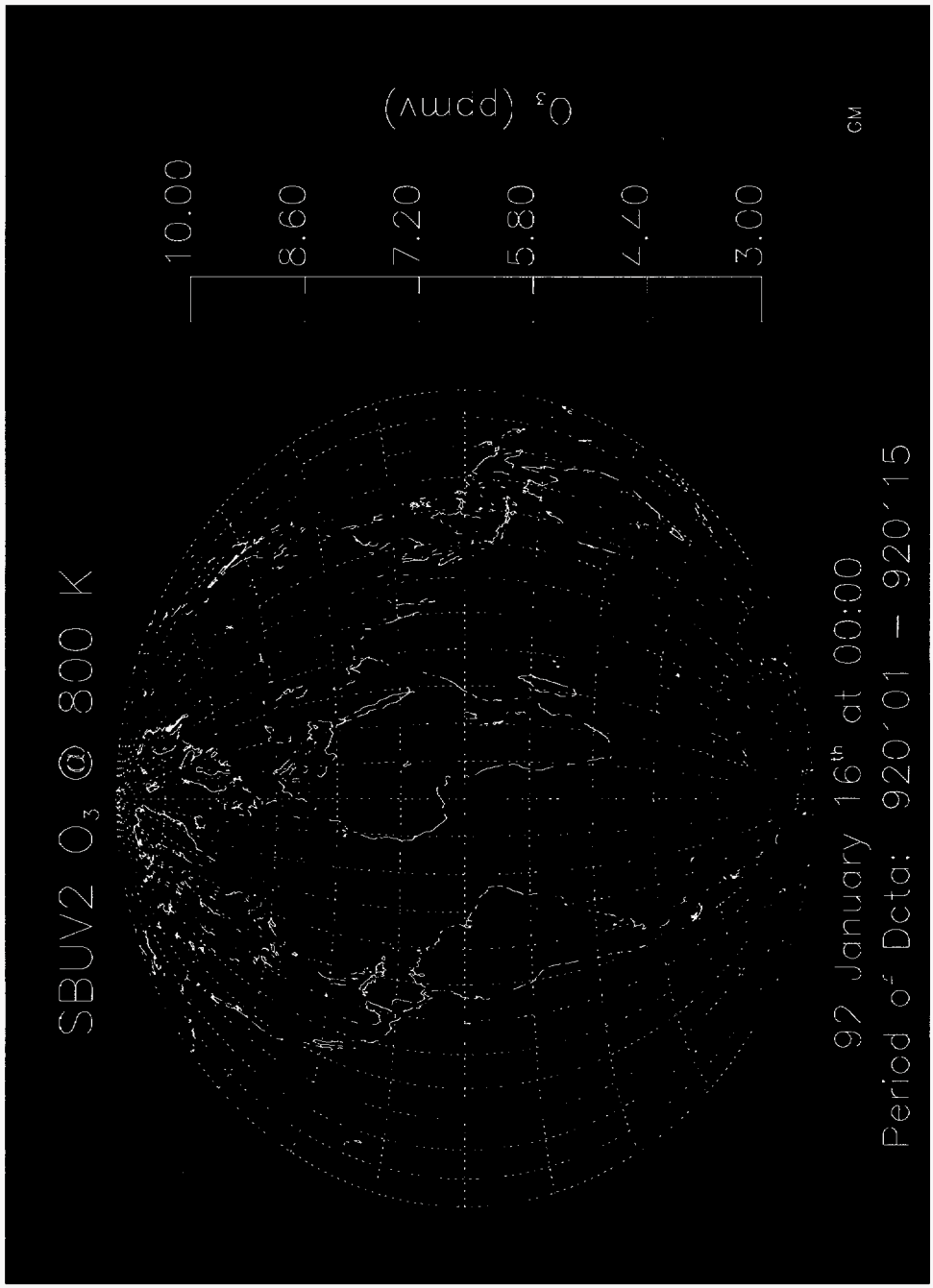

Figure 4.8 Trajectory Map of SBUV2 Ozone

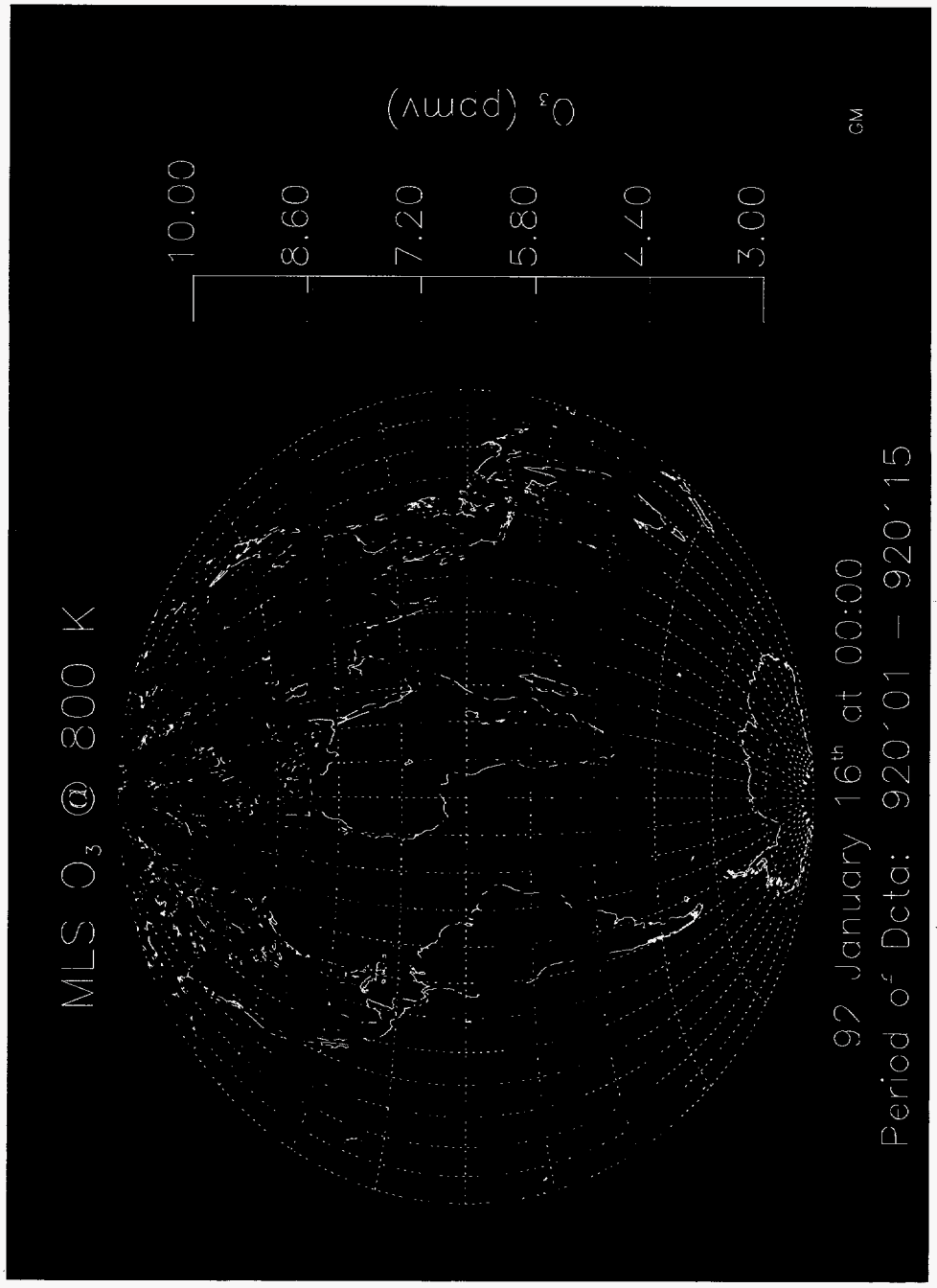

Figure 4.9 Trajectory Map of MLS Ozone

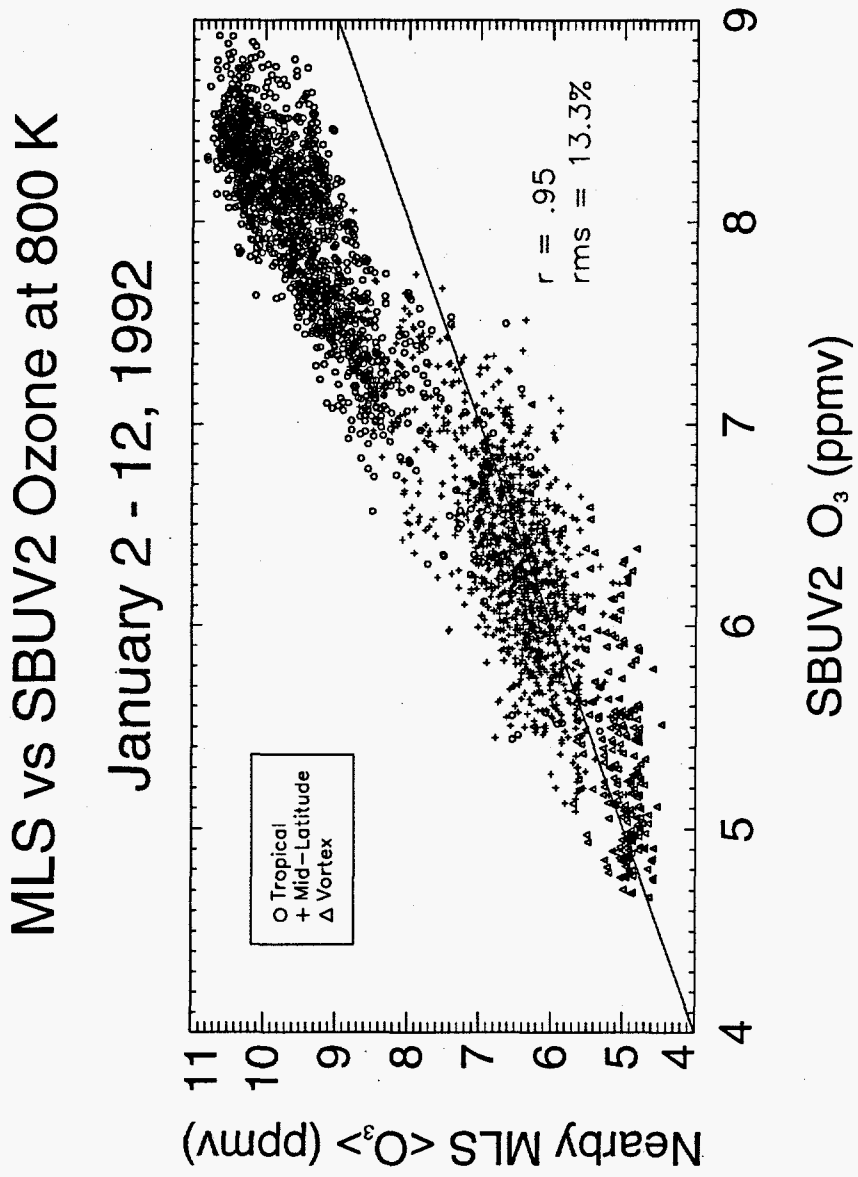

Figure 4.10 MLS vs SBUV2 Ozone

K m^2 / kg / sec). The slopes of lines of best fit to the data from these different regions can be seen to be quite different from one another. The reason for these differences has yet to be determined. The importance of determining the cause of the discrepancy and which of the two measurements is correct is clear. Given that much of the research today involves the determination of ozone trends (for example, *Stolarski, et al.* [50]), knowing the accuracy of instrument measurements amount of instrument drift becomes vital.

The above comparisons of non-collocated and dissimilarly measured data sets have been successfully performed with relative ease, demonstrating the usefulness of trajectory mapping. Future satellite data validation work should be enhanced by trajectory mapping techniques.

4.2.2 Precision Studies

Precision studies are performed in a manner quite similar to the accuracy studies outlined above, with one major exception: a single data set is employed and compared to itself via trajectory techniques. To perform these studies, a series of isentropic trajectory maps is made using a combination of back and forward trajectories of all the data for a selected constituent gathered by an individual instrument over a specified period of time.

In the study presented here, the trajectory maps have been produced every twelve hours (at 0:00Z and 12:00Z). Measurements made within $\pm$ 6 hours of the synoptic map time are called "new" measurements and compared with nearby advected data in the trajectory map. Nearby data consists of measurements made within $\pm$ 1.5 days of the time of the synoptic map (thus minimizing the affect of growing trajectory model errors) and within a 400 km great circle distance of the location of the "new" measurement. The nearby, advected measurements are averaged together and compared with the new values.

MLS Water Vapor Data

For this study, MLS H_2O data from August 14-24, 1992 were examined using the technique outlined above on three isentropic surfaces: 650 (26 km), 800 (30 km), and 1200 K (38 km). Isentropic trajectories were calculated using NMC winds. The lifetime of water vapor at these levels is significantly greater than the length of the studies [4], so chemical changes in its mixing ratio should be small. Because the

comparisons are performed only with data advected less than 1.5 days, vertical motion (which has a time scale on the order of 10 days as shown in Section 3.2.3) and other trajectory errors should be minimal.

The RMS error derived from the trajectory mapping technique has been compared to the mean quality flag parameter (as provided by the MLS science team) for the same set of measurements. The quality flag associated with each measurement represents the science team's best estimate of the error of the measurement. Data with quality flags reported as less than zero indicate climatological values and have, therefore, been excluded from the study. Also excluded from the study were those measurements whose correlation circles contained fewer than four advected measurements.

Figure 4.11 shows the calculated correlation coefficient as a function of time on each isentropic surface in the study. While the correlations remain quite high on the 800 (30 km) and 1200 K (38 km) surfaces, the correlations at 650 K (26 km) are seen to wildly fluctuate. More careful analysis of individual 12 hour periods reveals the reason. Figure 4.12 shows a scatter plot of the trajectory mapped H_2O averages versus the recent H_2O measurements for two distinct 12 hour periods: one with relatively a high correlation coefficient (from the pm measurements on August 14^{th}) and one with a low correlation coefficient (from the am measurements on August 16^{th}). The cause of the disparity is obvious from this Figure. On August 14^{th}, MLS observes a wider range of measurement values, while on the 16^{th}, the values observed fall only at the lower end of the overall range. The clustering at the low values (between 4 and 5 ppmv) is similar for both days. The lack of high values on the 16^{th}, however, necessarily results in the lower correlation coefficient. This particular example demonstrates the danger of examining only the correlation coefficient. The root mean square (RMS) error, therefore, has been used to better gauge the robustness of the result.

Figure 4.13 shows that the precision of the data as estimated by the RMS error (see Equation 3.13). The RMS error at each of the three vertical levels remains less than about 5% of the measurement for then entire period of study, while the average quality flag parameter is about 7% of the measurement at the highest altitudes and grows to near 20% of the measurement at the lower levels. The increase in the value of the quality flag parameter with depth into the atmosphere reflects the reduced confidence of the MLS team in the accuracy of their results at the lower altitudes. The trajectory RMS results, however, indicate that the precision of the MLS H_2O data remains consistently high over the entire range of altitudes considered.

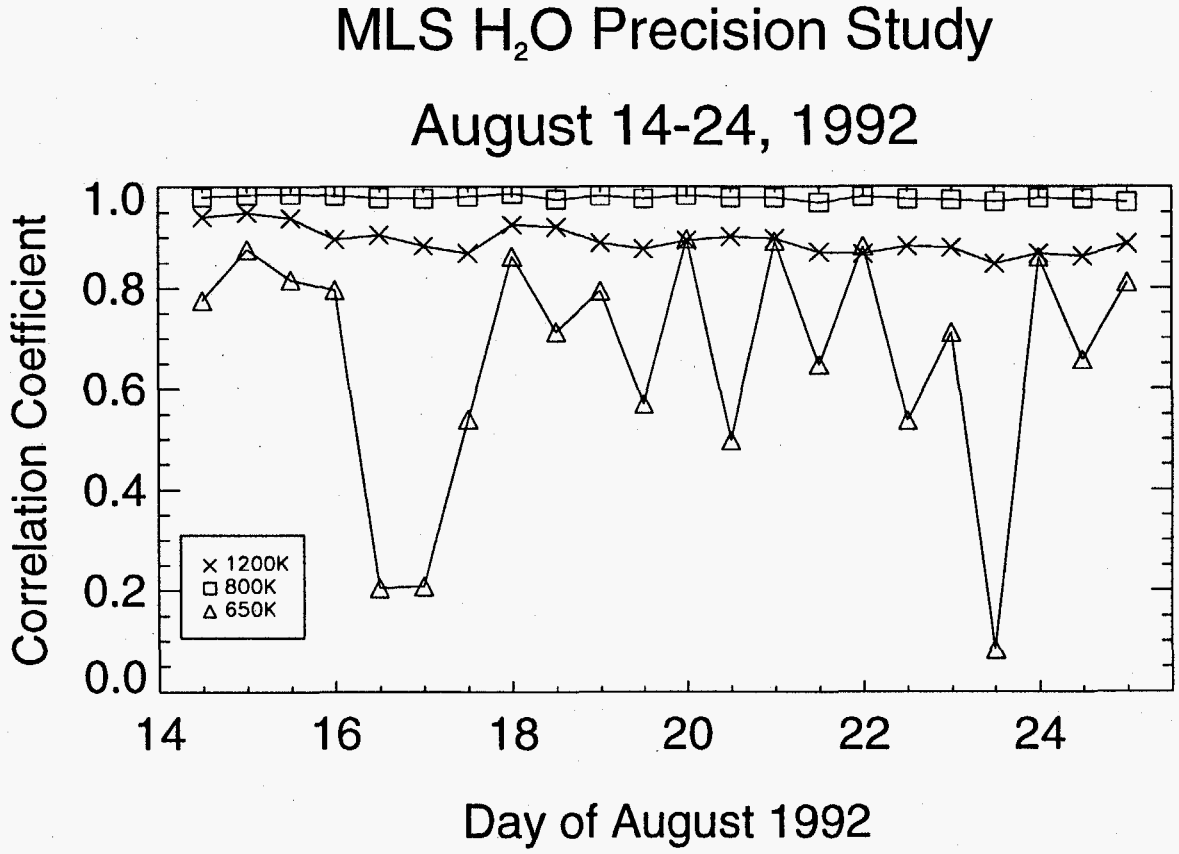

Figure 4.11 Self-Consistency of MLS Water Vapor Data

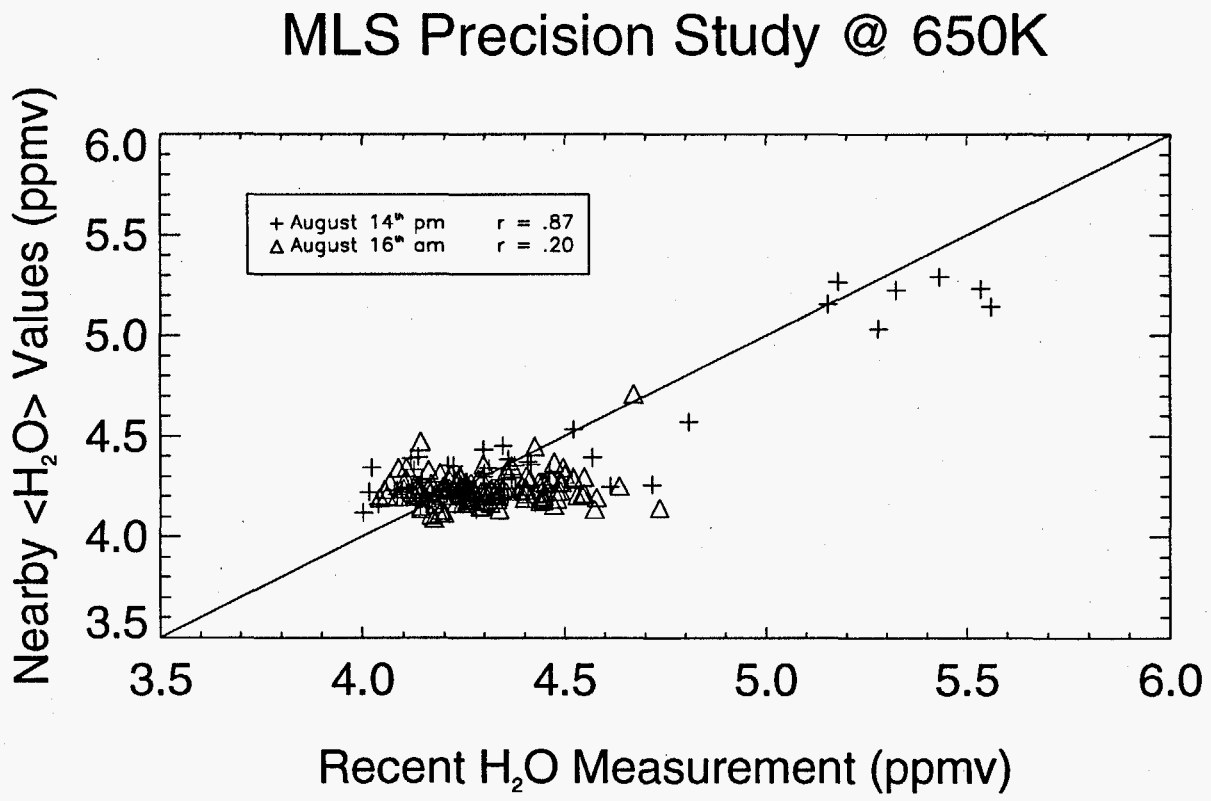

Figure 4.12 Scatter Plot of MLS Water Vapor Data

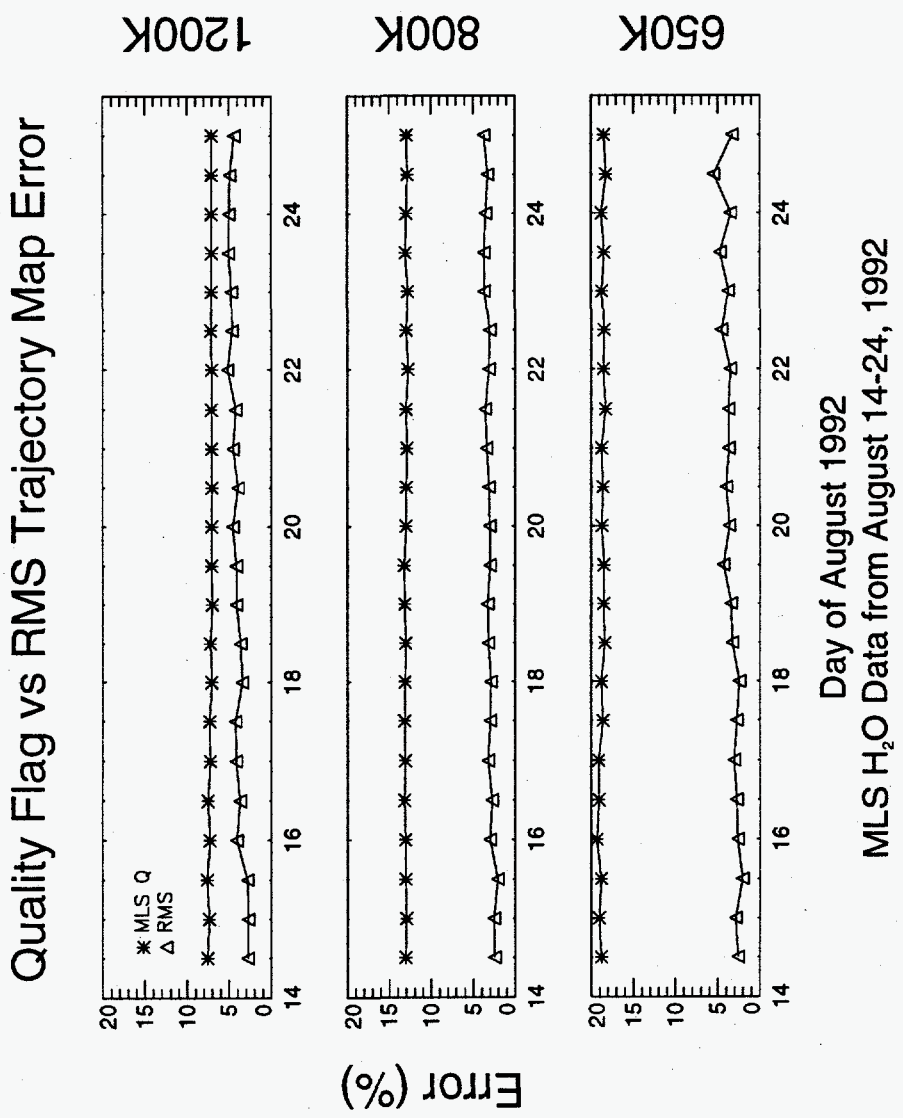

Figure 4.13 Precision of MLS Water Vapor Data

While the data set itself cannot provide a direct confirmation of the precision estimates derived from the trajectory technique, it is reassuring to note that the RMS errors are smaller than the quality flag parameters. This must certainly be the case if the RMS error has any value whatsoever, as the RMS error represents a lower bound on the error estimates while the quality flag represents an upper bound on the error. Future studies of instrument precision, particularly post-launch satellite instrument precision, should be enhanced with the use of the trajectory mapping technique.

4.3 Meteorological Field Evaluation

The trajectory mapping technique also provides a method by which meteorological wind fields can be evaluated. As with other applications of the technique, the methodology for evaluating meteorological wind field data is quite straightforward. Select a satellite data set for which a passive trace gas is consistently measured over an extended period of time. Using forward and backward trajectories, create a series of trajectory maps (in this case, every 12 hours) consisting of data measured within a specified time window (here, 1.5 days) of the synoptic map time. Examine successive neighborhoods of the oldest advected parcels (those initialized in the first 48 hours of the study period). Correlate the successive neighborhood averages with the original measurements and calculate the RMS error between the original measurements and the neighborhood averages.

In all cases, the correlations will decline and the RMS errors grow with time due to the inaccuracies of the technique (see Section 3.2). By examining the decay rates of advected data quality, the relative success of the three different wind fields at properly capturing dynamical events can be gauged. Figures 4.14–4.15 show the results of such a study performed using CLAES N_2O data (version 6) on the 800 K potential temperature surface (30 km) for the period September 1–15, 1992. This period was selected to include the known dynamical events which occur around September 5^{th} and 9^{th} [34]. The study employs the wind fields provided by NMC, UKMO, and GSFC's Data Assimilation Office. The results illuminate how well each of the meteorological fields capture the events.

Figure 4.14 shows the correlation coefficients for the three wind fields as calculated on each successive day of the study. All three cases are characterized by a fairly linear decline in correlation throughout the period. In general, the GSFC winds tend

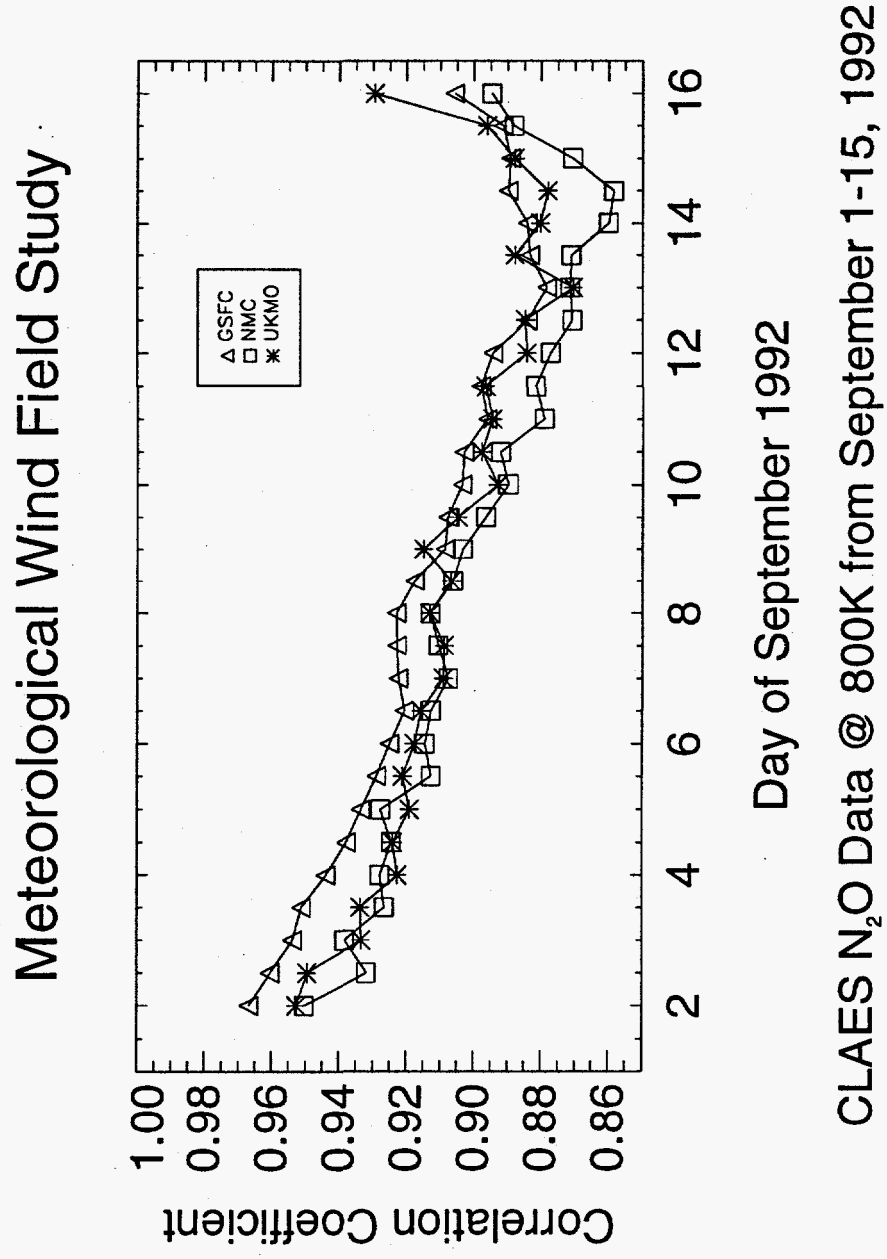

Figure 4.14 Meteorological Field Evaluation: Correlation Coefficients

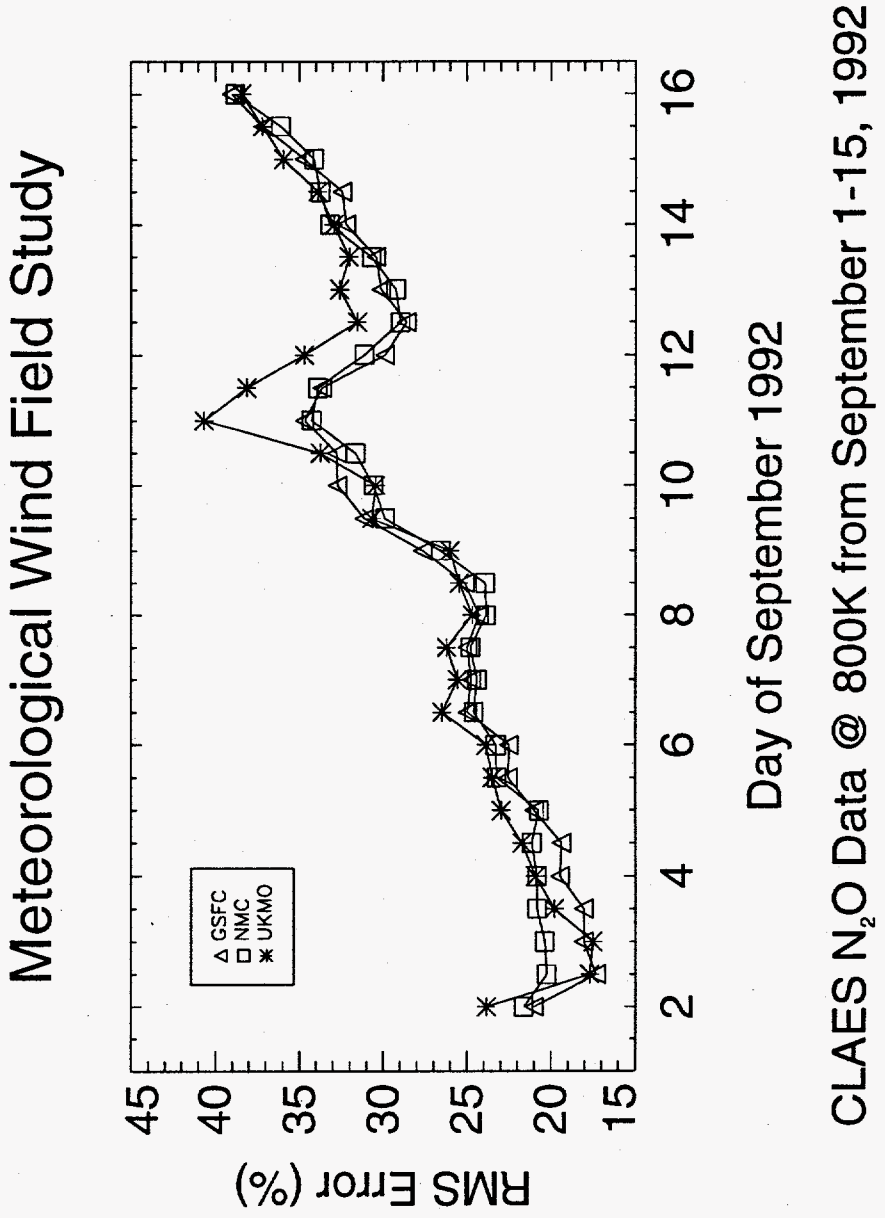

Figure 4.15 Meteorological Field Evaluation: RMS Errors

to result in slightly higher correlations than do NMC and UKMO winds throughout the period. These results, therefore, suggest that the higher temporal resolution of the GSFC fields may result in improvement of the trajectory calculations over the lower temporal resolution of the NMC and UKMO fields. Such a conclusion would agree with work published by *Waugh and Plumb* [56]. They examined the dependence of fine scale structure produced in contour advection studies upon the temporal and spatial resolution of the wind fields used to drive the material contours. After varying both quantities, they determined that the temporal resolution was far more important than the spatial resolution.

Figure 4.15 shows the growth of the RMS error as a function of time for each of the wind fields. While the RMS error is generally increasing throughout the period of study, the rate of its increase varies. In particular, after the occurrences of the wave breaking events on September 5^{th} and 9^{th}, the RMS errors show heightened jumps in value with subsequent recovery. In general, the UKMO errors tend to be higher than those for the NMC and GSFC runs. In particular, around the time of the second wave-breaking event, the UKMO RMS error jumps substantially more than that of either NMC or GSFC errors. Such a result is surprising given the fact that NMC and UKMO have the same temporal resolution, while UKMO has a better overall spatial resolution. However, the improvement in the spatial resolution of the UKMO data over NMC data is only longitudinal. Latitudinally, the NMC data set has better coverage. Perhaps, therefore, the lower resolution of the UKMO grid in the latitudinal direction hindered the UKMO's assessment of this mid-latitude event. Further tests, such as degrading the NMC meridional resolution to match that of UKMO, might help resolve this question.

Clearly, the trajectory mapping technique is an appropriate method by which to analyze and evaluate the quality of meteorological wind fields. In this Chapter, the trajectory mapping technique has also been applied to several other problems, including dynamical analysis and satellite data validation. In each case, the results of the trajectory mapping studies have been encouraging and indicate that trajectory mapping will be a useful technique for conducting a wide variety of studies in the future.

Chapter 5

Conclusions

This thesis has presented a new technique for producing synoptic maps from asynoptically gathered data. Known as trajectory mapping, this new technique combines observations made by satellite or in situ instruments with a simple 2-D model of atmospheric motions. The trajectory mapping technique has demonstrated strengths above and beyond those of several previously developed mapping techniques, including the Kalman filter, the Salby-Fourier technique, and constituent reconstruction.

In particular, trajectory mapping provides a simple, straightforward method by which trace gas data can be assimilated into synoptic maps. Unlike other techniques, which use mathematical fits to the data, trajectory mapping incorporates actual atmospheric behavior in its assimilation process. Trajectory maps can be produced both during data gathering periods and during periods of data are drop-out, so long as the wind and temperature fields (and heating rates for diabatic calculations) are available.

Estimates of the errors associated with the trajectory mapping technique have been evaluated and shown to be quite small for periods on the order of several days. Most sensitive are individual parcel trajectories, which can vary quite dramatically on short time scales (on the order of two or three days) depending on the wind fields employed. Diabatic effects seem to be characterized by time scales on the order of a week. Despite the individual trajectory differences, however, constituent distributions predicted from the advection of a large ensemble of measurements remain robust for much longer periods (on the order of weeks).

Knowledge of the limitations of the trajectory mapping technique (as indicated by the error analysis) aided the development of several procedures with a wide range of applications. Foremost among these applications is data validation. The technique has been successfully applied to studies of the accuracy (MLS vs HALOE—H_2O, MLS vs ER-2—O_3, MLS vs SBUV2—O_3) and the precision (MLS—H_2O) of satellite data sets. In addition, the technique also provides a method for evaluating meteorological wind fields.

The map products themselves have also proven useful in assessing and observing dynamical events, as in the cases of the wave-breaking events observed in the CLAES N_2O data from September 1992 and in the MLS H_2O data from February 1993. The technique appears to have a number of useful applications beyond the scope of the current thesis. Future work should include applications of the technique to chemical issues, such as a determination of the chemical partitioning and reaction rates for observed species. The technique should also provide the modeling community with a large number of useful products through which the models can be improved. Thus, trajectory mapping should become an important tool in determining the answers to some of the key questions about stratospheric behavior and, in particular, about the nature and scope of ozone depletion.

Bibliography

[1] D. G. Andrews, J. R. Holton, and C. B. Leovy. *Middle Atmosphere Dynamics.* Academic Press, San Diego, CA, 1987. p. 489.

[2] J. Austin and A. F. Tuck. The calculation of stratospheric air parcel trajectories using satellite data. *Q. J. R. Meteorol. Soc.*, 111:279–307, 1985.

[3] F. T. Barath et al. The Upper Atmosphere Research Satellite Microwave Limb Sounder Instrument. *J. Geophys. Res.*, 93(D6):10751–10762, 1993.

[4] G. Brasseur and S. Soloman. *Aeronomy of the Middle Atmosphere.* D. Reidel Publishing Company, Dordrecht, 1984.

[5] S. E. Cohn and D. F. Parrish. The behavior of forecast error covariances for a Kalman filter in two dimensions. *Monthly Weather Rev.*, 119(8):1757–1785, 1991.

[6] E. F. Danielsen. Trajectories: isobaric, isentropic and actual. *J. Meteor.*, 18:479–486, 1961.

[7] D. G. Dritschel. Contour surgery: A topological reconnection scheme for extended integrations using contour dynamics. *J. Comput. Phys.*, 77:240–266, 1988.

[8] L. S. Elson and L. Froidevaux. Use of fourier transforms for asynoptic mapping: Applications to the Upper Atmosphere Research Satellite Microwave Limb Sounder. *J. Geophys. Res.*, 98(D12):23039–23049, 1993.

[9] A. J. Fleig et al. Nimbus 7 Solar Backscatter Ultraviolet (SBUV) ozone products user's guide. Ref. Pub. 1234, NASA, 1990.

[10] J. F. Gleason, P. K. Bhartia, et al. Record low global ozone in 1992. *Science*, 260:523–526, 1993.

[11] W. L. Grose. Validation and intercomparison of constituent and temperature data measured from the UARS platform. *NASA report, in press*, 1994.

[12] K. V. Haggard, E. E. Remsberg, et al. Description of data on the Nimbus 7 LIMS map archival tape. Tech. Pap. 2553, NASA, 1986.

[13] D. L. Hartmann. The structure of the stratopshere in the Southern hemisphere during late winter 1973 as observed by satellite. *J. Atmos. Sci.*, 33:1141–1154, 1976.

[14] J. R. Herman, P. A. Newman, et al. The 1993 ozone hole using Meteor–3/TOMS data. *J. Geophys. Res.*, submitted, 1994.

[15] R. E. Kalman. A new approach to linear filtering and prediction problems. *Trans. ASME, Ser. D, J. Basic Eng.*, 82:35–45, 1960.

[16] R. E. Kalman and R. S. Bucy. New results in linear filtering and prediction theory. *Trans. ASME, Ser. D, J. Basic Eng.*, 83:95–108, 1961.

[17] K. F. Klenk, P. K. Bhartia, A. J. Fleig, and C. L. Mateer. Vertical ozone profile determination from Nimbus-7 SBUV measurements. In *Fifth Conference on Atmospheric Radiation*, Baltimore, MD, 1983.

[18] L. R. Lait. An alternative form for potential vorticity. *J. Atmos. Sci.*, 51(12):1754–1759, 1994.

[19] L. R. Lait et al. Reconstruction of O_3 and N_2O fields from the ER–2, DC–8, and balloon observations. *Geophys. Res. Lett.*, 17:521–524, 1990.

[20] L. R. Lait and J. L. Stanford. Applications of asynoptic space–time Fourier transform methods to scanning satellite measurements. *J. Atmos. Sci.*, 45(24):3784–3799, 1988.

[21] M. Loewenstein, J. R. Podolske, K. R. Chan, and S. E. Strahan. Nitrous oxide as a dynamical tracer in the 1987 Airborne Antarctic Ozone Experiment. *J. Geophys. Res.*, 94:11589–11598, 1989.

[22] M. Loewenstein, J. R. Podolske, K. R. Chan, and S. E. Strahan. N_2O as a dynamical tracer in the arctic vortex. *Geophys. Res. Lett.*, 17:477–480, 1990.

[23] G. L. Manney and R. W. Zurek. Interhemispheric comparison of the development of the stratospheric polar vortex during fall: a 3-dimensional perspective for 1991–1992. *Geophys. Res. Lett.*, 20:1275–1278, 1993.

[24] G. L. Manney, R. W. Zurek, et al. Stratospheric warmings during February and March 1993. *Geophys. Res. Lett.*, 21(9):813–816, 1994.

[25] M. E. McIntyre. Towards a Lagrangian-mean description of stratospheric circulations and chemical transports. *Philos. Trans. R. Soc. London, Ser. A*, 296:129–148, 1980.

[26] P. A. Newman, D. J. Lamich, et al. Meterological atlas of the Southern hemisphere lower stratosphere for August and September 1987. Tech. Mem. 4049, NASA, 1988.

[27] Project Office. *Airborne Arctic Stratospheric Expedition II.* NASA, Moffett Field, CA, 1991.

[28] Project Office. *Airborne Southern Hemisphere Ozone Experiment. Measurements for Assessing the Effects of Stratospheric Aircraft.* NASA, Moffett Field, CA, 1994.

[29] R. B. Pierce and T. D. A. Farlie. Chaotic advection in the stratosphere: implications for the dispersal of chemically perturbed air from the polar vortex. *J. Geophys. Res.*, 98(D10):18589–18595, 1993.

[30] R. B. Pierce, W. L. Grose, and J. M. Russell. Evolution of Southern hemisphere air masses observed by HALOE. *Geophys. Res. Lett.*, 21(3):213–216, 1994.

[31] R. A. Plumb, D. W. Waugh, et al. Intrusions into the lower stratospheric arctic vortex during the winter of 1991/92. *J. Geophys. Res.*, 99:1089–1106, 1994.

[32] M. H. Proffitt and R. J. McLaughlin. Fast-response dual-beam UV absorption ozone photometer suitable for use on stratospheric balloons. *Rev. Sci. Instrum.*, 54:1719–1728, 1983.

[33] W. J. Randel. The evolution of winds from geopotential height data in the stratosphere. *J. Atmos. Sci.*, 44:3097–3120, 1987.

[34] W. J. Randel, J. C. Gille, et al. Planetary wave mixing in the subtropical stratosphere observed in UARS constituent data. *Nature*, 365:533–535, 1993.

[35] C. A. Reber. The Upper Atmosphere Research Satellite (UARS). *Geophys. Res. Lett.*, 20(12):1215–1218, 1993.

[36] E. E. Remsberg, J. M. Russell, et al. Implications of the stratospheric water vapor distribution as determined from the Nimbus 7 LIMS Experiment. *J. Atmos. Sci.*, 41:2934–2945, 1984.

[37] A. E. Roche, J. B. Kumer, et al. The Cryogenic Limb Array Etalon Spectrometer (CLAES) on UARS: experiment description and performance. *J. Geophys. Res.*, 98(D6):10763–10775, 1993.

[38] C. D Rodgers. Retrieval of atmospheric temperature and composition from remote measurements of thermal radiation. *Rev. Geophys. Sp. Phys.*, 14:609–624, 1976.

[39] J. E. Rosenfield. A simple parameterization of ozone infrared absorption for atmospheric heating rate calculations. *J. Geophys. Res.*, 96:9065–9074, 1991.

[40] J. M. Russell et al. The Halogen Occultation Experiment. *J. Geophys. Res.*, 98(D6):10777–10797, 1993.

[41] M. L. Salby. Sampling theory for asynoptic satellite observations, part I: space–time spectra, resolution, and aliasing. *J. Atmos. Sci.*, 39:2577–2600, 1982.

[42] M. L. Salby. Sampling theory for asynoptic satellite observations, part II: fast Fourier synoptic mapping. *J. Atmos. Sci.*, 39:2601–2614, 1982.

[43] M. L. Salby et al. Global transport calculations with an equivalent barotropic system. *J. Atmos. Sci.*, 47:188–214, 1990.

[44] M. R. Schoeberl et al. Reconstruction of the constituent distributions and trends in the antarctic polar vortex from ER–2 flight observations. *J. Geophys. Res.*, 94:16815–16845, 1989.

[45] M. R. Schoeberl et al. MLS ClO observations and arctic polar vortex temperatures. *Geophys. Res. Lett.*, 20(24):2861–2864, 1993.

[46] M. R. Schoeberl and L. R. Lait. Conservative coordinate transformations for atmospheric measurements. In *Proceedings of the International School of Physics: the Use of EOS for Studies of Atmospheric Physics*, New York, 1992. Elsevier Science Publishing Company, Inc.

[47] M. R. Schoeberl and L. Sparling. Trajectory modeling. In G. Fiocco and G. Visconti, editors, *Proceedings of the International School of Physics: Diagnostic Tools in Atmospheric Physics*, New York, 1994. Elsevier Science Publishing Company, Inc.

[48] S. D. Schubert, R. B. Rood, and J. Pfaendtner. An assimilated dataset for Earth science applications. *Bull. Amer. Meteor. Soc.*, 74(12):2331–2342, 1993.

[49] L. Sparling, M. R. Schoeberl, et al. Trajectory modeling of emissions from lower stratospheric aircraft. *J. Geophys. Res.*, submitted, 1994.

[50] R. S. Stolarski, P. Bloomfield, R. D. McPeters, and J. R. Herman. Total ozone trends deduced from Nimbus 7 TOMS data. *Geophys. Res. Lett.*, 18(6):1015–1018, 1991.

[51] R. Swinbank and A. O'Neill. A stratosphere-troposphere data assimilation system. *Monthly Weather Rev.*, 122:686–702, 1994.

[52] F. W. Taylor. *Spectrometric Techniques*, volume 3, chapter Pressure Modulator Radiometry, pages 137–197. Academic Press, San Diego, CA, 1983.

[53] F. W. Taylor et al. Remote sensing of atmospheric structure and composition by pressure modulator radiometry from space: The ISAMS experiment on UARS. *J. Geophys. Res.*, 98(D6):10799–10814, 1993.

[54] A. F. Tuck, S. J. Hovde, et al. Intercomparison of HALOE and ER-2 aircraft H_2O and CH_4 observations collected during the second Airborne Arctic Stratospheric Experiment (AASE-II). *Geophys. Res. Lett.*, 20(12):1243–1246, 1993.

[55] J. W. Waters. Microwave limb-sounding of Earth's upper atmosphere. *Atmos. Res.*, 23:391–410, 1989.

[56] D. W. Waugh. Subtropical stratospheric mixing linked to disturbances on the polar vortex. *Nature*, 365:535–537, 1993.

[57] D. W. Waugh and R. A. Plumb. Contour advection with surgery: A technique for investigating fine scale structure in tracer transport. *J. Atmos. Sci.*, 51(4):530–540, 1994.

[58] D. W. Waugh, R. A. Plumb, et al. Transport of material out of the stratospheric arctic vortex by Rossby wave breaking. *J. Geophys. Res.*, 365:535–537, 1993.

Appendix A

UARS Instruments

Deployed September 14, 1991 from the Space Shuttle Discovery, the Upper Atmosphere Research Satellite (UARS) carries a variety of instruments designed to enhance our knowledge of the middle atmosphere. The instruments include solar monitors, atmospheric constituent sensors, and atmospheric Doppler wind measuring devices [35]. Table A.1 provides a listing of all the instruments aboard UARS. The data returned from the various instruments aboard UARS should further both our understanding of the mechanisms (both natural and man-made) which influence the stratosphere and the ways the stratosphere might affect climate and climate change [53].

UARS orbits the Earth about every 96 minutes in a plane inclined 57^0 to the Equator at an altitude of 585 km. Such an orbit restricts the limb scanning instruments on board to monitoring only from about 30^0 latitude in one hemisphere to about 80^0 latitude in the other. The orbit precesses at a rate of 5^0 per day, providing coverage of all local times in about 36 days. Ten times per year, the satellite performs a yaw maneuver, which rotates the platform 180^0 relative to its orbital velocity vector. This maneuver is required to maintain cold temperatures on the same side of the spacecraft at all times. For the limb-scanning instruments, the yaw maneuver changes the primary hemisphere of study. The launch window and yaw timing were prescribed to allow observation of the formation and break-up of the Southern hemisphere ozone hole during August/September and November respectively. For further information on the UARS platform, see *Reber* [35].

Of particular interest to the subject of this thesis are the atmospheric constituent sensors: HALOE, CLAES, MLS, and ISAMS. Each provides measurements of a set of atmospheric trace gasses in the stratosphere. Due to problems with the satellite's solar array, limited data were retrieved during June/early July 1992. Outside of this period, the satellite has performed admirably.

Acronym	Instrument	Task
SOLSTICE	Solar/Stellar Intercomparison Experiment	solar spectral measurements
SUSIM	Solar Ultraviolet Spectral Irradiance Monitor	"
ACRIM	Active Cavity Radiometer Irradiance Monitor	Total Solar Irradiance
PEM	Particle Environment Monitor	X-ray, particle, and magnetic field monitoring
CLAES	Cryogenic Limb Array Etalon Spectrometer	stratospheric IR constituent profiles
ISAMS	Improved Stratospheric and Mesospheric Sounder	upper stratospheric and mesospheric IR constituent profiles
MLS	Microwave Limb Sounder	stratospheric microwave constituent profiles
HALOE	Halogen Occultation Experiment	stratospheric IR constituent profiles
HRDI	High Resolution Doppler Imager	upper stratospheric mesospheric winds
WINDII	Wind Imaging Interferometer	mesospheric winds

Table A.1 UARS Instruments

A.1 HALOE

Unlike the other UARS instruments described here, the Halogen Occultation Experiment (HALOE) uses solar occultations to make constituent measurements twice per orbit: at sunrise and sunset. By tracking the sun during sunrise and sunset events, HALOE derives profiles for 8 constituents (O_3, HCl, HF, CH_4, H_2O, NO, NO_2, and aerosols), temperature, and pressure from as low as 15 to as high as 130 km (depending upon the constituent). The instrument makes measurements with a vertical resolution of better than 2 km, a horizontal field of view of 5 km (measured at the surface) perpendicular to the line-of-sight, and a limb path length of 300 km [40].

Since UARS completes approximately 15 orbits each day, HALOE returns 30 profiles daily: 15 at sunrise, 15 at sunset. This measurement strategy provides good longitudinal coverage on two latitude circles each day, one corresponding to the sunrise locations, the other corresponding to the sunsets. Latitude coverage various slowly over each UARS month. Due to HALOE's unusual sampling pattern, the launch of UARS was scheduled to optimize the number of HALOE observations of the extreme Southern hemisphere during times of noted ozone depletion.

To derive constituent profiles, HALOE examines absorption lines in the infrared part of the spectrum between 2.45 and 10.04 μm [40]. By measuring the absorption lines in the spectrum of a well known background source, the sun, HALOE measurements are self-calibrating and potentially highly accurate. Because of the temperature dependence of the absorption spectra of the species of interest at these wavelengths, a temperature profile is first derived using the absorption of CO_2 at 2.8 μm. The presence of aerosols from the eruption of Mt. Pinatubo has complicated this procedure, especially below 30 km. Below this altitude, National Meteorological Center (NMC) temperature data (see Appendix D.1 for more information) are reported [40].

A number of potential error sources can affect HALOE measurements. These errors include pointing errors, temperature profile uncertainties, contamination of targeted absorption lines by nearby lines of non-targeted species, instrument noise, and reference gas pressure uncertainties. In total, the HALOE team estimates an instrument precision of 3–8% of the measurement. Initial correlative studies with external data sets show agreement to within 10–15% for HALOE O_3 and H_2O measurements [40].

HALOE has operated nearly continuously since it was turned on about 4 weeks after launch. For further information, see *Russell et al.* [40].

A.2 CLAES

The Cryogenic Limb Array Etalon Spectrometer (CLAES) experiment makes measurements of a wide variety of stratospheric constituents. CLAES retrieves profiles of temperature, pressure, O_3, H_2O, CH_4, N_2O, NO, NO_2, N_2O_5, HNO_3, $ClONO_2$, HCl, CFC–11, CFC–12, and aerosols by examining their vibrational/rotational emission lines in the spectral bands between 3.5 and 13 μm [37].

The profiles are determined for altitudes between 10 and 60 km with a vertical resolution of 2.5 km (except for HCl, which, due to its weak signal is integrated over a greater vertical depth and, therefore, has a vertical resolution of 14 km). The field of view of the instrument extends 8.5 km in the horizontal direction perpendicular to the line-of-sight and covers the entire vertical range (between 10 and 60 km). The instrument, therefore, measures the whole profile, from top to bottom simultaneously [37].

During normal operation, retrievals are made through a mechanical cycling of a combination of etalons and filters. This procedure successively confines the measurements to specific wavelengths. Each 65 second cycle allows for the measurement of the entire suite of constituents. The large number of spectral bands at which the instrument makes measurements results in an overdetermination of the constituents which have emission lines in several of the bands. Determining a constituent mixing ratio from its primary spectral band allows for its later subtraction from spectral bands where it is a minor contributor. This technique allows a more accurate determination of the mixing ratios for constituents whose emission lines lie in regions of the spectra with several targeted contributors [37].

Reported mixing ratios are derived from 6 second integrations of detected infra-red emissions in each spectral band. Given the speed at which the spacecraft is traveling (covering about 8 km at the surface per second), the 6 second time integration results in a 48 km scale perpendicular to the line of sight for the measurement region. Successive measurements of individual species are linearly interpolated in time to the beginning/end of each 65 second cycle. CLAES reports, therefore, contain data for the entire suite of constituents at one point in space and time every 65 seconds [37].

Pressure and temperature profiles must be ascertained before constituent profiles can be derived. To determine pressures, CLAES examines the absorption of an O_3 line in the pressure broadened wings of a CO_2 line. Temperature is determined from CO_2 emissions in the 789–793 cm^{-1} band [37].

To minimize and stabilize signal contamination from instrument photon emissions, the optics are cryogenically cooled to 130 K. For calibration purposes, the instrument door, which holds a stable, blackbody source, is periodically closed, allowing the instrument to view a known spectrum. Spectral calibration is examined through periodic high resolution scanning of well known atmospheric features. The pointing accuracy of the instrument is checked by locating fixed stars [37].

CLAES successfully recorded data from just after launch through April 1993, at which time its cryogen supply expired. Expected profile accuracies range from 2.6–24% while precisions range from 1.6–7%. For further details and additional information, see *Roche et al.* [37].

A.3 MLS

The Microwave Limb Sounder (MLS) examines thermal microwave emissions to derive vertical profiles of ClO, O_3, and H_2O. Three microwave channels are employed to determine these profiles and the profiles of temperature and pressure: 63 GHz, 183 GHz, and 205 GHz. The 63 GHz channel permits the determination of the pressure profile from a molecular oxygen line. The 183 GHz channel provides water vapor and upper stratospheric ozone retrievals, while the 205 GHz channel allows measurement of lower stratospheric ozone and ClO. Extensive laboratory study of emission lines produced by these molecules from the Stark and Zeeman effects have determined their spectra with an accuracy of 1% at these wavelengths [55].

Because MLS is examining emission spectra, it is able to make measurements both day and night. Unlike retrievals from the other instruments, however, MLS retrievals are made at microwave frequencies. These frequencies are relatively insensitive to temperature. Knowledge of the exact temperature profile, therefore, is not required to derive the constituent profile. In addition, aerosols (such as those from Mt. Pinatubo which affected other UARS instruments more seriously) and ice clouds have minimal effect on the MLS measurements.

To return its constituent profiles, MLS scans in the vertical between 5 and 95 km in discrete steps with an integration time of 1.8 seconds at each vertical level.

Each measurement has a 3.5 km vertical resolution, is made through 300 km along the line-of-sight and is made over a horizontal distance of 12 km (as measured at the surface) perpendicular to the line-of-sight. ClO data are reported from 15–45 km, O_3 from 15–80 km, H_2O from 15–85 km (although water values below 46 mb (22 km) should be used with caution), and pressure and temperature from 30–60 km.

In flight calibration is periodically checked via a known internal source, and instrument noise levels are determined through the viewing of cold space.

MLS data are available from just after launch through the present. The 205 GHz channel, however, failed during April 1993. For more information on the MLS instrument, see *Barath et al.* [3] and *Waters* [55].

A.4 ISAMS

The Improved Stratospheric and Mesospheric Sounder (ISAMS) uses pressure modulator radiometry (PMR) [52] to make measurements of a number of gas constituents in the mesosphere and middle to upper stratosphere.

On board, eight cells contain the individual gasses to be measured by the PMR technique (CO_2, CO, CH_4, NO, N_2O, NO_2, and H_2O) in the infra-red wavelengths between 4.6 and 16.3 μm. In addition, wideband measurements are used to derive O_3, HNO_3, and N_2O_5 through the CO_2 channels, since these gasses are too reactive to be contained in their own gas cells. Finally, a window channel is available near 12.1 μm for detection of aerosols [53].

The instrument scans in the vertical from the tropopause to the mesopause once every 32 seconds in normal operating mode and has a vertical resolution of 2.4 km and a horizontal field of view of 16.6 km. Integrations are performed at each vertical level for 1.8 seconds resulting in a 12 km displacement (measured at the ground) of the satellite along its orbital track. Integration along the line of sight covers roughly 300 km [53]. Spectra from the Earth limb is routed through a chopper, which alternately passes cold space signal and Earth limb signal through the apparatus, thus providing calibration of each measurement against a background source.

ISAMS measures rotational/vibrational emission spectra from its target species both day and night. As with CLAES and HALOE, accurate temperature retrievals are necessary before constituent mixing ratios can be derived. To determine the temperature profiles between 40 and 80 km, ISAMS examines several peaks in the CO_2 emission spectrum.

Unlike the other instruments, ISAMS has the capability of looking out both sides of the UARS platform. ISAMS, therefore, has the potential to provide coverage at all latitudes between 80^0S and 80^0N every day. Normal operation entails that ISAMS instrument look out the dark side of the satellite. Sun-side viewing is initiated only to view latitudes obscured from dark side viewing.

The technique is susceptible to errors introduced by Doppler shifts of the targeted emission lines. Optics, mounts, and electronics aboard ISAMS are cooled to around 100 K to help reduce errors caused by instrument noise. Failure to accurately account for the Earth rotation, inaccurate reporting of the direction in which the instrument is viewing, and inaccurate estimates of the magnitude of winds along the line of sight can result in errors as high as 30% in N_2O. More typically, these errors are less than 10%.

ISAMS data retrieval did not begin in until three weeks after launch, to allow for satellite outgassing. Unfortunately, the instrument failed in July 1992, returning only 9 months of data. For further information on ISAMS, see *Taylor* [52] and *Taylor et al.* [53].

Appendix B

The SBUV2 Instrument

The Solar Backscatter Ultra-Violet Experiment 2 (SBUV2) was launched aboard the NOAA–11 satellite's afternoon platform in the fall of 1988. The satellite lies in a sun-synchronous, retrograde orbit circling the Earth 13 to 14 times daily. SBUV2 makes nadir measurements of total column ozone and ozone profiles in the ultra-violet region of the spectrum with a field of view 200 km^2.

In its primary retrieval mode, SBUV2 step scans 12 wavelength bands between 250 and 340 nm, performing 1 second integrations in each of the 12 targeted wavelength bands. Continuous scans are performed for solar spectral observation with 0.2 nm resolution between 160 and 400 nm. In these wavelength bands, absorption by ozone is dominant, with greater absorption at shorter wavelengths. Higher altitudes, therefore, are most responsible for absorption at these shorter wavelengths. Wavelengths shorter than 295 nm are completely absorbed by the ozone peak (lying between 20 and 25 km).

Total ozone measurements are determined from the ratio of measured backscattered Earth radiance to the measured incident solar irradiance. An optimal statistical technique is employed to derive the ozone profiles [38, 17]. The profiles are reported in both Umkehr layers (a set of standard levels down to 250 mb or 10 km) and on a set of 19 standard pressure levels. The vertical resolution of these profiles is limited to about 8 km between the 30 and 50 km levels. Below 30 km, the resolution is even coarser. Because the instrument is unable to see through clouds, a best guess must be used to fill in the column ozone below the cloud decks. In addition, data above 50 km is generally unreliable. For further information on SBUV2, see *Fleig et al.* [9].

Appendix C

Aircraft Data

The Airborne Southern hemisphere Ozone Experiment (ASHOE) consists of a series of flights of the ER–2 high altitude aircraft into and around the Southern polar vortex. The ASHOE flights take place during four periods from the late fall to mid-spring 1994 in the Southern hemisphere. The scheduling of the flights is designed to monitor the formation, evolution, and break-up of the polar vortex, and to observe the related chemical and dynamic processes. A second goal of the mission is to evaluate the impact on stratospheric chemistry of proposed high altitude transport fleet of aircraft. This goal will be attained through the simultaneously occurring Measurements for assessing the Effects of Stratospheric Aircraft (MAESA) experiments.

Most of the flights from this mission will originate from a base in Christchurch, New Zealand. From there, the ER–2 will sample air from both the polar vortex and mid-latitudes, depending upon the flight plan chosen and the meteorological conditions existing at the time of the flight.

The aircraft carries a suite of instruments to measure a variety of chemical constituents and meteorological variables in the lower stratosphere. (The plane generally flies in the lower stratosphere, between 15 and 22 km.) The instruments and measurements are listed in Table C.1. Measurements have been processed and averaged over 10 second intervals. With a cruising speed of roughly 200 m/sec, this averaging results in a horizontal resolution of about 2 km.

Three segments of the four planned for the mission had been completed at the time of this writing. The number of flights in each segment is highly variable due to the dependence of the aircraft on good weather conditions. Additionally, restrictions on the number of days each pilot can fly further limit the number of possible flights.

The first segment consisted of 12 flights from March 18 through April 15, 1994. This segment was designed to observe the formation of the primitive Southern polar vortex. The second segment consisted of 6 flights from May 23 through June 5, 1994. More information on the ASHOE/MAESA campaign can be found in the similarly entitled NASA publication [28].

Instrument	Measurements
High-Altitude OH Experiment (HO_x)	OH, HO_2
Multiple-Angle Aerosol spectrometer Probe (MASP)	aerosols
High-Sensitivity Fast-Response CO_2 Analyzer	CO_2
ER–2 Meteorological Measurement System (MMS)	p, T, u, v, w position, pitch, roll, heading yaw, angle of sideslip, airspeed aircraft velocity
Four-Channel Airborne Chromatograph Atmospheric Trace Species (ACATS IV)	CFC–11, CFC–113, MC, CT CFC–12, N_2O, HCFC–22, CH_4, CH_3Cl
Reactive Nitrogen	NO, NO_y
Microwave Temperature Profiler (MTP)	T (profiles)
Lyman α Hygrometer	H_2O
Airborne Tunable Laser Absorption Spectrometer (ATLAS)	N_2O, CH_4, CO
Composition and Photodissociative Flux Measurement (CPFM)	solar UV
Dual-Beam UV-Absorption Ozone Photometer	O_3
Ames Particle Sampler Impactor Experiment (APS)	soot, ice crystals, H_2SO_4, HNO_3
High Resolution Interferometer Sounder (HIS)	T (profiles)
Multiple Axis Resonance Fluorescence Chemical Conversion Detector for ClO and BrO	ClO, BrO
Aircraft Laser Infrared Absorption Spectrometer (ALIAS)	NO_2, HCl, CH_4, N_2O
Multi-Sample Aerosol Collection System (MACS)	aerosol

Table C.1 ER–2 Instruments

Another aircraft campaign which occurred during the UARS monitoring period was the Airborne Arctic Stratospheric Expedition II (AASE II). This series of 33 high-altitude aircraft flights took place between August 1991 and March 1992 and was designed to observe the Northern hemisphere winter vortex. A suite of instruments similar to that aboard the ER–2 for ASHOE measured a wide variety of trace gasses and meteorological variables in the lower stratosphere.

Flights for AASE II were based in Fairbanks, Alaska and Bangor, Maine. A DC–8 and an ER–2 aircraft made measurements both inside and outside the vortex. A typical flight plan consisted of a northbound flight from Bangor, Maine into the vortex on one potential temperature surface, a vertical dive inside the vortex, a southbound flight out of the vortex on a different potential temperature surface, and frequently, a second dive outside the vortex on the return flight. Generally, the flights occurred on potential temperature surfaces between 460 and 520 K (18–21 km). Further information on the AASE II campaign can be found in its associated NASA publication [27].

Appendix D

Meteorological Data

In order to run the trajectory model and produce trajectory maps, meteorological data sets of temperature and wind fields must be available. In the research presented in this thesis, three meteorological data sets have been employed: the National Meteorological Center (NMC) data, the United Kingdom Meteorological Office (UKMO) data, and Goddard Space Flight Center's Data Assimilation Office (GSFC) data. General information about each of these three data sets is given below.

D.1 NMC

Gridded data from the National Meteorological Center on wind and temperature fields are available on a set of 18 pressure levels between 1000 and 0.4 mb (surface to 55 km). Data are reported once per day (at 12:00Z) with grid spacing every 5^0 longitude by 2^0 latitude from pole to pole. While tropospheric data are the result of the optimal interpolation of radiosonde data and temperature profiles measured by the NOAA–10 satellite, stratospheric data are derived mainly from the TIROS Operational Vertical Sounder (TOVS) instrument aboard NOAA–10. Radiosonde data is included in stratospheric assimilation below 10 mb pressure surface (32 km) [26].

Balanced winds, temperatures, and potential vorticity are derived from the NMC data sets in the Goddard Laboratory for Atmospheres. The technique combines satellite data with an objective analysis and a general circulation model to produce the derived data sets [26].

D.2 UKMO

The United Kingdom Meteorological Office (UKMO) produces analyses of meteorological variables for the stratosphere and troposphere daily on a uniform grid with 42 vertical levels between the surface and 0.28 mb (57 km). The horizontal resolution of the analyses is 2.5^0 latitude by 3.75^0 longitude. To produce its analyses,

the UKMO uses an assimilation system which incorporates atmospheric data gathered from radiosondes (up to 50–10 mb or 21–32 km) and the TIROS-N series of NOAA polar orbiters (up to 1–0.4 mb or 48–55 km). Radiosonde and satellite data quality are assessed through comparison with model forecasts. Those data which substantially disagree from the forecasts are discarded unless they closely agree with other, nearby observations. After an initial model run, new data are added and the model output refined to better match observations. The UKMO analyses used in the studies presented in this thesis have been produced on 18 standard pressure levels in the stratosphere. For further information on the UKMO meteorological analyses, see *Swinbank and O'Neill* [51].

D.3 GSFC

The Goddard Laboratory for Atmosphere's Data Assimilation Office (GSFC) produces stratospheric and tropospheric analyses of meteorological and climatological variables. Using an optimal interpolation method, GSFC analyses combine observations gathered from satellite, surface, balloon, aircraft, and rocket measurements with a general circulation model. Solar irradiance, cloud cover, ice/snow extent, sea surface temperature, and topography are all taken into account in the calculations [48]. The resultant product is a dynamically consistent, gridded, analyzed set of meteorological variables. The stratospheric analyses are produced every 6 hours on a 4^0 latitude by 5^0 longitude grid at each of 18 presure levels ranging from 1000 to 0.4 mb (surface to 55 km).

Unlike other meteorological data sets, the Goddard assimilation product does not require an initialization scheme. Furthermore, imbalances created by new observations are damped through the time-differencing scheme employed [48]. More information can be found in *Schubert* [48].

Appendix E

Dynamical Diagnostic Variables

A number of useful diagnostic variables have been derived to assist in dynamical analysis. Particularly important in analyzing dynamical events and in assessing the quality of trajectory maps are the quantities of potential temperature and potential vorticity.

Potential temperature is defined to be the temperature a parcel of dry air would have if lowered/raised to a standard pressure surface p_o (typically chosen to be surface pressure of 1000 mb) from an initial temperature T and pressure p. The formal definition is given by

$$\theta = \mathrm{T}\left(\frac{\mathrm{p_0}}{\mathrm{p}}\right)^{\mathrm{R}/c_\mathrm{p}} \tag{E.1}$$

where R is the dry air gas constant (287 J/K/kg) and c_p is the specific heat of dry air at constant pressure (1004 J/K/kg).

Potential temperature acts as a vertical coordinate and is often used as a proxy variable for altitude. Because potential temperature acts as a quasi-conserved quantity, the motion of air parcels tends to be confined to isentropic surfaces for periods on the order of a week.

Due to its high correlation with trace gasses, potential vorticity (PV) can act as a proxy variable for constituent mixing ratios. PV is given by

$$\mathrm{PV} = (\zeta_\theta + f)\left(-g\frac{\delta\theta}{\delta \mathrm{p}}\right) \tag{E.2}$$

where g is the acceleration of Earth's gravity, θ is potential temperature, p is pressure, f is the Coriolis parameter given by

$$f = 2\Omega \sin\theta \tag{E.3}$$

(where Ω is the angular frequency of the Earth's rotation), and ζ_θ is the vertical component of relative vorticity as evaluated on a given potential temperature surface θ. ζ_θ is given by

$$\zeta_\theta = \frac{\delta v}{\delta x} - \frac{\delta u}{\delta y} \tag{E.4}$$

Here, v represents the North/South wind speed, and u represents the East/West wind speed.

Because it is highly dependent on latitude, PV often acts as a proxy variable for latitude. PV, however, also depends substantially on altitude. In fact, the function for PV increases exponentially with altitude. This increase is mainly due to the pressure derivative term in the definition of PV. To remove this effect and, thus, to better compare dynamical structures on different potential temperature surfaces, a modified form of potential vorticity has been created.

A form of modified potential vorticity (MPV) was suggested by *Lait* [18]. To remove the altitude dependence inherent in Ertel's definition, MPV rescales PV so that

$$\mathrm{MPV} = \mathrm{PV}\left(\frac{\theta}{\theta_0}\right)^{-9/2} \tag{E.5}$$

For this thesis, θ_0 has been defined to be 490 K. MPV thereby shows substantially smaller vertical gradients than does the more familiar Ertel definition of PV.